A PROPER TIME DEPENDENT MEASUREMENT OF ΔM_D USING JET CHARGE AND SOFT LEPTON FLAVOR TAGGING

Owen R. Long

A DISSERTATION

in

PHYSICS AND ASTRONOMY

Presented to the Graduate Faculty of the University of Pennsylvania in Partial Fulfillment of the Requirements for the Degree of Doctor of Philosophy

1998

Supervisor of Dissertation

Graduate Group Chairman

DEDICATION

This thesis is dedicated to my family and

to the memory of my friend and colleague George Michail.

ACKNOWLEDGMENTS

I would like to thank my advisor Nigel Lockyer for his guidance and support. His enthusiasm for physics is an inspiration. I'm also very grateful to Joseph Kroll for his guidance during my stay at Fermilab.

I'm deeply appreciative of the support given by Marjorie Shapiro, Manfred Paulini, and Marc Peters. It was a pleasure working with all of you.

Many thanks to Fumihiko Ukegawa for always answering my naive physics questions and being a great office mate.

I'm very grateful to Steve Hahn and the rest of the Drug Sniffing Dogs for their camaraderie and providing countless hours of fun. Thanks to Mike and Merry Starr for letting us invade your house every week. Long live DSD!

Finally, I would like to thank Brendan, Mark, Wasiq, Farrukh, Rick, and Maria for their generous friendship. If I forgot anyone, I'm sure I will remember later and feel bad about it.

ABSTRACT

A PROPER TIME DEPENDENT MEASUREMENT OF ΔM_D USING JET CHARGE AND SOFT LEPTON FLAVOR TAGGING

Owen R. Long

Nigel Lockyer

This thesis presents a proper time dependent measurement of the B_d^0 mixing frequency Δm_d using jet charge and soft lepton flavor tagging in $p - \bar{p}$ collisions at $\sqrt{s} = 1.8$ TeV. The measurement uses the inclusive e and μ trigger data of the CDF detector from an integrated luminosity of 91 pb^{-1}. The proper time at decay is measured from a partial reconstruction of the B associated with the trigger lepton. The measurement of Δm_d yields

$$\Delta m_d = 0.50 \pm 0.05 \pm 0.05 \ \hbar \ \mathrm{ps}^{-1}$$

where the first error is statistical and the second systematic. The flavor tagging methods used give a measured effective efficiency ϵD^2 of

- Jet Charge: $\epsilon D^2 = (0.78 \pm 0.12 \pm 0.09)$ %
- Soft Lepton: $\epsilon D^2 = (1.07 \pm 0.09 \pm 0.10)$ %

where the first error is statistical and the second systematic.

Contents

0.1 Introduction 1

1 Theoretical Background **13**

1.1 B Physics and the CKM Matrix 13

1.2 The Unitarity Triangle 14

1.3 CP Violation 15

1.4 The Phase of ξ 20

1.5 The Sides of the Unitarity Triangle 22

1.6 Mixing, Δm_d, and $|V_{td}|$ 23

2 The CDF Detector **27**

2.1 Tracking 30

2.1.1 CDF Coordinates and Track Helix Parameters 30

2.1.2 The Silicon Vertex Detector (SVX) 31

2.1.3 The Central Tracking Chamber (CTC) 36

2.2 The Central Electromagnetic Calorimeter (CEM) 43

2.3 The Central Fast Tracker (CFT) 45

2.4 The Central Muon Detectors 46

2.5 Triggers 47

2.5.1 The Inclusive Electron Trigger 48

2.5.2 The Inclusive Muon Trigger 49

3 The Data Samples **50**

3.1 Offline Lepton Selection Criteria 53

3.1.1 The Inclusive Electron Trigger 54

3.1.2 The Inclusive Muon Trigger 55

3.2 Monte Carlo Samples 55

3.3 Secondary Vertex Finding 57

3.3.1 The Primary Vertex Location 57

3.3.2 Track-Based Jets 58

3.3.3 The Secondary Vertexing Algorithm 59

3.4 Fake Trigger Electrons 67

3.5 Conversion Electron Removal 69

3.6 Fake Trigger Muons 73

3.7 Ratio of $b\bar{b}$ to $c\bar{c}$ Events 76

4 Reconstruction of the Proper Time t **82**

4.1 Resolution on Transverse Decay Length L_{xy} 83

4.2 Estimating $P_t(B)$ 84

5 Flavor Tagging **92**

5.1 Introduction 92

5.1.1 The Flavor Tag Dilution 93

5.1.2 The Raw Dilution 95

6 Jet Charge Flavor Tagging **97**

6.1 $b\bar{b}$ Production Topologies 98

6.2 Jet Selection and Classification 102

6.2.1 Double Secondary Vertex Tagged Events 102

6.2.2 Single Secondary Vertex Tagged Events 102

6.3 Jet Charge Distributions and Dilutions 103

7 Soft Lepton Flavor Tagging **109**

8 Determination of Δm_d and the Dilution Normalization N_D **113**

8.1 The Probability Density 114

8.2 Convolution of ct Resolution With the Probability Density 118

8.3 Fit Parameters 120

8.4 Fit Range in ct 123

8.5 Results of Fit for Δm_d 124

8.6 Systematic Errors 127

8.7 Check of the Fit Using a Fast Monte Carlo 138

8.8 Flavor Tag ϵD^2 Values 140

9 Conclusion **142**

A Glossary of Symbols and Acronyms **144**

B Fake Muon Estimate From Flavor Tag Dilution **148**

Bibliography **150**

List of Tables

1.1 The amplitude of the CP asymmetry for different B hadrons (B_d^0 and B_s^0) and decay modes ($b \to c$ and $b \to u$). 21

1.2 Various parameters involved in calculating $|V_{td}|$ from Δm_d. 24

2.1 Geometry and strip multiplicity of the SVX silicon wafers. The pitch is the spacing between microstrips. 34

2.2 Some features of the CTC. 39

3.1 Track quality criteria for track clustering. The CTC exit radius is the radial position at which the track crosses the plane that defines the edge of the CTC in z. 59

3.2 Average separation from e in dE/dx for particles with the trigger electron momentum spectrum. 67

3.3 Tight and loose cuts used in conversion finding. 70

3.4 Results of the P_t(rel) and m(cl) fits for the $b\bar{b}$ to $c\bar{c}$ ratio in the electron trigger data for the jet charge single vertex, jet charge double vertex, and soft lepton flavor tag events. 77

3.5 Results of the P_t(rel) and m(cl) fits for the $b\bar{b}$ to $c\bar{c}$ ratio in the muon trigger data for the jet charge single vertex, jet charge double vertex, and soft lepton flavor tag events. 78

3.6 Nominal values for the $b\bar{b}$ to $c\bar{c}$ ratio in the jet charge single vertex, jet charge double vertex, and soft lepton flavor tagged data for the electron and muon triggers. 78

6.1 Jet charge flavor tag $\sum \epsilon D(raw)^2$ where the sum is in bins of $|Q_{jet}|$. . 104

7.1 Soft lepton flavor tag $\sum_i \epsilon_i D^2_{raw}$ where the sum is in bins of soft lepton P_t(rel). 111

8.1 Parameters of the fit and their sources. 122

8.2 Results of the fits for Δm_d and N_D for the electron trigger data. The first errors are statistical and the second systematic. The systematic errors were evaluated for the jet charge and soft lepton flavor tags separately and are summarized in Tables 8.8 and 8.6. The systematic errors for the combined fit were calculated from the tables mentioned above, taking into account the correlated and uncorrelated variations. 130

8.3 Results of the fits for Δm_d and N_D for the muon trigger data. The first errors are statistical and the second systematic. The systematic errors were evaluated for the jet charge and soft lepton flavor tags separately and are summarized in Tables 8.9 and 8.7. The systematic errors for the combined fit were calculated from the tables mentioned above, taking into account the correlated and uncorrelated variations. 131

8.4 Correlation coefficients for the free parameters Δm_d and N_D in the fit. 132

8.5 Result of the e and μ trigger, jet charge and soft lepton combined fit. The first errors are statistical and the second systematic. The systematic errors were calculated from Tables 8.6, 8.7, 8.8, and 8.9 taking into account the correlated and uncorrelated variations. . . . 133

8.6 Systematic errors for the fit for Δm_d and the N_D factors for the soft lepton tagged e trigger data. 134

8.7 Systematic errors for the fit for Δm_d and the N_D factors for the soft lepton tagged μ trigger data. 135

8.8 Systematic errors for the fit for Δm_d and the N_D factors for the jet charge tagged e trigger data. 136

8.9 Systematic errors for the fit for Δm_d and the N_D factors for the jet charge tagged μ trigger data. 137

8.10 Values for N_D factors, where Δm_d has been fixed to the world average: 0.47 $\hbar$ ps^{-1}. The first error is statistical, the second systematic. . . . 140

8.11 Vales for ϵD^2, corrected with the N_D factors in Table 8.10. The first error is statistical, the second systematic. 141

B.1 Uncorrected average raw dilution for three flavor taggers in the electron and muon data. 149

B.2 Average raw dilution for three flavor taggers in the electron and muon data corrected for wrong sign sequential decay trigger leptons and the $b\bar{b}$ to $c\bar{c}$ ratio. 150

List of Figures

0.1 A triangle in the complex plane formed from the unitarity constraint on the first and third columns of V_{CKM}. 11

0.2 Box Feynman diagrams responsible for B_d^0 mixing. 12

1.1 A unitarity triangle in the complex plane formed from the 1st and 3rd columns of the CKM matrix. The sides have been renormalized by dividing by $V_{cd}V_{cb}^* = A\lambda^3$. 16

1.2 Box diagrams responsible for B^0 mixing. The amplitude of the diagram is proportional to $(V_{tb}V_{td}^*)^2$. 26

2.1 An isometric view of the CDF detector. 28

2.2 A 1/4 slice of the CDF detector. The image should be reflected to the right and below. The beam-beam interaction point is in the lower right of the figure. 29

2.3 A helix in the transverse plane with the impact parameter D_0 and initial phi ϕ_0 labeled. The radius of the helix is $1/2C$, where C is the curvature. 32

2.4 A generic silicon detector. The bias voltage V^+ applied to the n^+ side depletes the n^+ volume of free electrons and creates an electric field. A charged particle passing through the detector leaves a trail of electron/hole pairs, where the holes are collected at the p^+ strips. . . 33

2.5 A SVX event display. 35

2.6 A SVX event display. 36

2.7 The wire positions for an axial superlayer cell of the CTC. 38

2.8 CTC aluminum endplate showing the cell slots. 41

2.9 A CTC event display. 42

2.10 An illustration of an electromagnetic shower. 43

2.11 A central electromagnetic calorimeter (CEM) wedge. 45

3.1 The ordering hierarchy for tracks to be considered in vertexing. Tracks with high $|D_0/\sigma_{D_0}|$ and P_t and a large number of good SVX hits are favored and considered first. Tracks in the same class are sorted by the Secondary Sorting variable. 62

3.2 An illustration of the definition of the transverse decay length L_{xy}. Note that although only the secondary vertex tracks are shown, the tracking jet defines the jet axis. The jet axis may include tracks in addition to the secondary vertex tracks. The pointing error of the jet axis to the primary vertex has been exaggerated for clarity. 64

3.3 Reconstructed transverse decay length L_{xy} distributions for the electron (left) and muon (right) trigger data, $b\bar{b}$ Monte Carlo, and $c\bar{c}$ Monte Carlo. 66

3.4 Results of the dE/dx fits for the e, π, K, and p fractions in the $L_{xy} < 0$ and $L_{xy} > 0$ events. The p curve was not plotted because the fits gave no statistically significant p fraction. The errors are statistical only. . 68

3.5 The conversion partner dE/dx spectra for loose (top) and tight (bottom) criteria. 71

3.6 L_{xy} distributions for the single-track trigger sample, μ trigger data, and μ trigger $b\bar{b}$ Monte Carlo. All distributions are normalized to unit area. 75

3.7 The trigger lepton $P_t(rel)$ (thick vector) is defined as the component of the trigger lepton momentum transverse to the jet that it's associated with. The jet axis (dotted line) is calculated without including the trigger lepton. 79

3.8 Results of the P_t(rel) fits for the $b\bar{b}$ to $c\bar{c}$ ratio. The points with error bars are the data. The solid curve is the result of the fit, which is the sum of the $b\bar{b}$ component (dashed curve) and the $c\bar{c}$ component (dotted curve). 80

3.9 Results of the m(cl) fits for the $b\bar{b}$ to $c\bar{c}$ ratio. The points with error bars are the data. The solid curve is the result of the fit, which is the sum of the $b\bar{b}$ component (dashed curve) and the $c\bar{c}$ component (dotted curve). 81

4.1 The distributions of difference between the reconstructed (L_{xy}(meas)) and true (L_{xy}(true)) transverse decay length as predicted by the Monte Carlo. The three Gaussians and two exponentials used to parameterize the distributions are shown. 87

4.2 Examples of K-factor distributions from the e trigger Monte Carlo. Direct refers to direct semileptonic decay ($b \to l\nu$). Sequential refers to sequential semileptonic decay ($b \to c \to l\nu$). 88

4.3 Reconstructed ct for the soft lepton tagged data (solid) and a combination of $b\bar{b}$ and $c\bar{c}$ Monte Carlo (dashed). The ratio of $b\bar{b}$ to $c\bar{c}$ Monte Carlo is from Table 3.6. The solid and dashed distributions are both normalized to unit area. 89

4.4 Reconstructed ct for the jet charge single vertex data (solid) and a combination of $b\bar{b}$ and $c\bar{c}$ Monte Carlo (dashed). The ratio of $b\bar{b}$ to $c\bar{c}$ Monte Carlo is from Table 3.6. The solid and dashed distributions are both normalized to unit area. 90

4.5 Reconstructed ct for the jet charge double vertex data (solid) and a combination of $b\bar{b}$ and $c\bar{c}$ Monte Carlo (dashed). The ratio of $b\bar{b}$ to $c\bar{c}$ Monte Carlo is from Table 3.6. The solid and dashed distributions are both normalized to unit area. 91

6.1 The π^- produced in b quark fragmentation, where a $\bar{B}_d^0$ is formed, is correlated in charge with the original b quark flavor. 99

6.2 Representative Feynman diagrams for the three main $b\bar{b}$ production mechanisms. Note that not all possible diagrams are shown. 101

6.3 Jet charge and $D(raw)$ vs $|Q_{jet}|$ distributions for single and double vertex tagged events in the e trigger data. 105

6.4 Jet charge and $D(raw)$ vs $|Q_{jet}|$ distributions for single and double vertex tagged events in the μ trigger data. 106

6.5 The raw dilution $D(raw)$, flavor tag efficiency ϵ, and $\epsilon D(raw)^2$ in bins of $|Q_{jet}|$ for single and double vertex e trigger events. 107

6.6 The raw dilution $D(raw)$, flavor tag efficiency ϵ, and $\epsilon D(raw)^2$ in bins of $|Q_{jet}|$ for single and double vertex μ trigger events. 108

7.1 The soft lepton raw dilution as a function of the soft lepton P_t(rel). The data are divided into the 5 soft lepton types for the e and μ triggers. The negative P_t(rel) point is for events where the soft lepton is isolated and does not have a P_t(rel) measurement. The solid curve is used in the event-by-event dilution prediction. The dashed curves are used in the evaluation of the systematic error on the dilution parameterization. 112

8.1 The ct distributions for the single track trigger sample, μ trigger data, and μ trigger $b\bar{b}$ Monte Carlo. All distributions are normalized to unit area. 117

8.2 A generic K-factor distribution. 119

8.3 Determination of effective $c\bar{c}$ lifetime from the e and μ trigger $c\bar{c}$ Monte Carlo. 121

8.4 The raw same sign fraction as a function of the reconstructed proper time for the jet charge and soft lepton tagged e and μ trigger data. . 125

8.5 The raw same sign fraction as a function of the reconstructed proper time for the combined jet charge and soft lepton tagged e and μ trigger data. The curve is a representation of the fit result. 126

8.6 Several fast Monte Carlo experiments simulating the soft lepton tagged e trigger data. 139

0.1 Introduction

In the Standard Model [1], which describes the physics of elementary particles, there are three generations of leptons and quarks. The left-handed leptons and quarks form the $SU(2)$ weak isospin doublets illustrated below

$$\begin{pmatrix} \nu_e \\ e^- \end{pmatrix}_L \quad \begin{pmatrix} \nu_\mu \\ \mu^- \end{pmatrix}_L \quad \begin{pmatrix} \nu_\tau \\ \tau^- \end{pmatrix}_L$$

$$\begin{pmatrix} u \\ d' \end{pmatrix}_L \quad \begin{pmatrix} c \\ s' \end{pmatrix}_L \quad \begin{pmatrix} t \\ b' \end{pmatrix}_L$$

The doublet for each lepton generation contains a massless neutrino, denoted ν_i, and a lepton with a negative unit of charge. Each quark doublet consists of an up-type quark with charge $2/3$ and a down-type quark with charge $-1/3$. The generations form a mass hierarchy where each new generation is more massive. That is,

$$m_e \ll m_\mu \ll m_\tau$$

and

$$m_u \text{ and } m_d \quad \ll \quad m_c \text{ and } m_s \quad \ll \quad m_t \text{ and } m_b.$$

The down-type quark mass eigenstates (d, s, b) are connected to the weak eigenstates (d', s', b') via the Cabibbo-Kobayashi-Maskawa (CKM) quark mixing ma-

trix [2][3] shown below

$$\begin{pmatrix} d' \\ s' \\ b' \end{pmatrix} = \begin{pmatrix} V_{\rm ud} & V_{\rm us} & V_{\rm ub} \\ V_{\rm cd} & V_{\rm cs} & V_{\rm cb} \\ V_{\rm td} & V_{\rm ts} & V_{\rm tb} \end{pmatrix} \begin{pmatrix} d \\ s \\ b \end{pmatrix} = V_{CKM} \begin{pmatrix} d \\ s \\ b \end{pmatrix} \tag{0.1}$$

where the elements of V_{CKM} may be complex. The analogous mixing matrix for the leptons is the unit matrix due to the fact that the neutrinos are massless [1]. The absence of tree-level flavor-changing neutral currents requires V_{CKM} to be unitary [4]. The elements of V_{CKM} are fundamental parameters of the Standard Model and must be measured experimentally. One way to look for physics beyond the Standard Model is to explicitly test the unitarity of V_{CKM} through experimental measurements.

The unitarity constraint on V_{CKM} that is currently of most interest comes from the first and third columns, namely

$$V_{ud}V_{ub}^* + V_{cd}V_{cb}^* + V_{td}V_{tb}^* = 0 \tag{0.2}$$

$$V_{ub}^* + V_{cd}V_{cb}^* + V_{td} \approx 0 \tag{0.3}$$

where we have used the fact that $|V_{ud}|$ and $|V_{tb}|$ are known to be very close to one. The equation above can be visualized as a triangle in the complex plane, shown in Figure 0.1. The standard phase convention for V_{CKM} has been used [5] in which both V_{cd} and V_{cb} are essentially real numbers. The magnitudes of V_{cd} and V_{cb} have

[1] Recent experimental results [6] and the solar neutrino deficit [7] suggest that neutrinos may have a small mass, indicating a non-trivial lepton mixing matrix.

been fairly accurately measured already. The magnitude of V_{cd} comes from charm production measurements in deep inelastic neutrino scattering combined with the measured semileptonic branching fractions of charm quark mesons. The magnitude of V_{cb} comes from the measured semileptonic branching fractions and the lifetime of bottom quark mesons. This leaves the length of two sides and the three angles (α, β, and γ) to be measured. The magnitude of V_{ub} is known to be very small ($\approx 3\times10^{-3}$) and is measured from the branching fractions of B meson decays involving a $b \to u$ transition, which are quite rare. As will be discussed below, $|V_{td}|$ can be determined through the frequency of $B_d^0 - \bar{B}_d^0$ oscillations. The angles α, β, and γ can be determined through studying classes of B meson decay rates that violate the combined operation of charge conjugation C, which changes particle to antiparticle, and parity P, which inverts spatial directions.

Neutral B mesons display an interesting property known as mixing, where the B meson oscillates between the particle and antiparticle state before decaying. A B meson consists of quark-antiquark pair, bound together by the strong force, where either the quark or the antiquark is a b quark. By convention, the anti-B meson ($\bar{B}$) contains a b quark ($b\bar{q}$) and the B meson contains an anti-b quark ($\bar{b}q$). For a neutral B meson, the b quark combines with either a $\bar{d}$ or a $\bar{s}$ antiquark. The B_d^0 transition from the particle to antiparticle state, and vice versa, occurs through the second order weak transition depicted by the box Feynman diagrams shown in

Figure 0.2. The diagrams involve the exchange of virtual t quarks and $W^{\pm}$ bosons. Similar diagrams with either u or c quarks in place of the t quarks are also possible but their contributions are negligible compared to the t quark loop contribution, due to the extremely heavy mass of the t quark (≈ 170 GeV/c^2). The frequency of the oscillation is the small difference in mass between the weak eigenstates of the B_d^0 [2] and is related to the V_{CKM} elements by

$$\Delta m_d \propto |V_{td}V_{tb}|^2. \tag{0.4}$$

Since $|V_{tb}| \approx 1$ a measurement of Δm_d enables the calculation of $|V_{td}|$.

This thesis is a measurement of Δm_d using data from the Collider Detector at Fermilab (CDF). The CDF experiment resides in the Tevatron which collides protons (p) and antiprotons ($\bar{p}$) at a center of mass energy of $\sqrt{s} = 1.8$ TeV. In the $p\bar{p}$ collisions, $b\bar{b}$ quark pairs are produced. The first experimental observations of B^0 mixing came from experiments at e^+e^- colliders running on the $\Upsilon(4S)$ resonance [8][9][10]. These were later confirmed by experiments at e^+e^- colliders running on the Z^0 resonance [11][12][13][14]. The $b\bar{b}$ production cross sections on the $\Upsilon(4S)$ and Z^0 are ≈ 1 nb [15] and ≈ 7 nb [5] respectively. The $b\bar{b}$ cross section in $p\bar{p}$ collisions at a center of mass energy of $\sqrt{s} = 1.8$ TeV is ≈ 40 μb [16], which is 4 orders of magnitude larger. However, the $b\bar{b}$ cross section is around 0.1 % of the total inelastic cross section for $p\bar{p}$ collisions [17], which makes identifying $b\bar{b}$ production events experimentally

[2] See Chapter 1 for a detailed discussion of B^0 mixing and CP violation in the B^0 system.

challenging.

Leptons are often produced in the decay of B mesons either directly through semileptonic decay ($b \to c\ l\ \nu$) or indirectly through sequential decays ($b \to c \to s\ l\ \nu$). They can also be produced through B meson decays to charmonium states such as $B_d^0 \to J/\psi K_s^0$ where $J/\psi \to l^+l^-$. It is straightforward for high energy experiments to identify events containing high momentum ($P > 3$ GeV/c) electrons and muons thus creating data sets enriched with events from $b\bar{b}$ production. The relatively long lifetime of the B meson (1.5 ps) and the Lorentz boost from the initial momentum of the b quark cause the B hadrons to often travel several millimeters before decaying. Experiments with detectors that very accurately measure charged particle trajectories near the $p\bar{p}$ collision enable the reconstruction of the location of the B decay point or "vertex". Requiring evidence of at least one decay vertex separated from the $p\bar{p}$ interaction point further enriches the data in events from $b\bar{b}$ production.

This analysis uses a high statistics sample of data containing at least one high momentum lepton (either e or μ) that is associated with a decay vertex separated from the $p\bar{p}$ interaction point. The lepton and decay vertex requirements purify the sample significantly: over 90 % of the events are from $b\bar{b}$ production. The lepton also serves the essential purpose of determining whether the B meson [3] was in the particle or antiparticle state at the time of decay. The charge of a lepton from a semileptonic

[3]Not all of the B hadrons are B mesons. The b quark forms a baryon (bqq' or $\bar{b}\bar{q}\bar{q}'$) about 10 % of the time.

B decay shares the same sign as the charge of the b quark that produced it, thus l^+ (l^-) events indicate a B ($\bar{B}$) meson at the time of decay. The fraction of events in the sample where the lepton is from semileptonic B decay is about 80 %.

In order to determine if the B meson that produced the high momentum lepton decayed in "mixed" state ($B^0(t=0) \to \bar{B}^0 \to l^- \ X$ or $\bar{B}^0(t=0) \to B^0 \to l^+ \ X$), knowledge of the initial particle/antiparticle nature of the B meson is required. This is known as "tagging" the "flavor" of the B meson at the time of production. To do this, we use the other B meson in the event, taking advantage of the fact that the b quarks are produced in $b\bar{b}$ pairs. We use two flavor tagging methods: soft lepton and jet charge.

If two leptons are present in the event, the required high momentum lepton and a second (perhaps lower momentum) lepton, the charge of the second lepton provides the flavor tag. This assumes that the second lepton comes from the semileptonic decay of the "other" B meson and that it did not decay in a mixed state. This is correct a good fraction of the time. The efficiency of this method is rather low (≈ 5 %) due to the lepton identification efficiencies, the semileptonic branching fraction ($Br(B \to l \ X) \approx 10$ % for both e and μ), and the fact that the other B is in the acceptance of the detector only ≈ 40 % of the time.

The jet charge flavor tag uses a momentum-weighted charge average of particles

in a b quark jet [4], from the production and subsequent decay of the B hadron, to infer the charge of the b quark. The relation between the sign of the jet charge (Q_{jet}) and the b quark charge is the same as that for semileptonic B decay. That is, a positive jet charge indicates a $\bar{b}$ quark. A negative jet charge indicates a b quark. Since the jet charge is applied to the other b jet, not the one that produced the trigger lepton, the signature for a mixed event is when the jet charge and the charge of the high momentum lepton have the same sign. If two jets in the event, the high momentum lepton jet and another, contain a decay vertex separated from the $p\bar{p}$ interaction point, the second jet with a decay vertex is used for the calculation of the jet charge. This greatly enhances the effectiveness of the jet charge because the decay vertex unambiguously identifies the jet as coming from the other b quark in the event.

The jet charge flavor tagging method was developed by experiments at e^+e^- colliders running on the Z^0 resonance [18][19][20][21][22]. The method is very efficient and has produced some of the most accurate measurements of Δm_d to date. This analysis is the first application of jet charge flavor tagging in data from hadron collisions.

The B^0 mixing frequency Δm_d can be determined in either a time integrated or time dependent way, where by time we mean the proper time of the B meson at decay. A time integrated measurement simply counts the number of mixed and unmixed events. The frequency Δm_d is inferred from the fraction of events that mixed

[4] A **jet** is a collimated group of particles produced by the hadronization and decay of a quark or by a gluon.

and the B meson lifetime. A time dependent measurement explicitly measures the time dependence of the mixing probability, which is given by the equations below

$$P_m(t) = , \; e^{-\Gamma t} \frac{1}{2} \left(1 - \cos(\Delta m \; t)\right) \tag{0.5}$$

$$P_u(t) = , \; e^{-\Gamma t} \frac{1}{2} \left(1 + \cos(\Delta m \; t)\right). \tag{0.6}$$

where $P_m(t)$ ($P_u(t)$) is the probability that the B^0 decayed in a mixed (unmixed) state at the proper time t. There are several advantages in doing a time dependent measurement of Δm_d instead of a time integrated measurement.

First, a time dependent measurement is the only way to distinguish between B_d^0 and B_s^0 mixing. The frequency of B_s^0 mixing is larger than the B_d^0 frequency by a factor of $|V_{ts}|^2/|V_{td}|^2$, which is of order 20. One of the original goals of this analysis was to measure or set a lower limit on Δm_s. However, recent results have shown that Δm_s is indeed very large [23] making a competitive limit on Δm_s from the method used in this analysis infeasible.

Second, a time dependent measurement allows one to calibrate the flavor tagging methods while simultaneously determining Δm_d. For a time integrated measurement, the average probability that the flavor tag is correct (P_{tag}) must be known in advance. In a time dependent measurement, the amplitude of the mixed fraction as a function of the proper time at decay determines P_{tag}, while the frequency determines Δm_d.

Flavor tagging has another interesting application, which is the measurement of CP violation in B meson decays. As in a Δm_d measurement, a CP asymmetry

measurement requires knowledge of the initial flavor of the B meson. For example, to study the asymmetry between the decay rates for $B_d^0 \to J/\psi K_s^0$ and $\bar{B}_d^0 \to J/\psi K_s^0$, one needs to know if the B meson that decayed to $J/\psi K_s^0$ was initially a B_d^0 or a $\bar{B}_d^0$. The measured CP asymmetry is given by

$$A_{CP}(\text{meas}) = \frac{N - \bar{N}}{N + \bar{N}} \tag{0.7}$$

where N ($\bar{N}$) is the observed number of $J/\psi K_s^0$ decays from B mesons whose initial flavor was tagged as B_d^0 ($\bar{B}_d^0$). The true asymmetry is related to the measured asymmetry through the relation

$$A_{CP}(\text{true}) = \frac{1}{D} \cdot A_{CP}(\text{meas}) \tag{0.8}$$

where D is the dilution of the flavor tagging method and is defined by

$$D = 2 \cdot P_{tag} - 1. \tag{0.9}$$

Like a time integrated mixing measurement, the quantity of interest ($A_{CP}(\text{true})$) can not be extracted from the measured quantity without knowing P_{tag} (or equivalently D) for the flavor tagging methods used. The measurement of CP asymmetries, such as the one described above, is the primary focus of several experimental efforts including the construction of three dedicated B physics experiments and two asymmetric e^+e^- colliders [24][25][26].

There have already been several measurements of Δm_d [23], most of which come from the experiments at Large Electron-Positron (LEP) collider at CERN. While

this analysis gives a determination of Δm_d that is competitive with most individual measurements, it will not have a large impact on the world average. However, the techniques developed in this analysis, in particular the flavor taggers, will play a crucial role in the future study of B mesons at CDF. The CDF collaboration has ambitious physics objectives [27] for the next colliding beam run which include:

- The observation of CP violation in the decay $B_d^0 \to J/\psi K_s^0$, which will give a measurement of $\sin(2\beta)$ to better than ± 0.13.
- The observation of CP violation in the decay $B_d^0 \to \pi^+\pi^-$, which will give a measurement of $\sin(2\alpha)$ to better than ± 0.14.
- Measuring or setting a stronger limit on Δm_s.

Jet charge and soft lepton flavor tagging are essential for achieving all three of these goals.

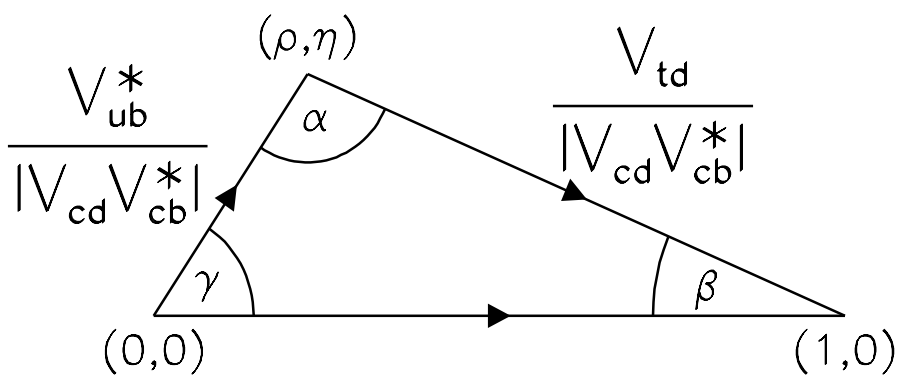

Figure 0.1: A triangle in the complex plane formed from the unitarity constraint on the first and third columns of V_{CKM}.

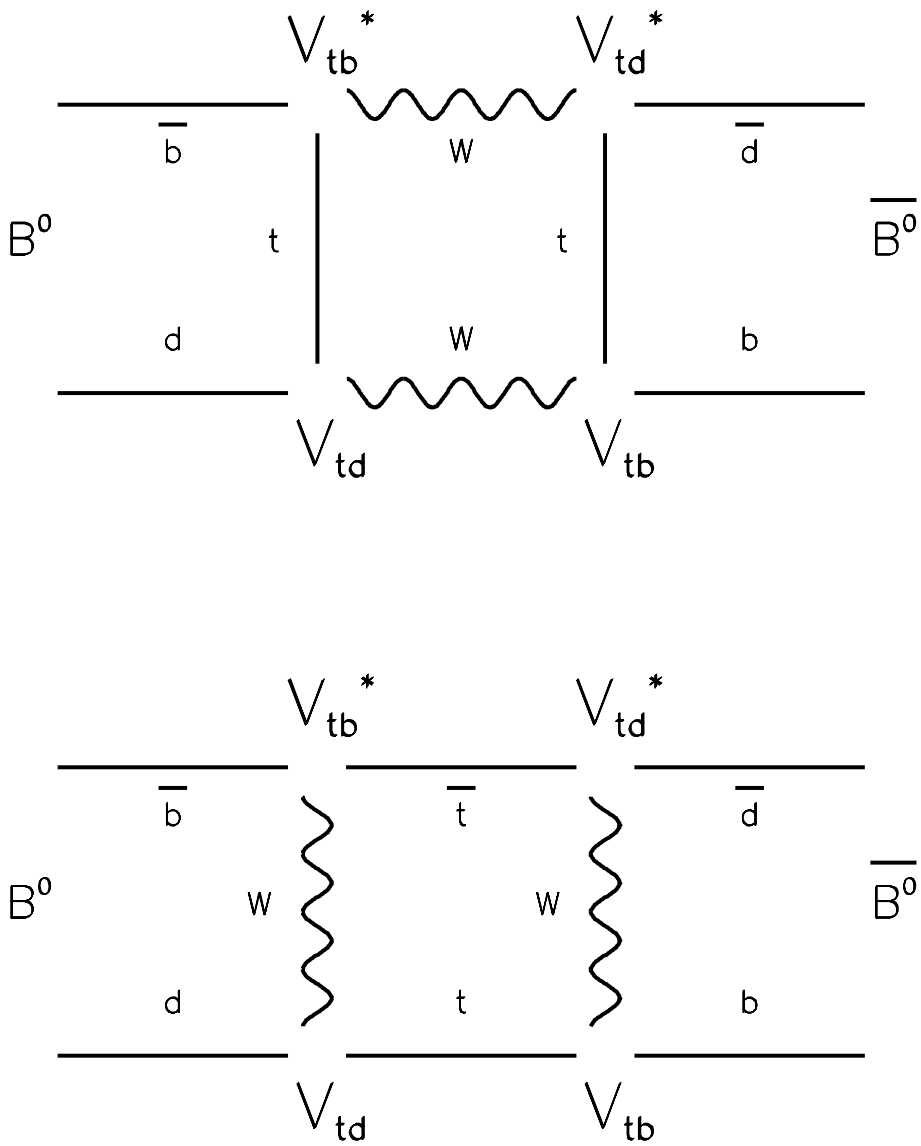

Figure 0.2: Box Feynman diagrams responsible for B_d^0 mixing.

Chapter 1

Theoretical Background

1.1 B Physics and the CKM Matrix

In the Standard Model quarks and leptons are coupled to the W-boson field via the charged current J^{μ}_{cc}. The Lagrangian for charged current processes is given by

$$L_{cc} = -\frac{g}{\sqrt{2}} \left(J^{\mu}_{cc} \; W^{+}_{\mu} + J^{\mu\,\dagger}_{cc} \; W^{-}_{\mu} \right) \tag{1.1}$$

where

$$J^{\mu}_{cc} = \sum_{k} \; \bar{\nu}_k \; \gamma^{\mu} \; \frac{1}{2} \left(1 - \gamma^5 \right) e_k + \sum_{i,j} \; \bar{u}_i \; \gamma^{\mu} \; \frac{1}{2} \left(1 - \gamma^5 \right) V_{ij} \; d_j \tag{1.2}$$

and the sums (i, j, k) are over the 3 generations [29]. The 3×3 unitary matrix V is the so called CKM matrix [3] which describes the coupling of the charge 2/3 quarks with the charge $-1/3$ quarks.

$$V = \begin{pmatrix} V_{\mathrm{ud}} & V_{\mathrm{us}} & V_{\mathrm{ub}} \\ V_{\mathrm{cd}} & V_{\mathrm{cs}} & V_{\mathrm{cb}} \\ V_{\mathrm{td}} & V_{\mathrm{ts}} & V_{\mathrm{tb}} \end{pmatrix} \tag{1.3}$$

The CKM matrix elements are fundamental parameters of the Standard Model and must be measured.

For example, the semileptonic decay amplitude for $\bar{B}^0 \to D^+ l^- \bar{\nu}$ is given by [30]

$$M\left(\bar{B}^0 \to D^+ l^- \bar{\nu}\right) = -i\,\frac{G_F}{\sqrt{2}}\,V_{cb}\,L^\mu\,H_\mu \tag{1.4}$$

where we have ignored the q^2 dependence of the W propagator because of the relatively small momentum transfer involved in B decays ($q^2 \ll M_W^2$). The leptonic current in terms of Dirac spinors is [30]

$$L^\mu = \bar{u}_l\,\gamma^\mu\left(1-\gamma^5\right)v_\nu. \tag{1.5}$$

The hadronic current is given by

$$H_\mu = \langle \bar{D}\,|\,\bar{c}\,\gamma_\mu\,(1-\gamma_5)\,b\,|\,\bar{B}^0\rangle. \tag{1.6}$$

The hadronic current cannot be calculated perturbatively and is typically written in terms of q^2 dependent form factors.

1.2 The Unitarity Triangle

A 3×3 unitary matrix with complex elements can be written in terms of four independent real parameters, where one of these parameters is a phase factor. Wolfenstein [32] has written the CKM matrix in a form, given below, which was inspired by the 2

generation matrix introduced by Cabibbo [2] which rotates the d and s quarks.

$$V = \begin{pmatrix} 1-\lambda^2/2 & \lambda & A\lambda^3(\rho - i\eta) \\ -\lambda & 1-\lambda^2/2 & A\lambda^2 \\ A\lambda^3(1-\rho-i\eta) & -A\lambda^2 & 1 \end{pmatrix} \tag{1.7}$$

The parameter λ is the sin of the Cabibbo angle θ_C ($\sin\theta_C \approx 0.22$).

The first and third columns of the CKM matrix give the following unitarity constraint:

$$V_{ud}V_{ub}^* + V_{cd}V_{cb}^* + V_{td}V_{tb}^* = 0 \tag{1.8}$$

$$A\lambda^3(\rho + i\eta) - A\lambda^3 + A\lambda^3(1-\rho-i\eta) + 0\ (\lambda^4) = 0 \tag{1.9}$$

This can be visualized as a triangle in the complex plane, shown in Figure 1.1. Measuring the sides and angles of the unitarity triangle is the primary goal of the next generation of B physics experiments. If an inconsistency is found, that is if the triangle isn't "closed", it would be a sign of physics beyond the three generation Standard Model.

1.3 CP Violation

An interesting consequence of the irreducible phase in the CKM matrix is CP violation in some B decays. By CP violation it is meant that the combined application of charge conjugation C (particle to anti-particle) and parity P ($\vec{x}$ to $-\vec{x}$) to some B

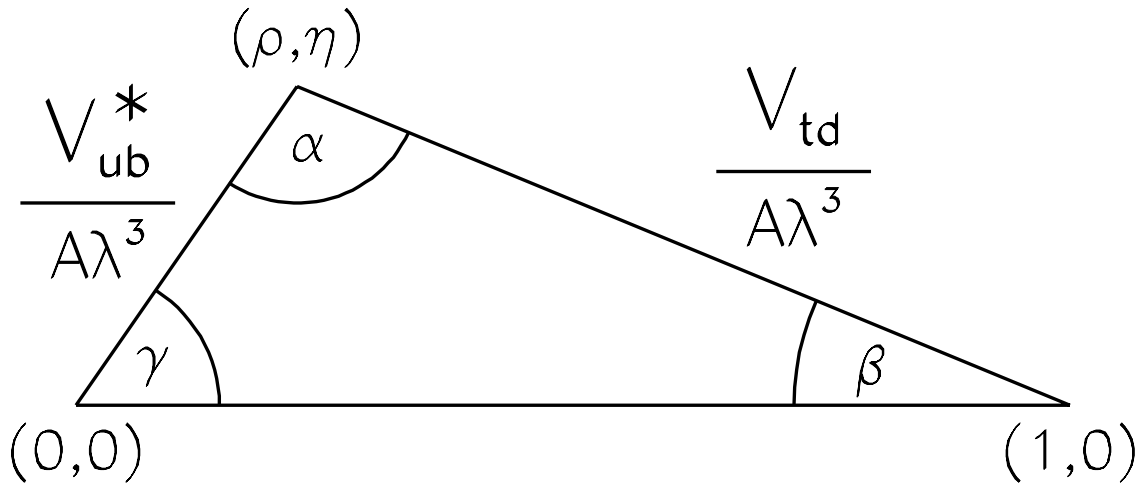

Figure 1.1: A unitarity triangle in the complex plane formed from the 1st and 3rd columns of the CKM matrix. The sides have been renormalized by dividing by $V_{cd}V_{cb}^{*} = A\lambda^3$.

decays yields different rates, or

$$, \ (B \to f) \neq , \ (CP\ B \to CP\ f) = , \ \left(\bar{B} \to \bar{f}\right). \tag{1.10}$$

As will be shown below, this is a consequence of the interference of amplitudes with different phases that give the same final state.

The following discussion uses the now standard notation that can be found in Reference [33]. For neutral B mesons, the states of definite flavor (B^0 and $\bar{B^0}$) are not eigenstates of the weak interaction. The weak Hamiltonian in the $|B^0\rangle$, $|\bar{B}^0\rangle$ basis can be written as

$$H = M - \frac{i}{2} \ , \tag{1.11}$$

where the 2×2 mass and decay matrices (M and ,) are Hermitian. More explicitly,

the Hamiltonian equation is given by

$$H \begin{pmatrix} B^0 \\ \bar{B}^0 \end{pmatrix} = \begin{pmatrix} M - \frac{i}{2}\,, & M_{12} - \frac{i}{2}\,,_{12} \\ M_{12}^* - \frac{i}{2}\,,^*_{12} & M - \frac{i}{2}\,, \end{pmatrix} \begin{pmatrix} B^0 \\ \bar{B}^0 \end{pmatrix} \tag{1.12}$$

where the Hermiticity of M and $,$ has been imposed. CPT invariance gives $H_{11} = H_{22}$.

Diagonalization of the Hamiltonian yields the eigenstates

$$|B_L\rangle = p\,|B^0\rangle + q\,|\bar{B}^0\rangle \tag{1.13}$$

$$|B_H\rangle = p\,|B^0\rangle - q\,|\bar{B}^0\rangle. \tag{1.14}$$

where

$$p = N\,\left(M_{12} - \frac{i}{2}\,,_{12}\right), \quad q = N\,\sqrt{\left(M_{12} - \frac{i}{2}\,,_{12}\right)\left(M_{12}^* - \frac{i}{2}\,,^*_{12}\right)} \tag{1.15}$$

and N is a normalization factor. The eigenvalues are

$$\mu_H = M - \frac{i}{2}\,, + Q \tag{1.16}$$

$$\mu_L = M - \frac{i}{2}\,, - Q \tag{1.17}$$

where

$$Q = \sqrt{\left(M_{12} - \frac{i}{2}\,,_{12}\right)\left(M_{12}^* - \frac{i}{2}\,,^*_{12}\right)} \tag{1.18}$$

$$Q = \frac{1}{2}\,\left(\Delta m - \frac{i}{2}\,\Delta,\right). \tag{1.19}$$

The quantities Δm and $\Delta,$ are the difference in mass and width between the states $|B_L\rangle$ and $|B_H\rangle$. For the B_d^0 system, $M_{12} \gg ,_{12}$ [31] so from now on the approximation

, $_{12} \approx 0$ and $\Delta,\ \approx 0$ will be used. Note that this may not be appropriate for the B_s^0 system where Δ, /, may be as large as 30 % [35].

The time dependence of an eigenstate of the Hamiltonian is proportional to $e^{-i\mu_j t}$. Using this and equations 1.13 and 1.14, initially pure $|B^0\rangle$ and $|\bar{B}^0\rangle$ states can be constructed:

$$|B^0(t)\rangle = g_+(t)\ |B^0\rangle + g_-(t)\ \frac{q}{p}\ |\bar{B}^0\rangle \tag{1.20}$$

$$|\bar{B}^0(t)\rangle = g_-(t)\ \frac{p}{q}\ |B^0\rangle + g_+(t)\ |\bar{B}^0\rangle \tag{1.21}$$

where

$$g_+(t) = e^{-iMt}\ e^{-\frac{1}{2}\Gamma t}\ \cos\left(\frac{\Delta m}{2}t\right) \tag{1.22}$$

$$g_-(t) = e^{-iMt}\ e^{-\frac{1}{2}\Gamma t}\ i\ \sin\left(\frac{\Delta m}{2}t\right) \tag{1.23}$$

Note that for $t > 0$ there is a finite probability that a $|B^0\rangle$ can be observed as a $|\bar{B}^0\rangle$ and vice versa. This is the phenomenon known as "B^0 mixing", which will be discussed in detail later.

Consider a final state f and it's CP conjugate $\bar{f}$ where f and $\bar{f}$ are accessible by $|B^0\rangle$ and $|\bar{B}^0\rangle$ respectively. The time dependent widths are given by

$$, (B^0(t) \to f) = |\langle f|B^0(t)\rangle|^2 \tag{1.24}$$

$$, (\bar{B}^0(t) \to \bar{f}) = |\langle \bar{f}|\bar{B}^0(t)\rangle|^2 \tag{1.25}$$

$$, (B^0(t) \to f) = |\langle f|B^0\rangle|^2\ e^{-\Gamma t}\ \left\{\cos^2\left(\frac{\Delta m}{2}t\right) + |\xi|^2\ \sin^2\left(\frac{\Delta m}{2}t\right) - \mathrm{Im}(\xi)\ \sin(\Delta m t)\right\}$$

$$, (\bar{B}^0(t) \to \bar{f}) = |\langle \bar{f}|\bar{B}^0\rangle|^2\ e^{-\Gamma t}\ \left\{\cos^2\left(\frac{\Delta m}{2}t\right) + |\bar{\xi}|^2\ \sin^2\left(\frac{\Delta m}{2}t\right) - \mathrm{Im}(\bar{\xi})\ \sin(\Delta m t)\right\}$$

where

$$\xi = \frac{q}{p}\,\frac{\langle f|\bar{B}^0\rangle}{\langle f|B^0\rangle}\ , \qquad \bar{\xi} = \frac{p}{q}\,\frac{\langle \bar{f}|B^0\rangle}{\langle \bar{f}|\bar{B}^0\rangle}. \tag{1.26}$$

Note that if , $_{12} \approx 0$, as is being assumed, q/p is a pure phase, since $q/p \approx \sqrt{M_{12}^*/M_{12}}$.

Now consider the special case where f is a CP eigenstate with only one weak amplitude contributing. In this case

$$CP\ |f\rangle = +|\bar{f}\rangle\ , \quad CP\ |\bar{f}\rangle = -|f\rangle \tag{1.27}$$

and thus

$$|\langle f|B^0\rangle| = |\langle \bar{f}|\bar{B}^0\rangle|\ , \quad |\langle f|\bar{B}^0\rangle| = |\langle \bar{f}|B^0\rangle|. \tag{1.28}$$

This means ξ is a pure phase, giving the simplified formulas

$$, (B^0(t) \to f) \;=\; |\langle f|B^0\rangle|^2\ e^{-\Gamma t}\ \{1 - \mathrm{Im}(\xi)\ \sin(\Delta m t)\} \tag{1.29}$$

$$, (\bar{B}^0(t) \to \bar{f}) \;=\; |\langle \bar{f}|\bar{B}^0\rangle|^2\ e^{-\Gamma t}\ \{1 + \mathrm{Im}(\xi)\ \sin(\Delta m t)\} \tag{1.30}$$

where the condition $\mathrm{Im}(\xi) = -\mathrm{Im}(\bar{\xi})$ has been used.

Equations 1.29 and 1.30 can be used to calculate the time dependent CP asymmetry $A(t)$ defined below.

$$A(t) = \frac{, (B^0(t) \to f) - , (\bar{B}^0(t) \to \bar{f})}{, (B^0(t) \to f) + , (\bar{B}^0(t) \to \bar{f})} \tag{1.31}$$

$$A(t) = -\ \mathrm{Im}(\xi)\ \sin(\Delta m t) \tag{1.32}$$

1.4 The Phase of ξ

As Equation 1.32 shows, CP is not violated if ξ is a real number. There are two sources for the phase of ξ:

- A phase difference in the decay amplitude for $|B^0\rangle$ and $|\bar{B}^0\rangle$.
- B_d^0 mixing.

Figure 1.2 shows the two box diagrams responsible for B^0 mixing. The vertices are labeled with the appropriate CKM matrix elements. Recall that

$$\frac{q}{p} \approx \sqrt{\frac{M_{12}^*}{M_{12}}} \tag{1.33}$$

The amplitude of the box diagrams shown in Figure 1.2 is proportional to M_{12} and is given by [34]

$$M_{12} \propto (V_{tb}V_{td}^*)^2 \tag{1.34}$$

so when considering a B_d^0 decay mode

$$\frac{q}{p} \approx \frac{V_{tb}^* V_{td}}{V_{tb}V_{td}^*} = \frac{V_{td}^*}{V_{td}} \equiv e^{i2\beta} \tag{1.35}$$

where the assumption $V_{tb} = 1$, as in the Wolfenstein parameterization, has been used. The phase of V_{td} is defined to be the angle β which is illustrated in the unitarity triangle shown in Figure 1.1. This shows that B_d^0 mixing connects the phase of V_{td} to the CP asymmetry $A(t)$. It is interesting to note that for B_s^0 mixing, V_{td} is replaced

with V_{ts} in the above expressions. This means that B_s^0 mixing does not by itself lead to CP violation since V_{ts} is real [1].

Now, we consider the possible phase difference in the decay amplitude. A b quark can decay either to a c quark or a u quark. Therefore the decay amplitude will be proportional to either V_{cb} or V_{ub} or

$$\frac{\langle f|\bar{B}^0\rangle}{\langle f|B^0\rangle} = \begin{cases} V_{cb}/V_{cb}^* = 1, & b \to c \\ V_{ub}/V_{ub}^* \equiv e^{i2\gamma}, & b \to u \end{cases} \tag{1.36}$$

The phase of V_{ub} is the angle γ of the unitarity triangle shown in Figure 1.1.

Table 1.1 summarizes the CP asymmetry amplitude for different combinations of B^0 hadrons (B_d^0 and B_s^0) and decay modes ($b \to c$ and $b \to u$). It has been shown that CP asymmetry measurements measure the phase of V_{td} and V_{ub} and thus the angles in the unitarity triangle.

	B_d^0	B_s^0
$b \to c$	$-\sin(2\beta)$	0
$b \to u$	$-\sin(2\gamma + 2\beta) = \sin(2\alpha)$	$-\sin(2\gamma)$

Table 1.1: The amplitude of the CP asymmetry for different B hadrons (B_d^0 and B_s^0) and decay modes ($b \to c$ and $b \to u$).

[1] Actually, this statement is true only to order λ^3. In the standard parameterization of the CKM matrix [5], the element V_{ts} has a small imaginary component. Keeping terms of order λ^4, gives [35] $V_{ts} = -A\lambda^2 + \frac{1}{2}A(1-2\rho)\lambda^4 - i\eta A\lambda^4$.

1.5 The Sides of the Unitarity Triangle

To rigorously test the CKM matrix, both the angles and the sides of the unitarity triangle must be measured. CP asymmetry measurements are sensitive to the angles of the unitarity triangle. The measurement of the sides is discussed in this section.

The base of the triangle in Figure 1.1 is equal to $|V_{cd}V_{cb}^*|$. In the Wolfenstein parameterization,

$$|V_{cd}V_{cb}^*| = A\lambda^3. \tag{1.37}$$

The Cabibbo angle λ (or $|V_{cd}|$) is quite well known so the task is to measure the parameter A or $|V_{cb}|/\lambda^2$. $|V_{cd}|$ is deduced from single charm production in deep inelastic neutrino - nucleon scattering and from the semileptonic branching fractions of charmed mesons [35].

Next, consider the left hand side of the triangle in Figure 1.1, which is $|V_{ub}|/A\lambda^3$. $|V_{ub}|$ can be measured from the branching fractions of decays involving a $b \to u$ transition [36].

Lastly, we have the right hand side of the triangle, which is $|V_{td}|/A\lambda^3$. $|V_{td}|$ can be measured by measuring the B_d^0 mixing frequency Δm_d. This thesis is such a measurement. In the next section we will discuss in detail how $|V_{td}|$ is extracted from Δm_d.

1.6 Mixing, Δm_d, and $|V_{td}|$

This thesis is a measurement of Δm_d. In this section B^0 mixing, Δm_d, and the relation between Δm_d and $|V_{td}|$ are discussed.

Neutral B mesons can oscillate between their particle and anti particle state via the box diagrams shown in Figure 1.2. The time dependent probability that a B^0 decays in same or opposite particle/antiparticle state is given by

$$P_m(t) = |\langle B^0|\bar{B}^0(t)\rangle|^2 = |\langle \bar{B}^0|B^0(t)\rangle|^2 \tag{1.38}$$

$$P_u(t) = |\langle B^0|B^0(t)\rangle|^2 = |\langle \bar{B}^0|\bar{B}^0(t)\rangle|^2 \tag{1.39}$$

where P_m (P_u) is the "mixed"("unmixed") probability. The term "mixed" means the B^0 has decayed in the opposite particle/antiparticle state from $t = 0$. Using Equations 1.20, 1.21, 1.22, and 1.23

$$P_m(t) = \ , \ e^{-\Gamma t}\ \frac{1}{2}\ (1 - \cos(\Delta m\ t)) \tag{1.40}$$

$$P_u(t) = \ , \ e^{-\Gamma t}\ \frac{1}{2}\ (1 + \cos(\Delta m\ t))\,. \tag{1.41}$$

It is clear from Equations 1.40 and 1.41 what is meant by mixing. The frequency of the oscillation is given by Δm, which was introduced in Equation 1.19.

The box diagram calculation for Δm yields [34]

$$\Delta m_q = \frac{G_F^2\ m_W^2}{6\pi^2}\ \eta_B\ f_B^2\ B_B\ m_B\ S(\bar{m}_t/m_W)\ |V_{tq}V_{tb}^*|^2. \tag{1.42}$$

where [37] [38]

$$S(\bar{m}_t/m_W) = 0.784\ (\bar{m}_t/m_W)^{2\times 0.76} \tag{1.43}$$

Table 1.2 gives the parameters in Equation 1.42 and their current values. Solving

Symbol	Parameter	Value	Reference
G_F	Fermi constant	1.17×10^{-5} GeV^2	Ref [5]
m_W	W boson mass	80.22 ± 0.26 GeV/c^2	Ref [5]
η_B	QCD correction factor	0.55 ± 0.01	Ref [39]
$f_B B_B^{1/2}$	"Bag factor" & decay constant	200 ± 40 MeV	Ref [40]
m_B	B_d mass	5.28 GeV	Ref [5]
$S(\bar{m}_t/m_W)$	Inami-Lim function	2.46	Ref [37] [38]
$\bar{m}_t$	Running Top quark mass	167 ± 6 GeV/c^2	Ref [41]
Δm_d	B_d Mixing parameter	$0.474 \pm 0.031\ \hbar$ ps^{-1}	Ref [5]

Table 1.2: Various parameters involved in calculating $|V_{td}|$ from Δm_d.

Equation 1.42 for $|V_{td}|$ gives

$$|V_{td}| = \frac{\pi}{G_F\ m_W\ f_B B_B^{1/2}} \sqrt{\frac{6\ \Delta m_d}{\eta_B\ m_B\ S(\bar{m}_t/m_W)}} \tag{1.44}$$

where $|V_{tb}|$ has been assumed to be 1. The calculation yields

$$|V_{td}| = (8.6 \pm 1.8) \times 10^{-3} \tag{1.45}$$

where the uncertainty on $|V_{td}|$ is completely dominated by the uncertainty on $f_B B_B^{1/2}$, which is calculated using lattice QCD and QCD sum rules. The B decay constant

f_B can, in principle, be measured through the leptonic decay modes of the charged B meson ($B^+ \to l^+\nu$). In practice, however, this is very difficult since the leptonic decay modes are very rare due to the smallness of V_{ub} and helicity suppression.

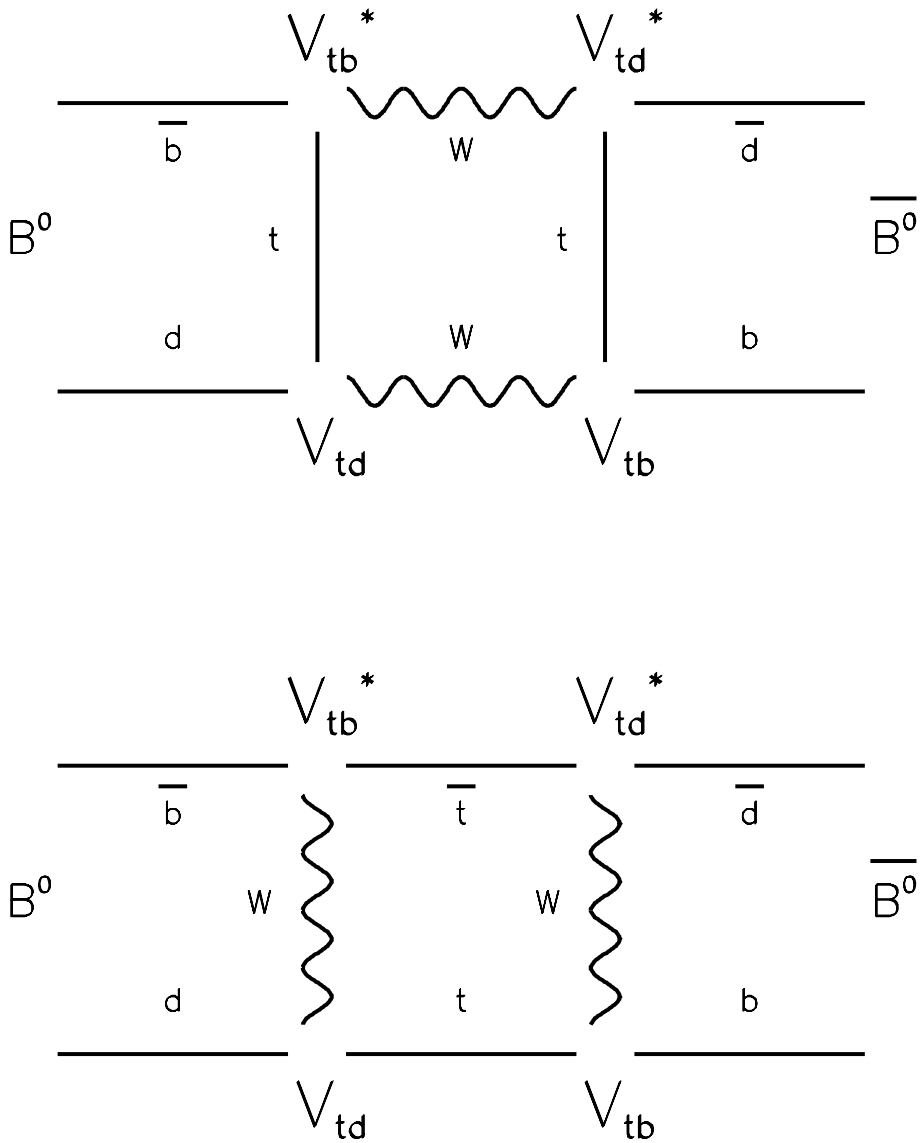

Figure 1.2: Box diagrams responsible for B^0 mixing. The amplitude of the diagram is proportional to $(V_{tb}V_{td}^*)^2$.

Chapter 2

The CDF Detector

This chapter gives a general description of the CDF detector with an emphasis on the elements relevant to this analysis. A detailed description can be found in reference [28]. The design philosophy for the CDF detector was rather simple: build a general purpose detector with as much solid angle coverage as possible. Figure 2.1 shows an isometric view of the detector. Figure 2.2 shows a 1/4 slice of the detector with more detailed labeling of the segmentation. The CDF coordinate system is defined in the upper left-hand corner of Figure 2.2. The proton direction defines the $\hat{z}$ or longitudinal axis. In the transverse plane looking in the proton direction, the 9 o'clock position defines the $\hat{x}$ axis and the 12 o'clock position the $\hat{y}$ axis. For the following discussion, we refer to Figure 2.2.

For this thesis, only the central ($|\eta| < 1.1$ or $37^0 < \theta < 143^0$) region of the detector was used [1]. The detectors that immediately surround the $p\bar{p}$ interaction point, which is in the lower right corner of Figure 2.2, all measure the trajectories of charged

[1] $\eta = -\ln\left(\tan\frac{\theta}{2}\right)$.

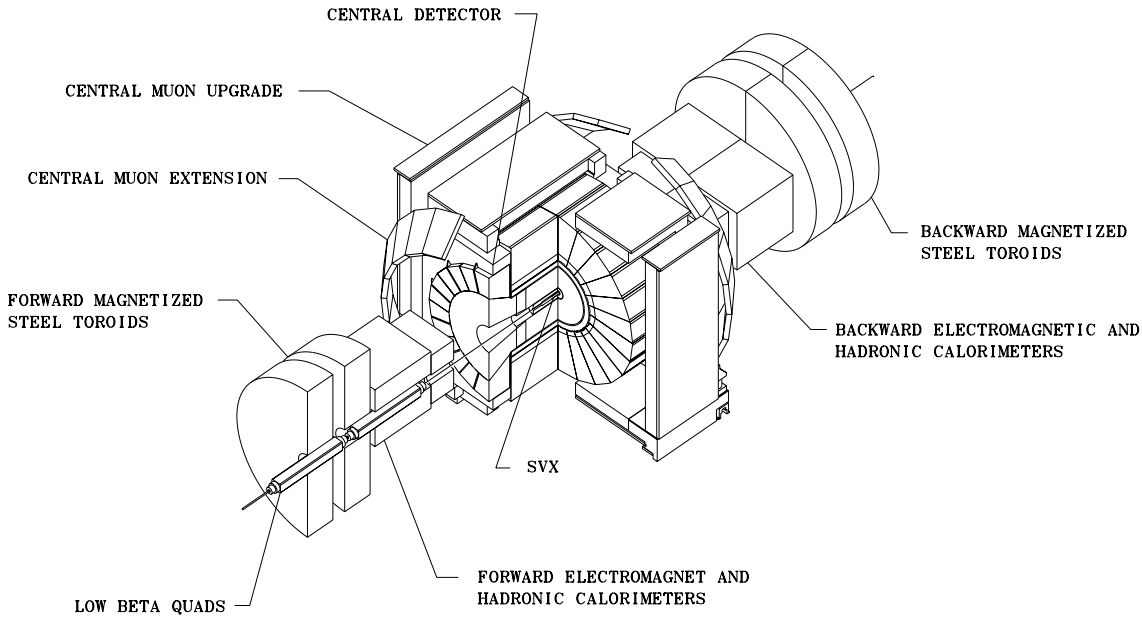

Figure 2.1: An isometric view of the CDF detector.

particles. They are, moving radially outward, the Silicon Vertex Detector (SVX), the Vertex TPC or the VTX, and the Central Tracking Chamber (CTC). The SVX provides up to four very accurate measurements close to the $p\bar{p}$ interaction point. This enables the positional measurement of the point at which a B hadron decays. This is done by searching for particles whose trajectories form a vertex which is separated from the $p\bar{p}$ interaction point. The $p\bar{p}$ interaction point is referred to as the primary vertex. Vertices from the decay of long lived particles are referred to as secondary vertices. The VTX provides the longitudinal (z) location of the $p\bar{p}$ interaction point. The CTC provides the main measurement of a charged particles trajectory. Out-

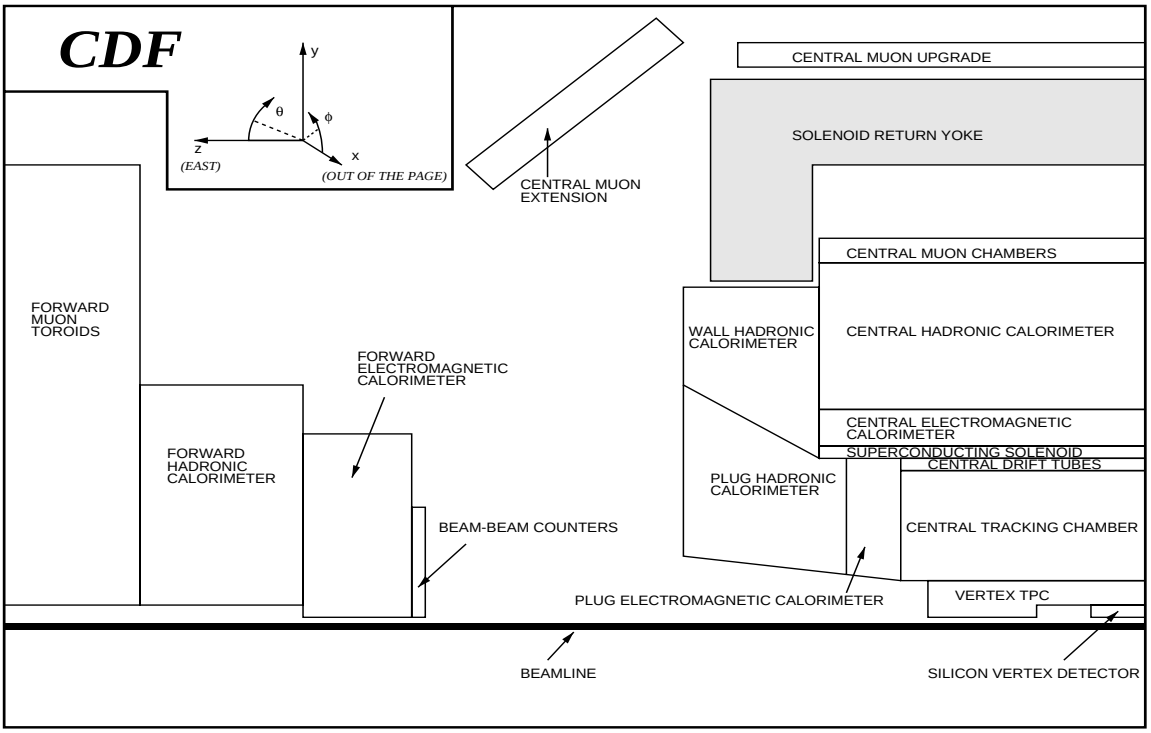

Figure 2.2: A 1/4 slice of the CDF detector. The image should be reflected to the right and below. The beam-beam interaction point is in the lower right of the figure.

side the charged particle tracking systems reside the electromagnetic and hadronic calorimeters. The electromagnetic calorimeter is used to identify electrons. Outside the calorimeters resides two sets of muon chambers behind an average 5.4 and 8.4 pion interaction lengths of material.

The detector can record events at a maximum rate of about 1 to 4 per second, which is limited by the maximum rate at which the events can be recorded on tape for storage. Since there is a $p\bar{p}$ interaction every 3.5 μs, decisions about which events to

keep must be made very quickly. There are several "triggers" built in to the detector read out which recognize the presence of interesting objects, such as electrons and muons, in an event. If an event passes a trigger, it is fully read out and written to tape.

2.1 Tracking

Tracking in CDF consists of three major systems: the Silicon Vertex Detector (SVX), the Vertex time projection chambers (VTX), and the Central Tracking Chamber (CTC). The SVX provides high precision position measurements close to the interaction point, enabling the detection of secondary vertices from the decay of long-lived particles. The VTX is used for finding the location of the primary interaction in the longitudinal (z) direction. The CTC provides tracks for track-based triggers, and gives the main track helix measurement used in the extrapolation into the SVX and the outer detectors. Below, the SVX and CTC are discussed in more detail.

2.1.1 CDF Coordinates and Track Helix Parameters

Before discussing the tracking detectors, the CDF Coordinates and track helix parameters are defined for clarity. The trajectory of a charged particle in the uniform magnetic field in the longitudinal (z) direction is a helix whose axis is in the longitudinal direction. The projection of the helix in the transverse ($x - y$) plane is a circle.

Figure 2.3 shows the path of a helix in the transverse plane. The circle radius is given by $1/2C$ where C is the curvature. The distance of the point of closest approach to the origin defines the impact parameter D_0. The tangential direction of the circle at the impact parameter point defines ϕ_0. The z position at the impact parameter point defines z_0. Finally, the last track parameter is the cotangent of the polar angle θ or $\cot(\theta)$ at the impact parameter point.

The translation of the helix parameters into the momentum of the particle naturally separates into a transverse $(x - y)$ and a longitudinal (z) component. The transverse component of the momentum is given by

$$P_t = \frac{c \cdot B}{2C} \times 10^{-9} \tag{2.1}$$

where P_t is in units of GeV/c, c is the speed of light in m/s, $B = 1.4$ tesla, and the curvature C is in m^{-1}. The longitudinal component is given by

$$P_z = \cot(\theta) \cdot P_t. \tag{2.2}$$

2.1.2 The Silicon Vertex Detector (SVX)

The silicon vertex detector (SVX) uses modern lithography technology and the silicon pn junction to create a detector capable of position measurements on the order of 10 μm in resolution. Finely spaced strips of strongly doped p-type silicon (p^+) are deposited on a lightly doped n-type silicon (n^-) substrate. On the opposite side, a

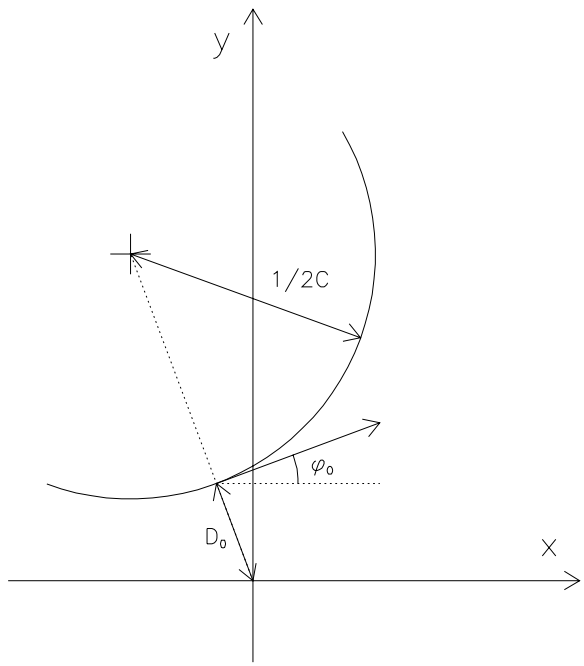

Figure 2.3: A helix in the transverse plane with the impact parameter D_0 and initial phi ϕ_0 labeled. The radius of the helix is $1/2C$, where C is the curvature.

thin layer of strongly doped n-type silicon (n^+) is deposited. A positive voltage is applied to the n^+ side, which depletes the n^- substrate of free electrons and creates an electric field in the volume of the n^- substrate. A charged particle that passes through the silicon leaves a trail of electron/hole pairs from ionization. The holes drift to the p^+ strips producing an electric signal, which is read out by an integrated circuit at the end of the silicon strip. Figure 2.4 illustrates a cross section view of a generic silicon detector.

The SVX is composed of two cylindrical assemblies called "barrels". The barrels

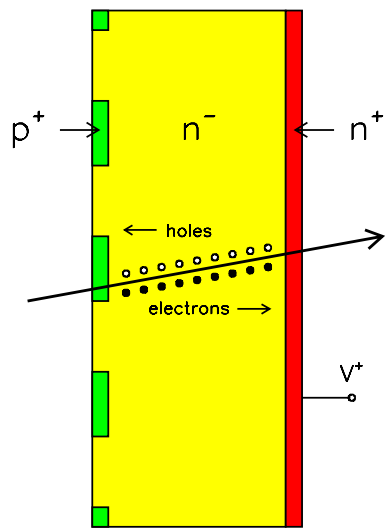

Figure 2.4: A generic silicon detector. The bias voltage V^+ applied to the n^+ side depletes the n^+ volume of free electrons and creates an electric field. A charged particle passing through the detector leaves a trail of electron/hole pairs, where the holes are collected at the p^+ strips.

are positioned end-to-end along the beam axis and centered longitudinally in the detector. Each barrel has 4 cylindrical layers staggered in radius. Each layer is composed of 12 planes of silicon called "ladders." Each ladder has three silicon wafers with microstrips in the longitudinal direction. The microstrips for the wafers are microbonded together between the wafers and to the integrated circuits which record the signals. Table 2.1 lists some of the features of the SVX.

The high precision position measurements from the SVX directly translate into a very accurate measurement of the track impact parameter D_0. A charged particle that crosses the silicon plane usually creates a signal in a small cluster of strips, rather

Layer	Radius (cm)	Pitch (μm)	Number of strips per Wafer
0	2.94	60	256
1	4.37	60	384
2	5.84	60	512
3	8.07	55	768

Table 2.1: Geometry and strip multiplicity of the SVX silicon wafers. The pitch is the spacing between microstrips.

than just one. The crossing point, transverse to the strip direction, is found from the weighted average of the charge recorded in the cluster of strips. The accuracy of the position measurement in each plane of silicon is around 12 μm. For high P_t tracks ($P_t > 5$ GeV/c) with hits in all 4 silicon planes, the impact parameter resolution is around 16 μm.

Figure 2.5 shows an event display for the SVX. The display is an end on view of the detector. Clusters of hits are represented by little ticks. The center shows the track extrapolations near the primary interaction. Figure 2.6 shows an enlargement near the primary interaction. The arrows represent tracks with SVX information, where the arrow length is proportional to the track P_t. The solid tracks are part of a reconstructed secondary vertex from the decay of a long-lived particle. This particular

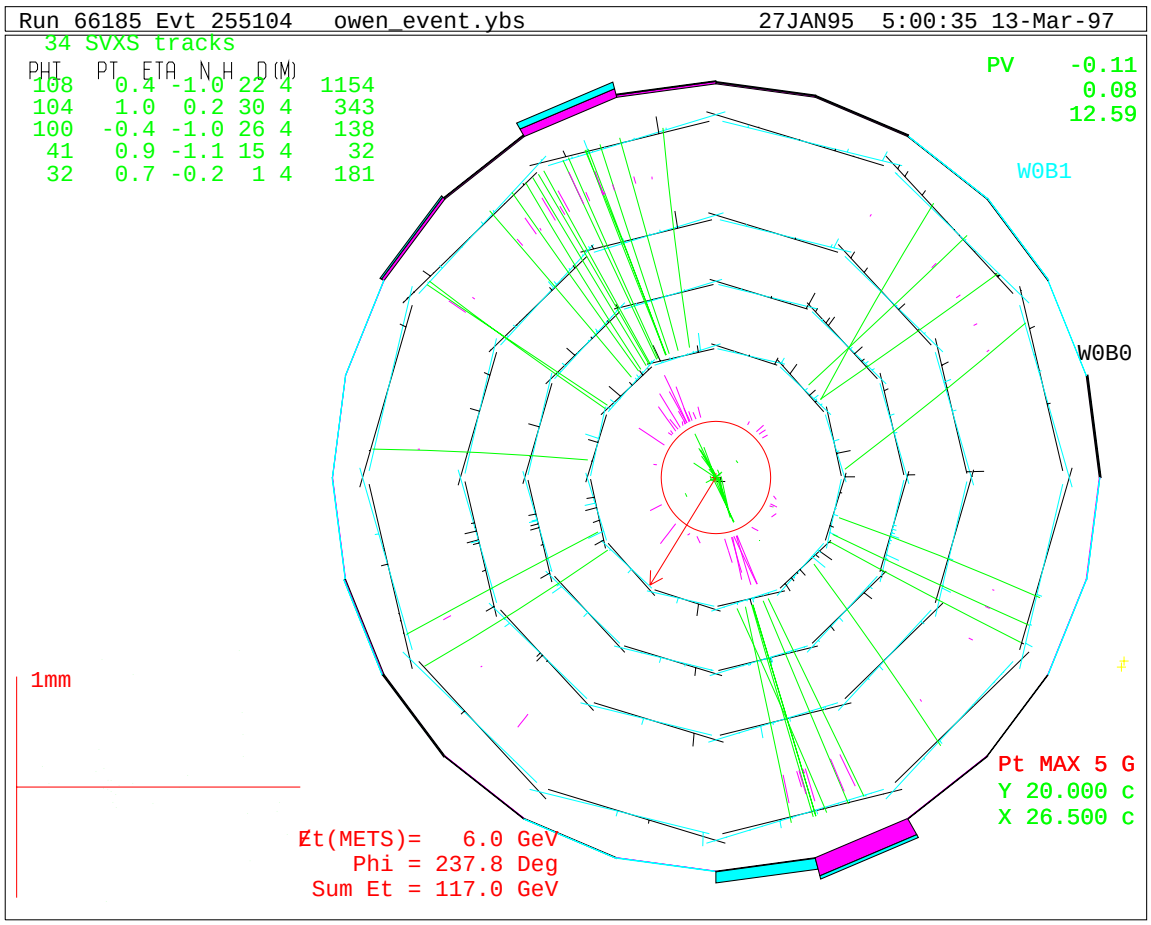

Figure 2.5: A SVX event display.

event clearly shows two back-to-back jets with secondary vertices; the classic signature for b–$\bar{b}$ production. The vertexing technique is discussed in later sections.

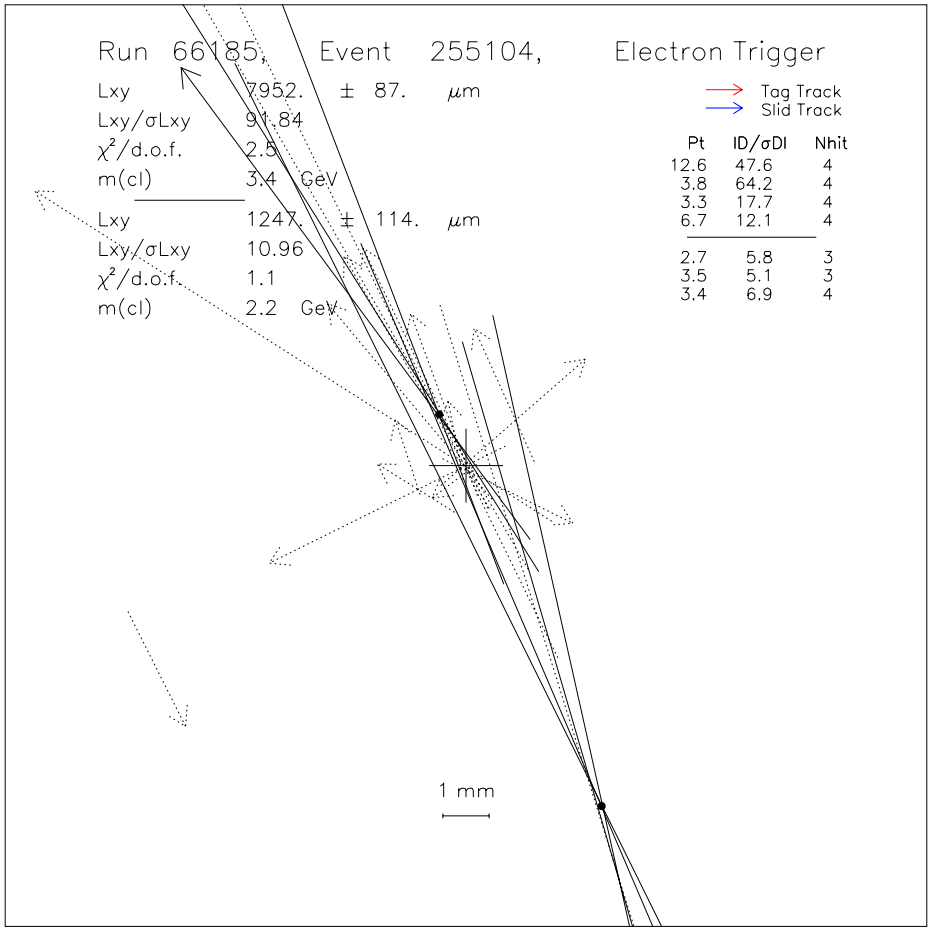

Figure 2.6: A SVX event display.

2.1.3 The Central Tracking Chamber (CTC)

The CTC is a cylindrical multi-wire drift chamber 3.214 m long with an active area from 0.309 m to 1.320 m in radius. Charged particles that pass through the CTC

ionize the argon/ethane gas leaving a trail of ionization electrons. The electrons drift in crossed electric and magnetic fields in the ϕ direction at constant velocity toward the sense wires. When the electrons get near the sense wires, they accelerate in the local $1/r$ electric field causing more ionization. These secondary ionization electrons form an "avalanche" producing a signal (or "hit") on the sense wire that is shaped and further amplified by electronic circuits at the end of the sense wire. The position in ϕ of the track with respect to the sense wire is inferred from the arrival time of the signal.

A charged particle that traverses the entire CTC radially will have 84 position measurements. The sense wires are arranged in 9 radially spaced superlayers of cells. Each cell is composed of a plane of wires tilted by 45^0 with respect to the radial direction. This is illustrated in Figures 2.7 and 2.8 which show the wire positions for a cell and the slots for each cell in the aluminum endplate respectively. The distance traveled by the ionization electrons is measured from the arrival time of the signal. However, there is an ambiguity as to the direction in ϕ from which the ionization electrons came. The tilt gives a distinct pattern of drift times in the cell for high P_t tracks, which facilitates the correct resolution of the left/right ambiguity for each hit. The superlayers alternate between axial (parallel to the beam direction) alignment and small angle ($\pm 3^0$) stereo alignment, where the tilt angle is a rotation about an axis in the radial direction. The stereo layers enable the CTC to measure the helix

polar angle or $\cot(\theta)$. Table 2.2 gives some features of the CTC.

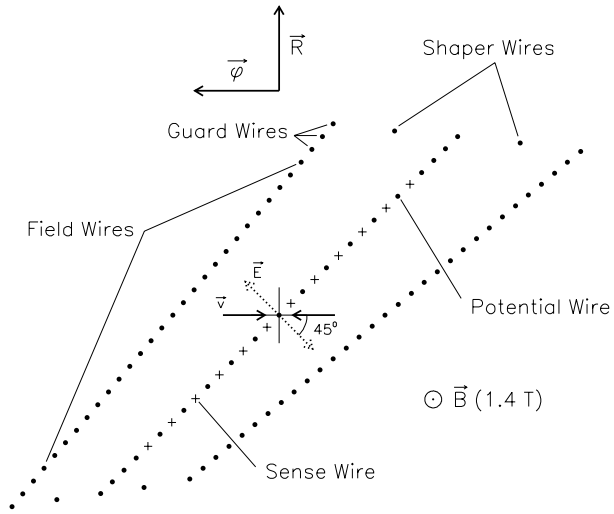

Figure 2.7: The wire positions for an axial superlayer cell of the CTC.

The individual hit resolution for the CTC is around 200 μm in $r - \phi$ and 4 mm in $r - z$. The transverse momentum resolution for the CTC is

$$\delta P_t / P_t = 0.002 \times P_t, \tag{2.3}$$

where P_t is in GeV/c. If the track also has SVX information, the P_t resolution is better by a factor of 2.

The pulse height information for the sense wires in superlayers 4, 6, and 8 is encoded in the discriminated pulse width, which is read out by the TDCs (Time to Digital Converter). This corresponds to a measurement of the energy loss through ionization of the gas per unit length (dE/dx) . The dE/dx of a charged particle is a

Super Layer	Sense Wires per Cell	Number of Cells	Stereo Angle	Cell Center Radius (cm)
0	12	30	0^0	34.64
1	6	42	$+3^0$	46.39
2	12	48	0^0	58.24
3	6	60	-3^0	69.88
4	12	72	0^0	81.65
5	6	84	$+3^0$	93.25
6	12	96	0^0	104.92
7	6	108	-3^0	116.49
8	12	120	0^0	128.11

Table 2.2: Some features of the CTC.

function of $\beta\gamma = P/m$. The momentum and dE/dx measurements in the CTC can be combined to infer the particles mass. As will be shown, the dE/dx is effective for distinguishing electrons from hadrons on a statistical basis. That is, the fraction of electrons and hadrons can be measured in a large sample of tracks. However, the dE/dx resolution is not sufficient to distinguish muons from pions, since their masses are fairly close (106 and 140 MeV/c^2 respectively).

Figure 2.9 shows the CTC display for the event shown in Figures 2.5 and 2.6.

Hits are shown as small black dots. For each real hit there are two shown, each the same distance in ϕ from the wire. Because of the 45^0 tilt in the cell planes, the left/right ambiguity for each hit is easily resolved. This signature "X" pattern can be clearly seen in top of the enlargement on the left hand side for the track in the middle. One can see that not all of the hits are associated with tracks. Tracks with $P_t < 0.275$ GeV/c curl up inside the CTC and do not reach reach the outer edge. The offline track reconstruction software does not attempt to reconstruct these low momentum tracks.

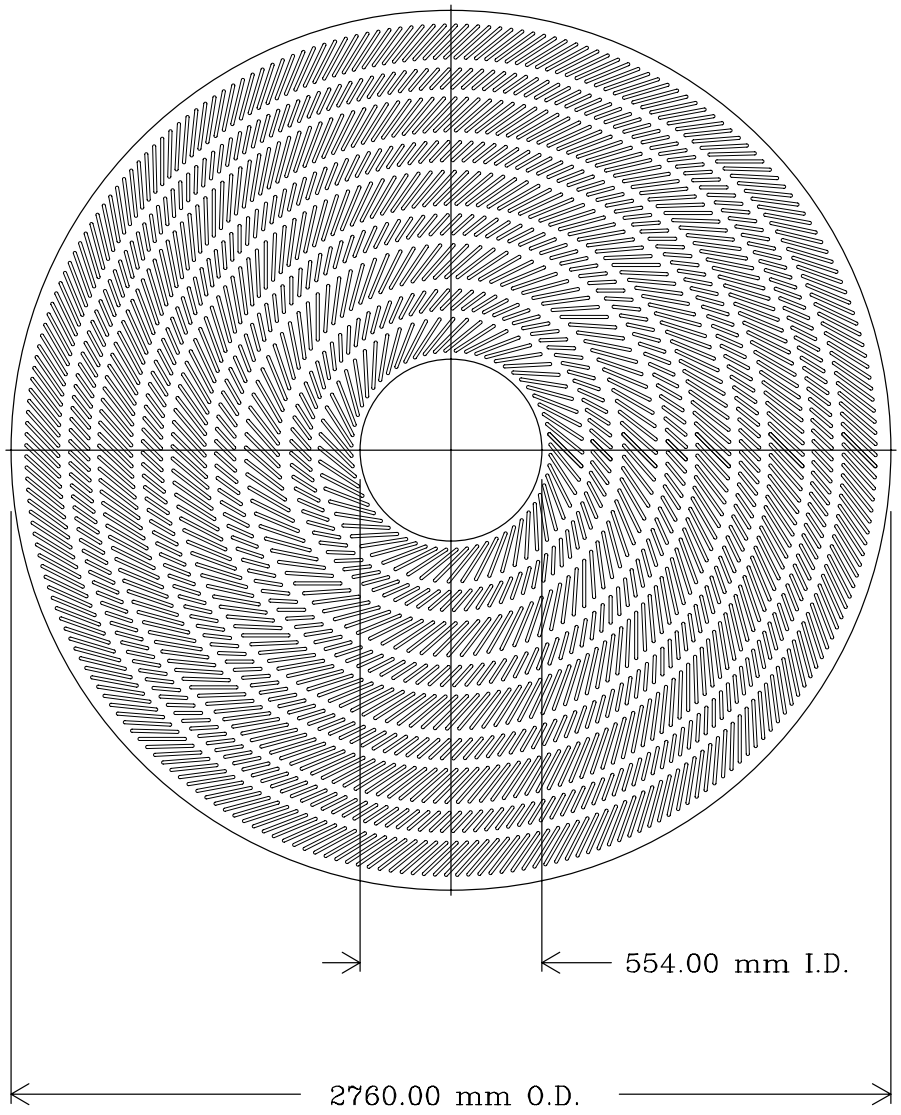

Figure 2.8: CTC aluminum endplate showing the cell slots.

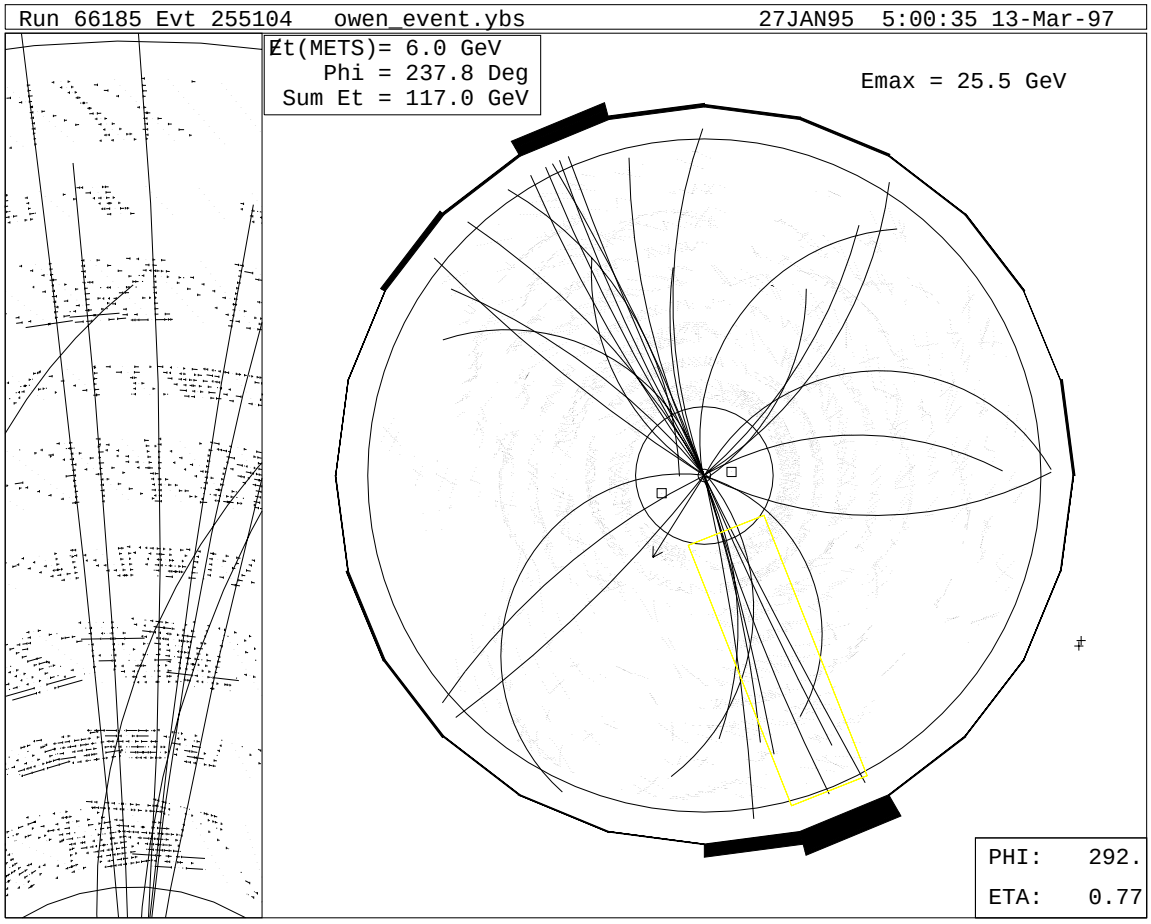

Figure 2.9: A CTC event display.

2.2 The Central Electromagnetic Calorimeter (CEM)

The central electromagnetic calorimeter (CEM) resides just outside the superconducting solenoid in radius. In this analysis, the CEM is used to trigger on and identify electrons. A moderate energy ($E > 100\ MeV$) electron passing through matter will emit photons through bremsstrahlung. These photons convert to electron-positron pairs, which in turn emit more photons through bremsstrahlung. This process continues until the electron and positron energies reach around 10 MeV where they begin to lose energy via ionization rather than bremsstrahlung. The concept of the electromagnetic shower is illustrated in Figure 2.10.

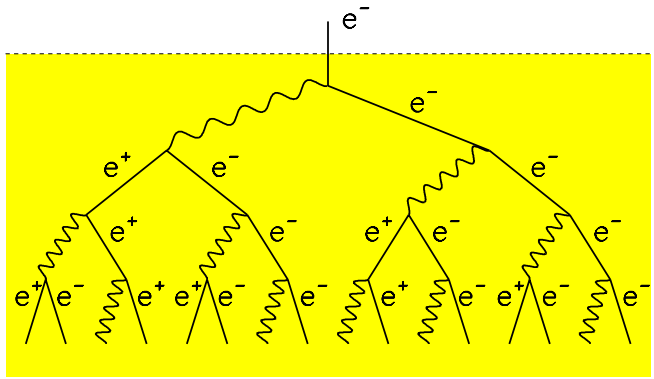

Figure 2.10: An illustration of an electromagnetic shower.

The CEM is composed of alternating layers of lead and scintillator. The shower develops mainly through interactions with the lead. The electrons and positrons excite the organic molecules in the scintillator which then emit blue light. The light

is collected with wavelength-shifting plastic and detected in photomultiplier tubes. The wavelength shifting plastic shifts blue light to green, which is a more optimal wavelength for the phototubes. The total amount of light collected is proportional to the initial electron energy.

At a depth corresponding to the position of average maximum transverse shower development, lies a gas chamber of orthogonal strips and wires. This is used to measure the position and transverse development of the shower. The transverse shape of the shower is compared to electron test beam data in order to distinguish between electrons and hadrons.

The CEM is divided into 24 modules on each side (East and West), with each module covering 15^0 in the ϕ direction and 0 to 1.1 in η. The modules are segmented into 10 towers, each covering 0.11 in η. Each tower is made up of a lead-scintillator "sandwich" with a strip chamber in the middle. Figure 2.11 shows one CEM module.

The energy resolution of the CEM is given by the formula below:

$$\left[\frac{\delta E}{E}\right]^2 = \left[\frac{(13.5)\%\ \mathrm{GeV}^{1/2}}{\sqrt{E_T}}\right]^2 + [(1.0 \pm 1.0)\%]^2 \tag{2.4}$$

The first term is from statistical fluctuations in the number of particles produced in the shower and was measured with an electron test beam. The second term was determined from a sample of 259 $Z \rightarrow e^+e^-$ decays [42].

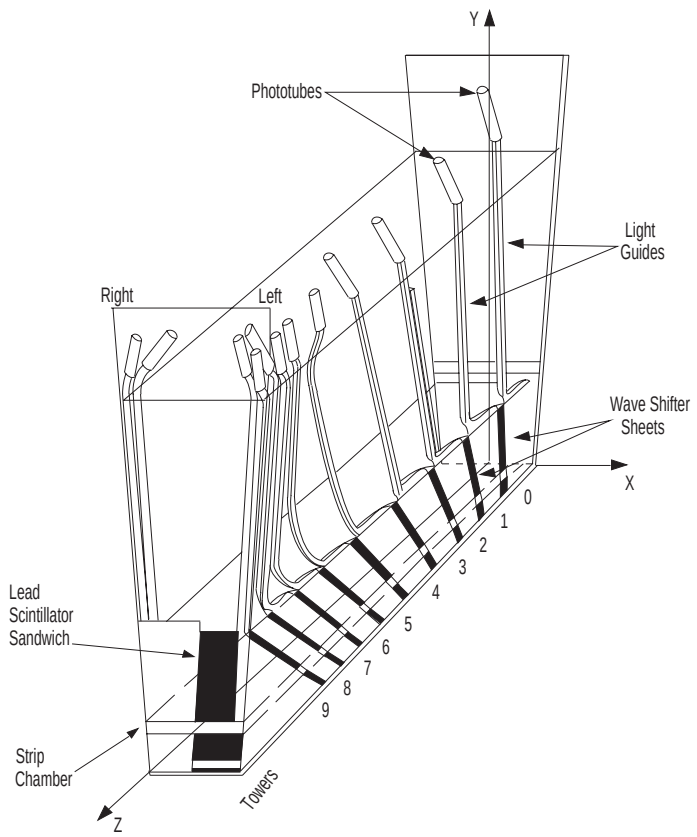

Figure 2.11: A central electromagnetic calorimeter (CEM) wedge.

2.3 The Central Fast Tracker (CFT)

Both the e and μ triggers require the presence of a track in the CTC. The bunch crossing period is 3.5 μs, requiring a very fast tracker. The Central Fast Tracker (CFT) is a hardware tracker which uses hits in the axial superlayers of the CTC and pre-programmed hit patterns to reconstruct tracks and provide a level 2 trigger. The hits considered come from two coincidence gates following the beam crossing: a

"prompt" gate from 0-80 ns and a "delayed" gate from 500-650 ns [2].

A CFT candidate track begins with a prompt hit in the outer superlayer (layer 8). Patterns of hits ("roads") in the inner layers consistent with the hit in layer 8 are formed from lookup tables corresponding to several P_t ranges. The prompt hits are considered in the first pass. If the hits in the detector form an acceptable match with one of the road patterns, a level 2 trigger is generated after the first pass. In the second pass, the delayed hits are also considered. The CFT decision time is typically 1 to 6 μs.

2.4 The Central Muon Detectors

Because the muon mass is about 200 times that of the electron and the fact that the radiation length is proportional to M^2, energy loss through bremsstrahlung for muons is entirely negligible (except for very high energies). For a 10 GeV muon, the total energy loss per unit length is more than three orders of magnitude less than that of a 10 GeV electron. Because of this, muons with moderate transverse momentum ($P_t > 2.7$ GeV/c) completely penetrate the central calorimeter. Muon detectors take advantage of the muons large penetrating power: anything that reaches them is most likely a muon.

The central region ($\eta < 0.7$) in CDF is instrumented with two independent muon

[2] The maximum possible drift time is around 800 ns.

detection systems: the central muon chambers (CMU) and the central muon upgrade (CMP). The CMU chambers lie outside the central electromagnetic and hadronic calorimeters, which provide an average of 5.4 pion interaction lengths [3] of material. The CMP chambers are further outside the detector behind an additional 60 cm of steel for a total of 8.4 pion interaction lengths of material.

The central muon chambers consist of rectangular drift cells with sense wires strung in the z direction. A muon traveling in the radial direction will pass through 4 drift cells. The drift time of the ionization electrons gives the distance in ϕ from the sense wires. The 4 sense wires are staggered in ϕ to resolve the left-right ambiguity. The position in z is determined using charge division. The central muon upgrade consists of an additional 4 layers of rectangular drift cells, similar to the drift cells used for the CMU.

2.5 Triggers

The CDF detector has a 3 level triggering system, with each level increasing in sophistication. For moderate luminosities, the input rate into the first level of the trigger is 300 Khz. The level 1 trigger looks for signs of an interaction, such as hits in the beam-beam counters or energy in the calorimeter. The output rate of the level 1 trigger is about 1 Khz.

[3] For a material with a pion interaction length l_0, the probability that a pion penetrates to a depth x without interacting is e^{-x/l_0}.

The level 2 trigger has the output of the CFT, calorimeter, and muon chambers (among other things) at its disposal. The detector is fully read out for all events that pass the level 2 trigger. The output rate of the level 2 trigger is about 20 to 30 Hz.

The level 3 trigger has the full event information from the detector. Because it has the full event information, the triggers for more complex physics signatures, such as $t\bar{t}$ events, are in level 3. The output of the level 3 trigger is about 1 to 4 Hz and is limited by the rate at which the events can be written to tape.

2.5.1 The Inclusive Electron Trigger

The inclusive electron trigger requires an electromagnetic energy cluster with at least 8.0 GeV of transverse energy (E_t). In addition, the ratio of the total E_t (electromagnetic and hadronic) over the electromagnetic E_t for the three calorimeter towers that contain the cluster must be less than 1.125. There must also be a CFT track with at least 7.5 GeV/c of transverse momentum pointing at the electromagnetic energy cluster, where the track matching is done using the wires in the CES. Because of limitations on how fast data can be written to tape, some triggers are "prescaled", which means they are written to tape only a fraction of the time. The inclusive electron trigger had a nominal prescale value of 2 (half the time it was written to tape) and a dynamic prescale that varied from 1 to 8, depending on the Tevatron luminosity. The cross section for the inclusive electron trigger was about 200 nb after prescaling.

2.5.2 The Inclusive Muon Trigger

The inclusive muon trigger requires a CFT track with at least 7.5 GeV/c of transverse momentum pointing at hits in the central and upgrade muon chambers. The extrapolation of the CFT track to the location of the muon chambers and the location of the hits in the muon chambers are required to agree within 5^0. The nominal prescale was 8, with the dynamic prescale ranging from 1 to 32. The cross section for the inclusive muon trigger is about 100 nb after prescaling.

Chapter 3

The Data Samples

In a proper time dependent B^0 mixing measurement, each event must have:

1. Identification of the flavor (whether it was a B^0 or a $\bar{B}^0$) at the time of decay for the B meson whose proper time is measured.

2. A measurement of the proper time t at decay for one of the B mesons in the event.

3. Identification of the initial flavor of the B meson whose proper time is measured.

The sign of the charge of a lepton from a semileptonic B decay is the same as the sign of the b quark that produced it. This means positively (negatively) charged leptons come from the semileptonic decay of B ($\bar{B}$) mesons [1]. The data from the inclusive lepton triggers (e and μ) are ideal for a B^0 mixing measurement for two reasons. First, they provide a sample of data which is enriched in $b\bar{b}$ events where one of the B mesons decays semileptonically. This is significant, considering that $b\bar{b}$ production

[1] Recall that the b quark charge is -1/3 and that a B ($\bar{B}$) meson contains $\bar{b}q$ ($b\bar{q}$).

makes up less than 1 % of the total inelastic $p\bar{p}$ cross section. Second, the trigger lepton charge identifies the flavor of the B meson at decay, satisfying requirement 1.

The second requirement is met by measuring the point of decay in the transverse $(x - y)$ plane for the B meson that produced the trigger lepton. This is done by searching for tracks close to the trigger lepton that form a vertex which is separated from the point of the $p\bar{p}$ collision. A measurement of the separation between the $p\bar{p}$ interaction (the primary vertex) and the B meson decay point (the secondary vertex) in the transverse plane (L_{xy}), combined with an estimation of the B mesons transverse momentum ($P_t(B)$), enables the calculation of the proper time at decay t.

The third and last requirement is to identify the initial flavor of the B meson that produced the trigger lepton. To do this, we have two methods which take advantage of the fact that b quarks are produced in $b\bar{b}$ pairs. If a second, perhaps lower momentum, lepton is present, we assume that it came from the semileptonic decay of the other B meson (not the one that produced the trigger lepton), thus it's charge is the flavor tag and the event is "soft lepton" tagged. If a soft lepton isn't present, we calculate the jet charge of a jet which we assume is from the other B in the event. The sign of the jet charge is correlated with the sign of the b quark that produced the jet, thus the sign of the jet charge provides the flavor tag and the event is "jet charge" tagged. The flavor tagging methods are discussed in detail in the following chapters.

This chapter discusses the inclusive lepton data, the algorithm for finding secondary vertices, and how the fraction of events which are from $b\bar{b}$ production is determined. Possible sources of inclusive lepton events, once the secondary vertex requirement is made, are:

$b\bar{b}$ production:

- **$b \rightarrow l$.** Most of the time, the event is from $b\bar{b}$ production where the lepton is from the semileptonic decay of one of the B mesons. This also referred to as direct decay.

- **$b \rightarrow c \rightarrow l$.** The lepton may come from the semileptonic decay of a charm hadron, which is the decay product of a B meson. The lepton is said to have come from a sequential decay in this case because it did not come directly from the B meson.

- **$b \rightarrow$ fake lepton.** The trigger lepton may actually be a hadron that appears to be a lepton in the detector. For example, a $\pi^{\pm}$ that begins it's hadronic shower early in the electromagnetic calorimeter may be identified as an electron. Also, a $\pi^{\pm}$ or $K^{\pm}$ may traverse the entire detector without interacting hadronically, thus faking the behavior of a muon. A $\pi^{\pm}$ or $K^{\pm}$ may also decay to a real muon before reaching the muon chambers. These are considered fake muons (even though they are real muons) because they do not come from the semileptonic

decay of a charm or B meson.

$c\bar{c}$ production: Like the B mesons, the charm mesons have relatively long lifetimes (0.4 to 1.0 ps). Recall that the lifetime of the B mesons is around 1.5 ps. This means that there will be events in the sample from $c\bar{c}$ production where one of the charm mesons decays semileptonically and lives long enough to give an observable secondary vertex. They are suppressed, relative to $b\bar{b}$ events, however due to the shorter lifetimes and the momentum requirements of the inclusive lepton triggers.

- $\boldsymbol{c \to l}$.
- $\boldsymbol{c \to}$ **fake lepton.**

Events in the sample may also come from light quark (u, d, or s) or gluon jets that give a fake lepton and fake vertex although the amount is negligibly small.

3.1 Offline Lepton Selection Criteria

Several offline lepton quality requirements are made to reduce contamination from fake leptons. Below, we outline these additional requirements for each trigger with a brief explanation for each.

3.1.1 The Inclusive Electron Trigger

- **Fiducial in the SVX:** The electron track is required to be within the fiducial volume of the SVX, since we later attempt to form a secondary vertex in the jet associated with the trigger electron.

- $\boldsymbol{P_t > 6.0}$ **GeV/c:** Although the CFT P_t requirement for the electron track is 7.5 GeV/c, we make a second offline P_t requirement at 6.0 GeV/c since the offline P_t resolution is an order of magnitude better. This requirement will remove any mistakes made by the CFT thus giving a well defined sample.

- $\boldsymbol{E_t > 7.5}$ **GeV:** Again, since the offline energy resolution is better, we make an offline E_t requirement to correct for any trigger mistakes for the purpose of having a well defined sample of data.

- $\boldsymbol{E_{\mathrm{had}}/E_{\mathrm{EM}} < 0.04}$**:** The three calorimeter towers which contain the electron shower are required to contain mostly electromagnetic energy. This removes hadrons which may fake electrons by showering early in the calorimeter.

- **Transverse shower profile shape:** The transverse development of the shower measured in the calorimeter towers is required to match expectations from electron test-beam measurements.

- $\boldsymbol{\Delta x < 1.5}$ **cm,** $\boldsymbol{\Delta z < 3.0}$ **cm of track and CES wire:** The extrapolation of the electron track into the CES is required to agree with the strip and wire

hits within 1.5 cm in x and 3.0 cm in z.

- **Strip and wire profile $\chi^2 < 10$:** The transverse shower development measured in the CES is required to match expectations from electron test-beam measurements.

3.1.2 The Inclusive Muon Trigger

- **Fiducial in the SVX:** See above.
- **$P_t > 6.0$ GeV/c:** See above.
- **CMU $\chi^2_x < 9$, $\chi^2_z < 12$:** The quality of the match between the muon track extrapolation and the hits in the CMU is evaluated with a χ^2. The χ^2 uses the difference between the track extrapolation and the hits in the CMU and the estimated error on the extrapolation from multiple scattering of the muon in the material of the detector.
- **CMP $\chi^2_x < 9$:** See above.

3.2 Monte Carlo Samples

Samples of $b\bar{b}$ and $c\bar{c}$ Monte Carlo were prepared for the determination of:

- The ratio of $b\bar{b}$ to $c\bar{c}$ events in the data through fits to kinematic distributions.
- The resolution on the measured decay length L_{xy}.

- The relation between the P_t of the trigger jet and the true P_t of the B hadron that produced the jet.
- The fraction of trigger leptons from sequential ($b \to c \to l\ \nu\ s$) decays.
- The effective lifetime of the $c\bar{c}$ data when the proper time at decay is reconstructed under the $b\bar{b}$ hypothesis.

Version 5.6 of the `PYTHIA` [43] Monte Carlo generator was used to produce our samples of $b\bar{b}$ and $c\bar{c}$ events for simulation. The minimum quark P_t cutoff was set to 8 and 15 GeV/c for $b\bar{b}$ and $c\bar{c}$ generation respectively. The Peterson fragmentation parameters used were $\epsilon_b = 0.006$ and $\epsilon_c = 0.06$. The bottom and charm hadrons were decayed using version 9.1 of the CLEO Monte Carlo `QQ` [44].

Events with a lepton with $P_t > 6$ GeV/c were kept and passed through a generator-level simulation of the CFT trigger turn-on as a function of P_t. Events passing the trigger simulation were passed on to the detector simulation.

A "fast" simulation of the CDF detector was used which is based on detector response models. Unlike detector simulation packages, such as `GEANT`, which trace the evolution of simulated particles through a detector in small steps, the fast CDF detector simulation uses resolution parameterizations based on the measured detector response, which are functions of the particle kinematics (P_t, E_t, ...). For example, in the fast CDF detector simulation, multiple scattering effects in the tracking are based on the particle P_t, rather than stepping through the material in the path of

the particle. Similarly, the electromagnetic calorimeter response is a function of the particle E_t and not a simulation of the electromagnetic shower.

Finally, the simulated events were required to pass the offline lepton quality criteria and the secondary vertex requirement for the trigger lepton jet, just like the real data.

3.3 Secondary Vertex Finding

In order to measure the proper time (t) of the B that decays to the trigger lepton, it is necessary to reconstruct the secondary vertex associated with the B decay. Track-based jets are formed using a cone clustering algorithm. Tracks within a cone about the lepton jet axis with significant displacement from the primary vertex are used in an attempt to form a secondary vertex. If a good vertex is found, the vertex is required to be significantly displaced in the transverse direction from the primary vertex. Below, is an outline of the details of the determination of the primary vertex location, the track-based jet algorithm, and the vertexing algorithm.

3.3.1 The Primary Vertex Location

The CDF database contains an average beam line position for each run (about 1 to 10 hours of data taking), which is accurate to about 35 μm (in x and y). The beam has a slight slope with respect to the z axis ($\partial x/\partial z = 5$ μm, $\partial y/\partial z = -4.4$ μm) so the z position of the primary vertex must be known in order to use the run-averaged

beam line position. The VTX provides the z position of the primary vertex. The run-averaged beam line position serves as a seed position for an event-by-event fit, using SVX tracks, for the primary vertex location.

The first iteration of the fit attempts to use all quality tracks ($P_t > 0.4$ GeV/c, at least 3 SVX hits, $|D_0| < 2.0$ cm) and the seed position to find a common vertex. Tracks are also required to be no greater than 5 cm from the seed position in z in order to avoid tracks from a second $p - \bar{p}$ interaction. The trigger lepton track is explicitly excluded from the fit since we are assuming it originated from a B decay and not the primary interaction. The fit is iterated, removing the track with the highest residual at the end of each iteration, until there are no tracks contributing more than 50 to the vertex χ^2. At this point, the iteration process is restarted, this time allowing the track parameters to float within their measured uncertainties.

3.3.2 Track-Based Jets

Track based jets are formed for each event using a cone clustering algorithm. Tracks with $P_t > 1$ GeV/c are considered seeds for jets. If two seeds are within ΔR [2] of 0.7 of each other they are merged together. After all seed merging, tracks with $P_t > 0.4$ GeV/c within ΔR of 0.8 around the jet are added to the jets. All tracks must pass several quality criteria listed in Table 3.1.

[2] $\Delta R = \sqrt{\Delta\eta^2 + \Delta\phi^2}$

Track Quality Criteria	
Requirement	Value
Max Δz w.r.t P.V.	5 cm
Min track P_t	0.400 GeV/c
Max $\|D_0\|$	0.2 cm
Min CTC Exit Radius	130 cm
Min hits in good Stereo Layer	2
Min hits in good Axial Layer	5
Min good Stereo Layers	2
Min good Axial Layers	2

Table 3.1: Track quality criteria for track clustering. The CTC exit radius is the radial position at which the track crosses the plane that defines the edge of the CTC in z.

3.3.3 The Secondary Vertexing Algorithm

The secondary vertexing algorithm is the same as that which was used in the top quark discovery at CDF [45] with some minor modifications. The method was originally designed to tag the high-P_t B jets in $t\bar{t}$ events with a minimum of fake tags. The modifications made take into account the fact that the B jets in our sample are softer and place more emphasis on efficiency rather than purity.

The vertex finding is done in two passes. In the first pass, the track criteria

are relatively "loose". A minimum of three tracks is required. The second pass has relatively "tight" criteria and only requires two tracks. Below, we describe the details of each pass.

Pass 1

Tracks that are associated with the trigger lepton jet ($\Delta R < 0.7$) are required to meet the following criteria:

- At least 2 axial CTC superlayers with at least 4 sense wire measurements.
- At least 2 stereo CTC superlayers with at least 2 sense wire measurements.
- Good SVX clusters (hits) are defined as:

  Not shared with any other track.

  No bad strips.

  No more than 3 strips in the cluster.
- Not consistent with coming from a K_s^0 or Λ.
- $|\Delta z| < 5$ cm from primary vertex.
- $|D_0| < 0.15$ cm with respect to primary vertex.
- χ^2/d.o.f < 6 for track fit to SVX hits.

- Tracks with two SVX hits must have both hits in the first two or last two layers of silicon.

- For tracks with two SVX hits, both hits must be good hits and the track must have $P_t > 1.5$ GeV/c.

- Tracks with three or four SVX hits must have at least one good hit and $P_t > 0.5$ GeV/c.

- $|D_0/\sigma_{D_0}| > 2.5$.

If only two tracks pass the above criteria, a third track is allowed if it passes all but the $|D_0/\sigma_{D_0}| > 2.5$ requirement. This is to increase the acceptance at low L_{xy}. The selected tracks are ordered based on the number of good SVX hits, P_t, and $|D_0/\sigma_{D_0}|$. Tracks with high $|D_0/\sigma_{D_0}|$ and P_t and a large number of good hits are placed first in the list and are considered first in the vertexing. The ordering scheme is illustrated in Figure 3.1.

Tracks in the list are combined in pairs, starting with the best tracks in the beginning of the list, in an attempt to form a seed vertex. The seed vertex must contain at least one track with $P_t > 2.0$ GeV/c. Once a seed vertex is found, we search for "attached" tracks in the list, where an attached track is required to have it's closest distance of approach to the seed vertex in the x-y plane be within 3 σ.

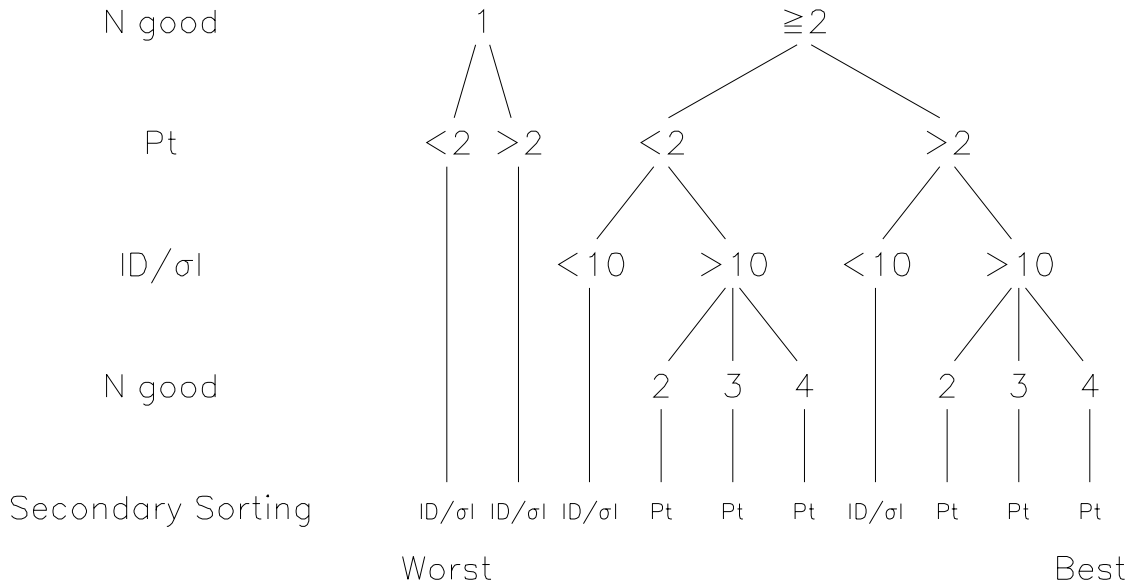

Figure 3.1: The ordering hierarchy for tracks to be considered in vertexing. Tracks with high $|D_0/\sigma_{D_0}|$ and P_t and a large number of good SVX hits are favored and considered first. Tracks in the same class are sorted by the Secondary Sorting variable.

If at least one attached track is found, we attempt to fit the seed plus attached tracks to a common vertex. If a track has a χ^2 contribution greater than 50, it is dropped and the fit is repeated until all tracks have a χ^2 contribution less than 50.

If at this point there are still three tracks in the vertex, we make two final requirements. First, the the two dimensional decay length L_{xy} must must have a significance greater than 2. That is, $|Lxy/\sigma_{L_{xy}}| > 2.0$. This is to remove fake vertices from random combinations of tracks. Second, L_{xy} must be less than 2.5 cm. A B hadron with $P_t = 40$ GeV/c has less than a 0.1 % chance of traveling more than 2.5 cm in

the transverse plane before decaying. Most of the vertices with $L_{xy} > 2.5$ cm are combinatoric mistakes or contain very poorly measured tracks.

Pass 2

If pass 1 fails, we go on to pass 2. Tracks considered for vertexing in pass 2 must pass all of the pass 1 quality criteria plus the following additional requirements:

- No 2 hit tracks.
- $P_t > 1.0$ GeV/c.
- $|D/\sigma_{D_0}| > 3.0$.
- 3 hit tracks must have a least 2 good hits.

The search for the seed and final vertex from this point on is the same as pass 1 with the exception that only two tracks are required. Two track vertices that are consistent with $K_s^0 \to \pi^+\pi^-$ and $\Lambda \to p^\pm\pi^\mp$ are removed.

The transverse decay length L_{xy} is defined as the two dimensional (x and y) distance between the primary and secondary vertices projected on to the jet axis. This is illustrated in Figure 3.2. It is possible for the measured L_{xy} to be negative. This can happen for two reasons. First, it could be a heavy flavor event where the vertex is poorly reconstructed, through both combinatoric mistakes (using the wrong

tracks) and poorly measured tracks. Second, it may not be a heavy flavor event in which case the vertex is most likely fake and entirely due to tracking resolution effects.

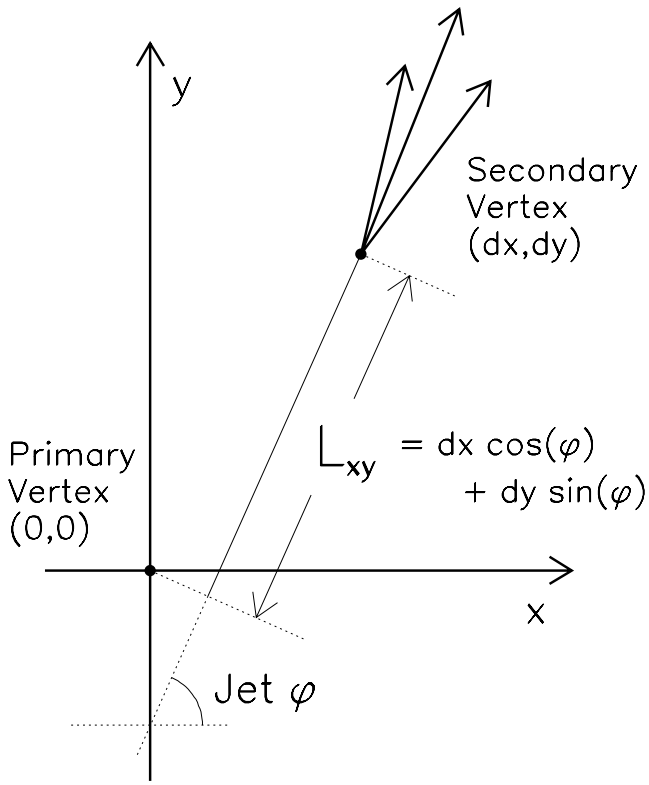

Figure 3.2: An illustration of the definition of the transverse decay length L_{xy}. Note that although only the secondary vertex tracks are shown, the tracking jet defines the jet axis. The jet axis may include tracks in addition to the secondary vertex tracks. The pointing error of the jet axis to the primary vertex has been exaggerated for clarity.

Figure 3.3 shows the reconstructed transverse decay length (L_{xy}) distributions for the data, $b\bar{b}$ Monte Carlo, and $c\bar{c}$ Monte Carlo for the e and μ triggers. The L_{xy} distributions show a discrepancy in the fraction of $L_{xy} < 0$ events between the data

and the Monte Carlo. Both the $b\bar{b}$ and $c\bar{c}$ Monte Carlo have about 2 % of the events with $L_{xy} < 0$, while this number is around 5 % in the data. We will show in the next sections that some of the discrepancy is from fake trigger electrons and trigger electrons from photon conversions, which are not present in the Monte Carlo samples.

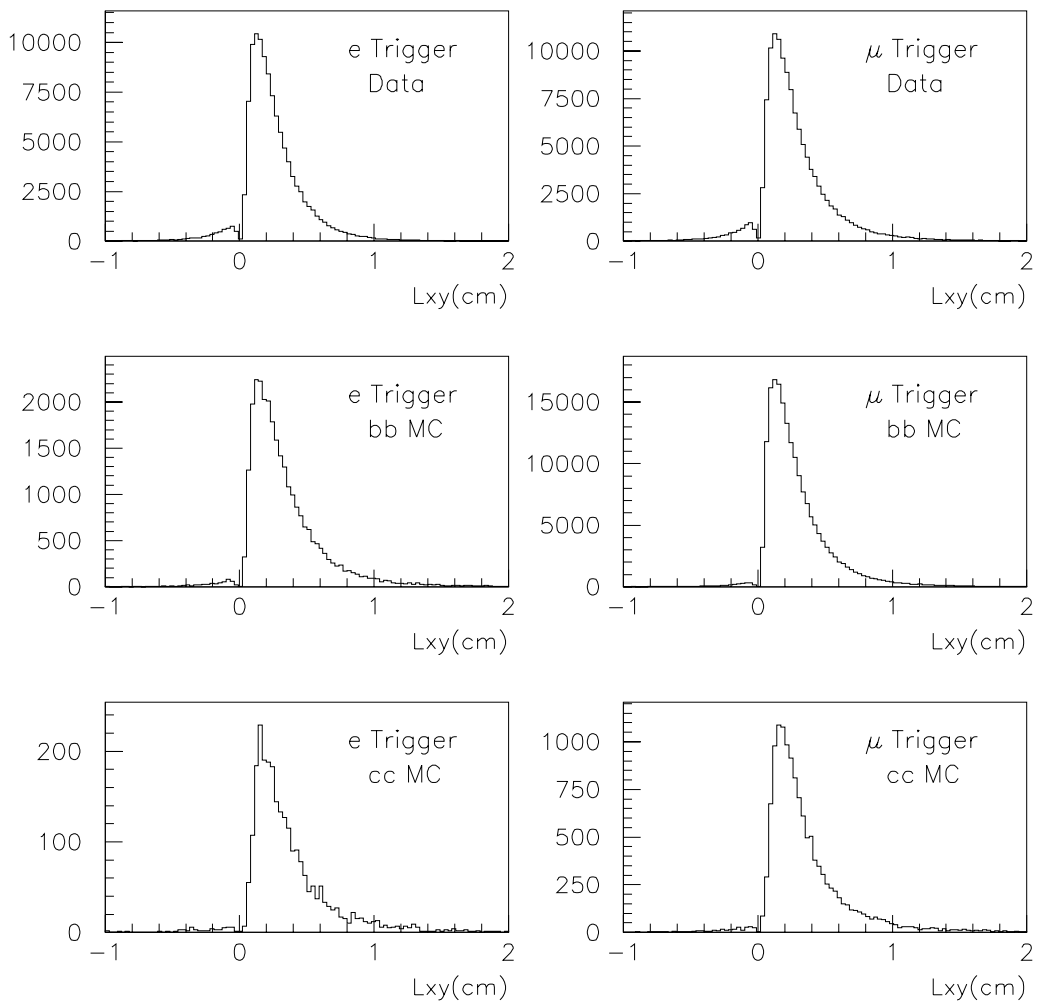

Figure 3.3: Reconstructed transverse decay length L_{xy} distributions for the electron (left) and muon (right) trigger data, $b\bar{b}$ Monte Carlo, and $c\bar{c}$ Monte Carlo.

3.4 Fake Trigger Electrons

Some of the trigger electrons are actually hadrons that fake electrons. The separation in dE/dx between electrons and hadrons (π, K, and p) is large enough to determine the number of fake trigger electrons (hadrons) by fitting the observed dE/dx spectrum in the data. Table 3.2 lists the average separation significance in dE/dx between e and π, K, and p for the trigger electron momentum spectrum. The number of sense wire measurements used in the dE/dx measurement (N_{CTC}) is required to be greater than 24 to ensure a high quality dE/dx measurement.

Average dE/dx Separation From e	
Particle	$\langle (dE/dx_{meas} - dE/dx_{pred}(e))/\sigma_{dE/dx} \rangle$
π	-0.7
K	-1.8
P	-2.5

Table 3.2: Average separation from e in dE/dx for particles with the trigger electron momentum spectrum.

Figure 3.4 shows the results of the fits of the trigger electron dE/dx spectrum where the data have been divided into $L_{xy} < 0$ and $L_{xy} > 0$ events. The fits give a fake electron fraction of 10.3 $\pm$ 3.6 % and 0.6 $\pm$ 0.5 % for the $L_{xy} < 0$ and $L_{xy} > 0$ events respectively. It's not surprising that the fake electron fraction is higher for the

events with $L_{xy} < 0$ since fake electrons events are more likely to also have a fake secondary vertex.

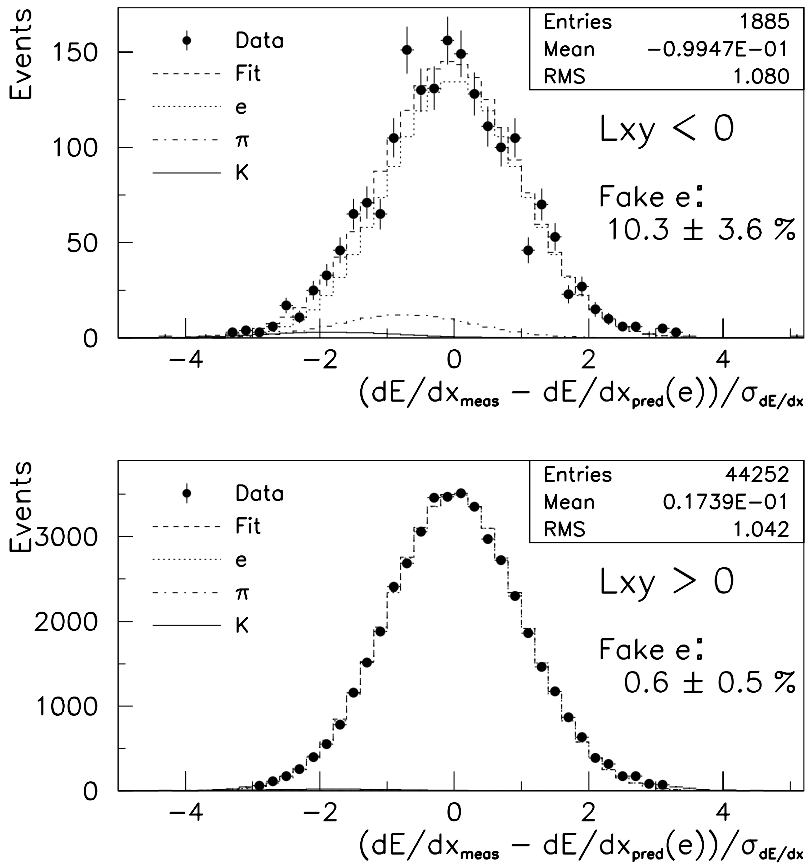

Figure 3.4: Results of the dE/dx fits for the e, π, K, and p fractions in the $L_{xy} < 0$ and $L_{xy} > 0$ events. The p curve was not plotted because the fits gave no statistically significant p fraction. The errors are statistical only.

3.5 Conversion Electron Removal

A small fraction of the trigger electrons are from photon conversions ($\gamma \rightarrow e^+e^-$). They are identified by searching for an oppositely charged track that forms a good vertex with the trigger electron. The tracks must be parallel, within the detector resolution, at the point of the vertex. The efficiency of the conversion finding algorithm for real conversions is estimated from the P_t and dE/dx spectra of the track that pairs with the trigger electron to form the conversion candidate. This track will be referred to as the conversion partner. The residual amount of trigger electrons from conversions that remain in the sample is estimated from the conversion finding efficiency.

Two sets of selection criteria, shown in Table 3.3, were used to evaluate the efficiency of the conversion identification algorithm for real conversion electrons. One set of criteria (the "loose" criteria) were chosen to be fully efficient in identifying real conversion electrons. However, the loose criteria also label many non-conversion electrons as conversion electrons, thus it's over-efficient. The second set of criteria (the "tight" criteria) are a compromise between reducing the over-efficiency and keeping the efficiency for real conversions high.

The dE/dx spectrum of the conversion partner is used to measure the number of real and fake conversions. As with the dE/dx fits for the trigger electrons, N_{CTC} is required to be at least 25 to ensure a quality dE/dx measurement. Figure 3.5

shows the results of the fit for the conversion events identified with the loose and tight criteria. The fit of the selected conversion events gives a real conversion fraction of 46 % and 74 % for the loose and tight criteria respectively.

Conversion Finding Cuts		
Parameter	Tight	Loose
$r - \phi$ Separation at point of tangency	0.2 cm	0.5 cm
Difference of cotangents	0.03	0.06
z Mismatch at point of tangency	2.0 cm	5.0 cm
Conversion radius	-5 cm to 50 cm	-10 cm to 50 cm
$\Delta\phi$ at radius of conversion	0.01	0.05
Pointing residual to origin	1.0 cm	1.0 cm

Table 3.3: Tight and loose cuts used in conversion finding.

Figure 3.5 shows that some of the over-efficiency of the conversion finding algorithm can be removed by requiring the conversion partner to be consistent with the electron hypothesis with the cut below

$$\frac{dE/dx_{meas} - dE/dx_{pred}(e)}{\sigma_{dE/dx}} > -2.0. \tag{3.1}$$

After this requirement, the real conversion fraction for the tight cuts is 86 %. This will be referred to as the conversion purity $P(cnv)$.

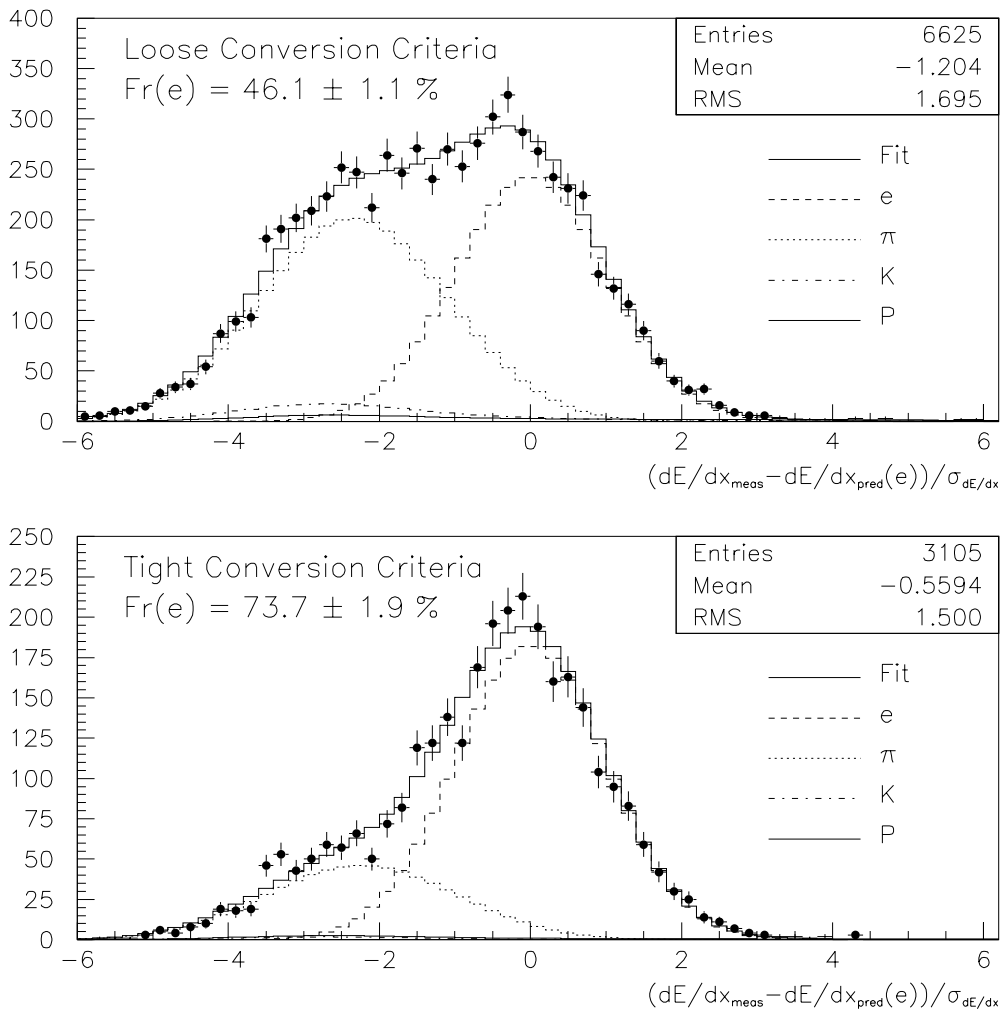

Figure 3.5: The conversion partner dE/dx spectra for loose (top) and tight (bottom) criteria.

If it is assumed that the loose cuts are fully efficient in finding real conversions, the efficiency of the tight cuts can be estimated by comparing the number of conversion partner electrons (real conversions) from the dE/dx fits for the loose and tight cuts. This efficiency, which will be referred to as $\epsilon_{cnv}(cut)$, is 75 %.

Some conversions are not identified because the conversion partner momentum is too low to be reconstructed in the tracking chamber. It is estimated, from the conversion partner P_t spectrum, that the efficiency for the conversion partner to be reconstructed in the tracking chamber ($\epsilon_{cnv}(P_t)$) is 82 %.

The amount of residual (unidentified) conversions left in the data N_{resid} is estimated with the following formula

$$N_{resid} = N_{tag} \cdot P_{cnv} \cdot \left(\frac{1}{\epsilon_{cnv}(cut)} \cdot \frac{1}{\epsilon_{cnv}(P_t)} - 1 \right) = N_{tag} \cdot 0.54 \tag{3.2}$$

where N_{tag} is the number of events tagged as conversions with the tight criteria.

The number of events with a trigger electron identified as a conversion electron with the tight criteria is 2,446. This is 2 % of the electron trigger data. Equation 3.2 gives an estimated 1,300 residual (unidentified) conversion events (1.1 %) in the electron trigger data.

3.6 Fake Trigger Muons

The amount of fake muons can be estimated by the effectiveness of the flavor taggers in the e and μ trigger data. The details of this estimate are in Appendix B since the estimate depends on information in the following sections. The analysis described in Appendix B yields a fake muon fraction of 12 ± 6 %.

A sample of single-track trigger data was used to study the L_{xy} and ct shape of events with a fake trigger muon. Since the only requirement for the muon trigger, other than hits in the muon chambers, is a high P_t track, these data should represent the behavior of hadrons that give a false muon signature. The only trigger requirement for these data was a CFT track with $P_t(\mathrm{CFT}) > 12\,\mathrm{GeV}/c$. The inclusive muon trigger used $P_t(\mathrm{CFT}) > 7.5$ GeV/c however, the difference in the P_t spectrum is negligible for our purposes. The vertexing procedure was applied treating the highest P_t track with $P_t > 7.5$ GeV/c as the trigger muon. Figure 3.6 shows the L_{xy} distributions for the single-track trigger sample, muon trigger data, and muon trigger $b\bar{b}$ Monte Carlo. Aside from the higher $L_{xy} < 0$ fraction, the single-track trigger sample is qualitatively very similar to the muon trigger data and $b\bar{b}$ Monte Carlo. This suggests that most of the fake muons are from $b\bar{b}$ events. This is not unreasonable since the secondary vertex requirement should remove most of the non-$b\bar{b}$ and $c\bar{c}$ events. Later, it will shown that the reconstructed ct distribution of the single-track trigger sample is also very similar to the muon trigger data and $b\bar{b}$ Monte Carlo.

The fake muon fraction can't be determined using dE/dx because the $\mu - \pi$ separation is very small due to the relatively small difference between m_μ and m_π (36 MeV/c^2).

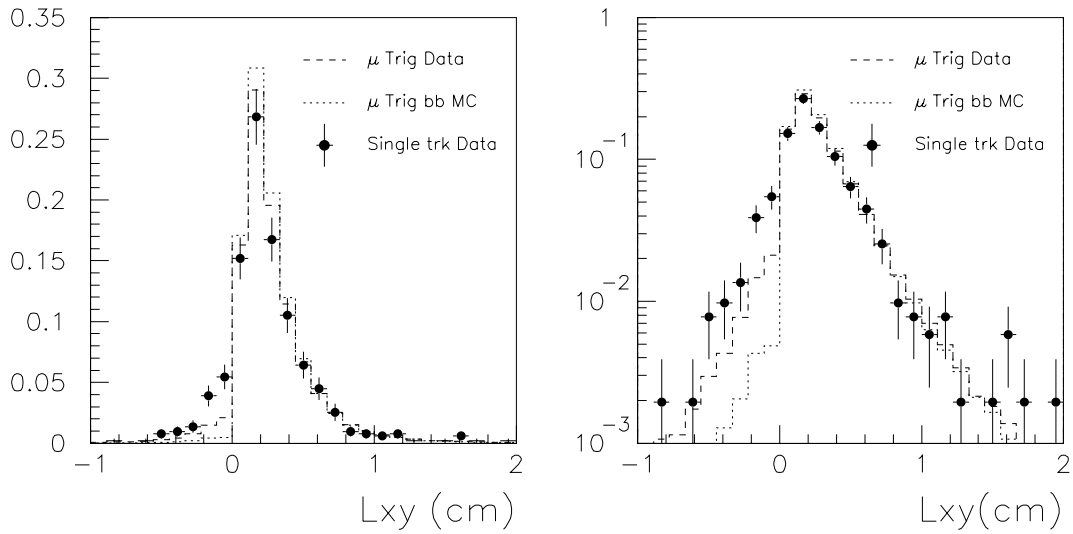

Figure 3.6: L_{xy} distributions for the single-track trigger sample, μ trigger data, and μ trigger $b\bar{b}$ Monte Carlo. All distributions are normalized to unit area.

3.7 Ratio of $b\bar{b}$ to $c\bar{c}$ Events

Our data set contains events from $b\bar{b}$ and $c\bar{c}$ production since both can satisfy the two requirements for the sample: a high P_t lepton (through semileptonic decay), and a secondary vertex associated with the lepton (both the charm and B mesons have relatively long lifetimes). The relative amount of $b\bar{b}$ and $c\bar{c}$ events must be determined since $c\bar{c}$ events will affect the mixed fraction of events. This is done using two kinematic quantities: the P_t(rel) of the trigger lepton and the invariant mass of the cluster of secondary vertex tag tracks (m(cl)). The P_t(rel) and m(cl) shapes for the $b\bar{b}$ and $c\bar{c}$ components are determined from the Monte Carlo samples. The $b\bar{b}$ to $c\bar{c}$ ratio is determined separately for the e and μ triggers and for the flavor tag subsets: jet charge single vertex, jet charge double vertex, and soft lepton.

The lepton P_t(rel) is defined as the component of the trigger lepton momentum perpendicular to the axis of the tracking jet that the lepton is associated with, where the lepton is not included in the calculation of the jet axis. This is illustrated in Figure 3.7. The usefulness of the P_t(rel) variable comes from the heavy mass of the b quark. The physical limit for P_t(rel) is the mass of either the bottom hadron (5.3 GeV/c^2) or charm hadron (1.9 GeV/c^2) that produced the lepton. This mass difference gives two distinct P_t(rel) distributions for $b\bar{b}$ and $c\bar{c}$ production which are used in a two component fit of the data P_t(rel) spectrum.

Figure 3.8 shows the results of the P_t(rel) fits. The fits show that the fraction

Electron Trigger				
	$P_t(rel)$ Fits		$m(cl)$ Fits	
Sample	$F_{b\bar{b}}$	$F_{c\bar{c}}$	$F_{b\bar{b}}$	$F_{c\bar{c}}$
JC, SV	89.6 ± 0.6 %	10.4 ± 0.3 %	92.2 ± 0.5 %	7.8 ± 0.3 %
JC, DV	94.5 ± 1.5 %	5.5 ± 1.0 %	96.7 ± 1.0 %	3.3 ± 0.5 %
SLT	91.3 ± 1.7 %	8.7 ± 1.2 %	94.4 ± 1.5 %	5.6 ± 0.8 %

Table 3.4: Results of the P_t(rel) and m(cl) fits for the $b\bar{b}$ to $c\bar{c}$ ratio in the electron trigger data for the jet charge single vertex, jet charge double vertex, and soft lepton flavor tag events.

of events from $b\bar{b}$ production is over 90 %. Note that the requirement of a second jet with a secondary vertex (jet charge double vertex) significantly increases the $b\bar{b}$ fraction.

The cluster invariant mass m(cl) is a useful tool in discriminating between $b\bar{b}$ and $c\bar{c}$ events, again, because of the heavy mass of the b quark. The cluster invariant mass is calculated from all of the secondary vertex tag tracks, assuming the pion mass for the non-lepton tracks. The lepton is included in the calculation of m(cl) even if it isn't a tag track since we are assuming it's a B daughter. The bottom or charm hadron is never fully reconstructed since the neutrino from the semileptonic decay and other neutral daughters always escape detection. Figure 3.9 shows the results of the m(cl) fits. The m(cl) and P_t(rel) fits agree to within 3 %.

Muon Trigger				
	$P_t(rel)$ Fits		$m(cl)$ Fits	
Sample	$F_{b\bar{b}}$	$F_{c\bar{c}}$	$F_{b\bar{b}}$	$F_{c\bar{c}}$
JC, SV	90.1 ± 0.5 %	9.9 ± 0.4 %	89.0 ± 0.5 %	11.0 ± 0.3 %
JC, DV	98.7 ± 1.3 %	1.3 ± 0.9 %	97.6 ± 1.2 %	2.4 ± 0.7 %
SLT	92.8 ± 1.6 %	7.2 ± 1.1 %	91.5 ± 1.4 %	8.5 ± 0.9 %

Table 3.5: Results of the P_t(rel) and m(cl) fits for the $b\bar{b}$ to $c\bar{c}$ ratio in the muon trigger data for the jet charge single vertex, jet charge double vertex, and soft lepton flavor tag events.

Nominal Values				
	e Trigger		μ Trigger	
Sample	$F_{b\bar{b}}$	$F_{c\bar{c}}$	$F_{b\bar{b}}$	$F_{c\bar{c}}$
JC, SV	90.9 ± 1.3 %	9.1 ± 1.3 %	89.6 ± 1.3 %	10.4 ± 1.3 %
JC, DV	95.6 ± 1.5 %	4.4 ± 1.5 %	98.2 ± 1.3 %	1.8 ± 1.3 %
SLT	92.9 ± 1.7 %	7.1 ± 1.7 %	92.2 ± 1.6 %	7.8 ± 1.6 %

Table 3.6: Nominal values for the $b\bar{b}$ to $c\bar{c}$ ratio in the jet charge single vertex, jet charge double vertex, and soft lepton flavor tagged data for the electron and muon triggers.

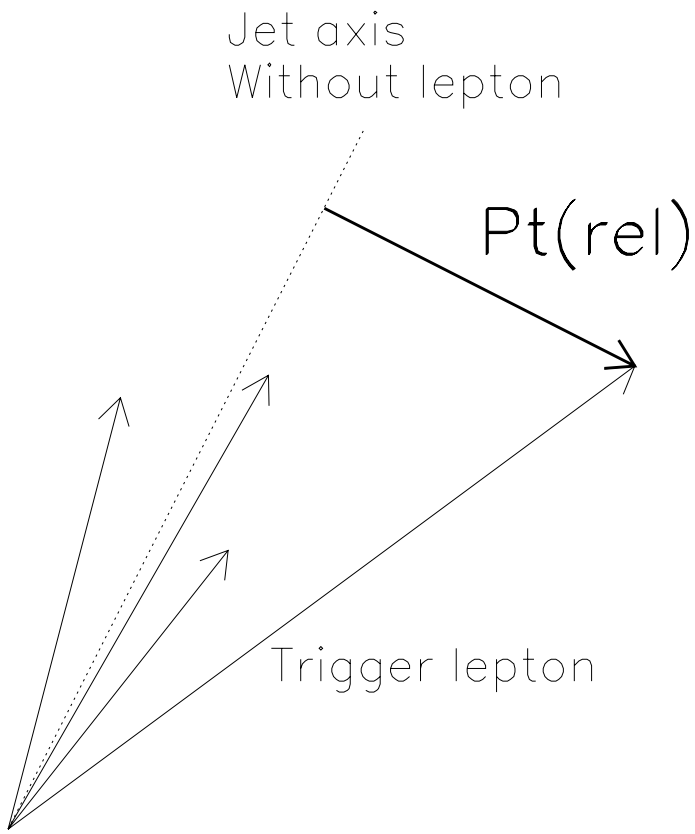

Figure 3.7: The trigger lepton $P_t(rel)$ (thick vector) is defined as the component of the trigger lepton momentum transverse to the jet that it's associated with. The jet axis (dotted line) is calculated without including the trigger lepton.

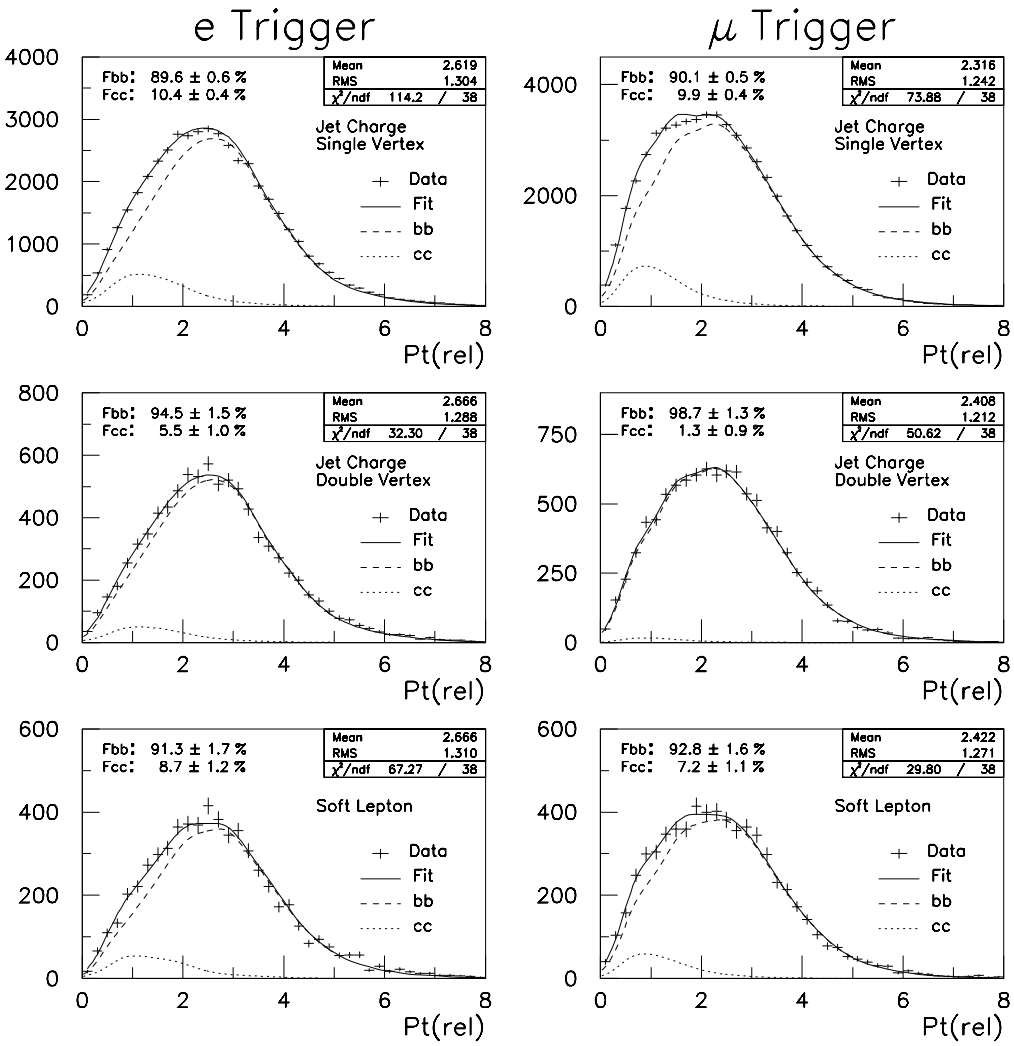

Figure 3.8: Results of the P_t(rel) fits for the $b\bar{b}$ to $c\bar{c}$ ratio. The points with error bars are the data. The solid curve is the result of the fit, which is the sum of the $b\bar{b}$ component (dashed curve) and the $c\bar{c}$ component (dotted curve).

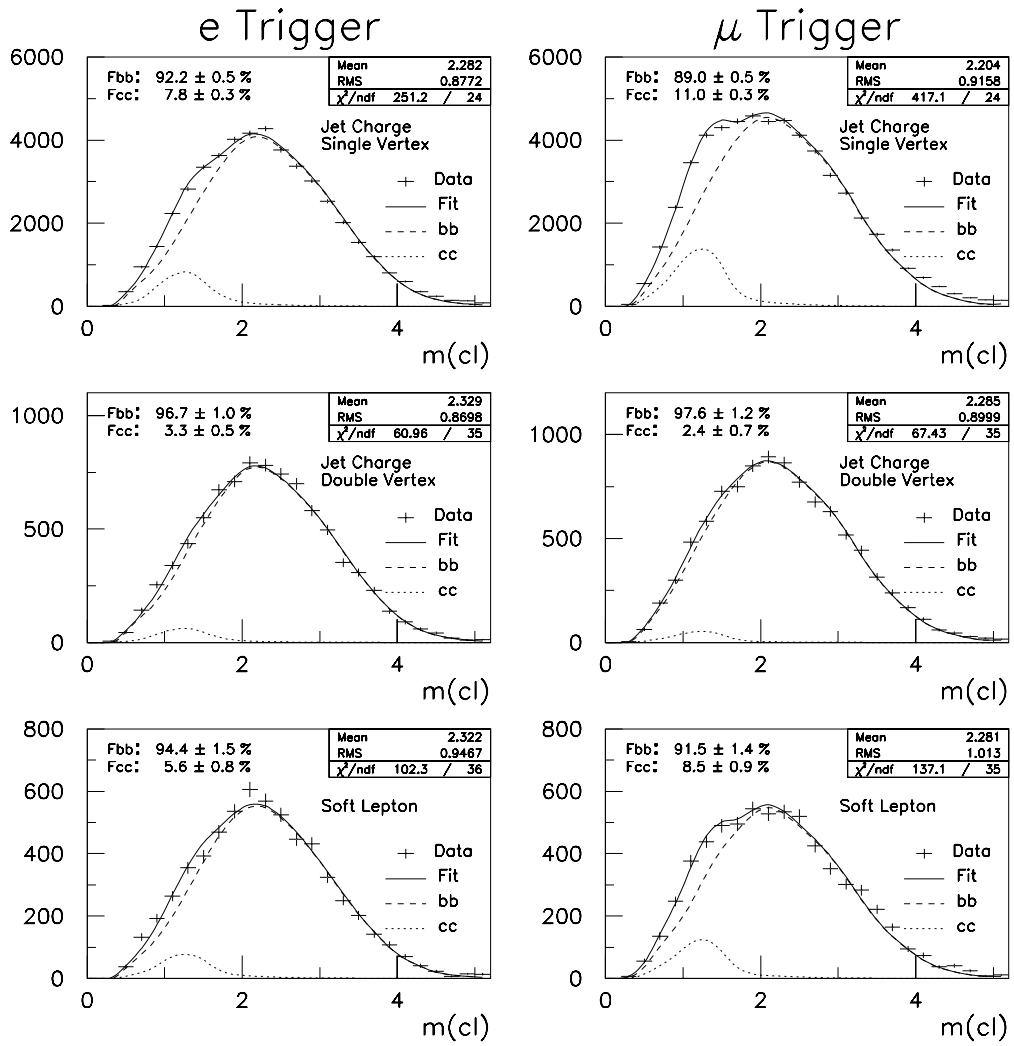

Figure 3.9: Results of the m(cl) fits for the $b\bar{b}$ to $c\bar{c}$ ratio. The points with error bars are the data. The solid curve is the result of the fit, which is the sum of the $b\bar{b}$ component (dashed curve) and the $c\bar{c}$ component (dotted curve).

Chapter 4

Reconstruction of the Proper Time t

As was shown in Chapter 1, the proper time (t) dependence of $B_d^0 - \bar{B}_d^0$ mixing is given by the equations

$$P_m(t) = , \; e^{-\Gamma t} \frac{1}{2} \; (1 - \cos(\Delta m_d \; t)) \tag{4.1}$$

$$P_u(t) = , \; e^{-\Gamma t} \frac{1}{2} \; (1 + \cos(\Delta m_d \; t)) \, . \tag{4.2}$$

where P_m (P_u) is the probability that the B_d^0 decayed in a "mixed" ("unmixed") state and $1/,$ is the lifetime of the B_d^0. A mixed state is where a B_d^0 ($\bar{B}_d^0$) at $t = 0$ decays as a $\bar{B}_d^0$ (B_d^0). In order to measure Δm_d from the proper time dependence described by Equations 4.1 and 4.2, the proper time t must be measured for each event in the data sample.

The proper time at decay of a B hadron is given by

$$t = \frac{1}{c} \cdot \frac{L_{xy} \cdot m_B}{P_t(B)} \tag{4.3}$$

where L_{xy} is the transverse decay length, m_B is the mass of the B hadron ($m_B = 5.28$ GeV/c^2), $P_t(B)$ is the transverse momentum of the B hadron, and c is the speed of

light. This chapter describes how we determine our resolution on L_{xy} and how we estimate $P_t(B)$.

4.1 Resolution on Transverse Decay Length L_{xy}

The transverse decay length L_{xy}, as defined in Chapter 3, is determined from the distance in the x-y plane between the primary and secondary vertices. To determine the experimental resolution on L_{xy}, we examine the quantity $\delta L_{xy} = L_{xy}(\text{meas}) - L_{xy}(\text{true})$ in the Monte Carlo. We only look at Monte Carlo events with $L_{xy}(\text{true}) > 0.1$ cm in order to avoid creating a bias in the δL_{xy} distribution. Events with $L_{xy}(\text{true}) < 0.1$ cm are biased toward high δL_{xy} because in this region events that are smeared to higher L_{xy} are more likely to pass the $|L_{xy}/\sigma_{L_{xy}}|$ requirement.

Figure 4.1 shows the δL_{xy} distributions for the e and μ trigger data. The δL_{xy} distributions are parameterized with the sum of three Gaussians, a positive δL_{xy} exponential, and a negative δL_{xy} exponential. The parameters A_i, σ_i, and m_i are the area, width, and mean for the ith Gaussian. The parameters C_P (C_N) and L_P (L_N) are the area and constant for the positive (negative) δL_{xy} exponential. δL_{xy} has a positive bias from decays where the secondary vertex includes either a mixture of tracks from the B and D decay or only tracks from the D decay. In the fit for Δm_d, we use the parameterizations shown in Figure 4.1 to convolute the probability density of observing an event with proper time t with the L_{xy} resolution. The parameterization

will be referred to as $R_{L_{xy}}\left(L^0_{xy}, L^r_{xy}\right)$ where L^0_{xy} (L^r_{xy}) is the true (reconstructed) transverse decay length.

4.2 Estimating $P_t(B)$

The transverse momentum of the cluster of tracks that form the secondary vertex ($P_t(cl)$) is only a fraction of the transverse momentum of the B meson ($P_t(B)$). This is because we do not observe all of the decay products of the B meson. The neutrino from the semileptonic decay and other neutral decay products always escape detection. Low momentum charged decay products may also not be included in the cluster. We estimate $P_t(B)$ based on distributions of the average fraction of $P_t(B)$ that is observed. This fraction, which is referred to as the K-factor, is defined as

$$K = \frac{P_t(cl)}{P_t(B)} \tag{4.4}$$

where $P_t(cl)$ is the P_t of the cluster of tracks that form the secondary vertex and $P_t(B)$ is the true P_t of the B hadron.

The K-factor depends on both $P_t(cl)$ and $m(cl)$, which is the invariant mass of the cluster of tracks that form the secondary vertex. Qualitatively, the larger $P_t(cl)$ and $m(cl)$, the larger the fraction of $P_t(B)$ observed. The K-factor also depends on whether the trigger lepton is from a direct ($b \to c\ l\ \nu$) or sequential ($b \to c \to s\ l\ \nu$) decay. There are also kinematic differences between the e and μ triggers which affect the K-factor. The data are divided into four $P_t(cl)$ and four $m(cl)$ bins. For each bin

we form separate K-factor distributions for the following combinations:

- Electron trigger, direct decay.
- Electron trigger, sequential decay.
- Muon trigger, direct decay.
- Muon trigger, sequential decay.

Figure 4.2 shows the K-factor distributions for the highest and lowest $P_t(cl)$, $m(cl)$ bins in the e trigger $b\bar{b}$ Monte Carlo for direct and sequential decays. Events in the highest $P_t(cl)$, $m(cl)$ bin clearly have a larger fraction of $P_t(B)$. The $P_t(cl)/P_t(B)$ is also narrower in the highest $P_t(cl)$, $m(cl)$ bin, which translates into a more precise estimation of $P_t(B)$.

A single estimate of $P_t(B)$ for each event can be made by dividing $P_t(cl)$ by the mean value of the appropriate K-factor distribution. That is,

$$P_t' = \frac{P_t(cl)}{\langle P_t(cl)/P_t(B)\rangle_{ij}} \tag{4.5}$$

where P_t' is the corrected P_t and ij denotes the ith and j^{th} $P_t(cl)$ and $m(cl)$ bins. The P_t' estimate can be used to get an estimate of ct for the event, which is given by

$$ct_r = \frac{L_{xy} \cdot m_B}{P_t'}. \tag{4.6}$$

Figures 4.3, 4.4, and 4.5 show the ct_r distributions for the soft lepton, jet charge single vertex, and jet charge double vertex flavor tagged data respectively. The solid

distribution is the data. The dashed distribution is a combination of $b\bar{b}$ and $c\bar{c}$ data with the relative fraction from Table 3.6. The data agree fairly well with the Monte Carlo, except for $ct_r < 0$ where there is an excess in the data.

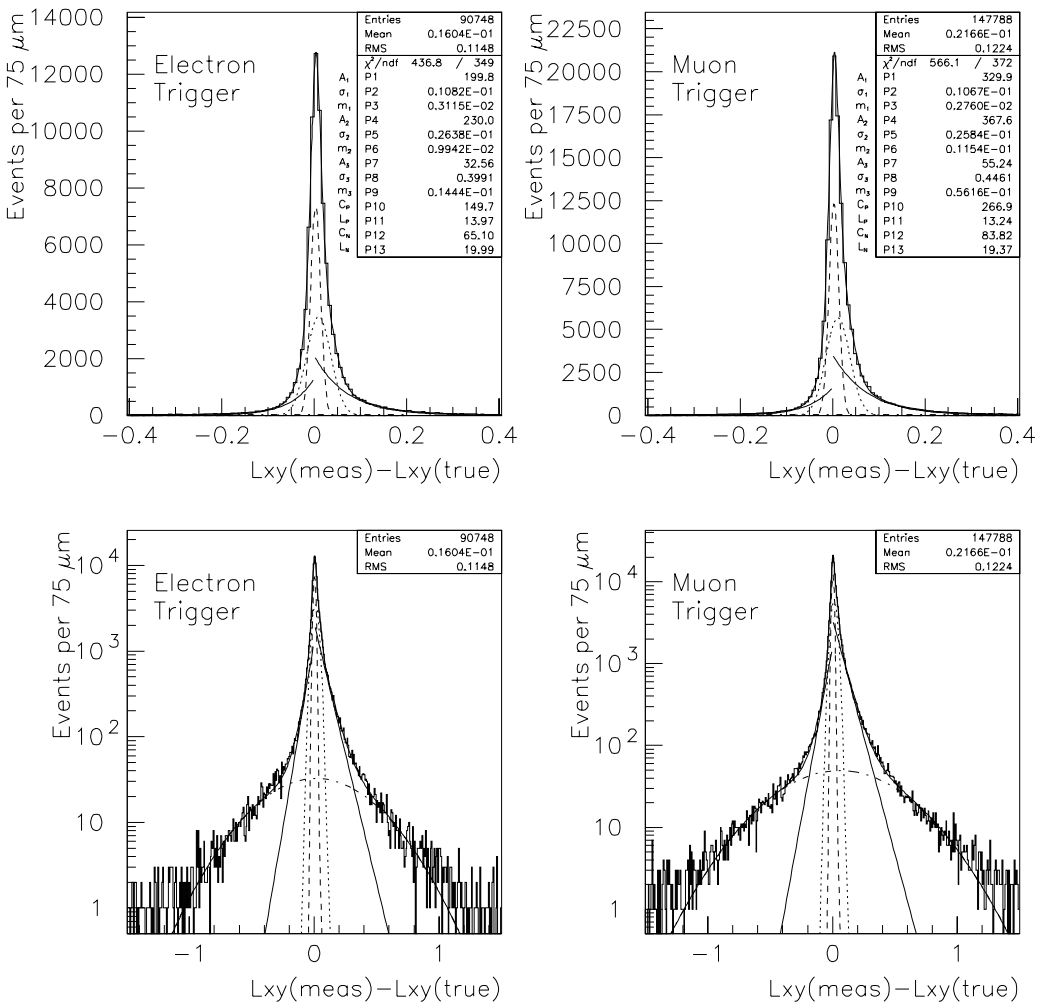

Figure 4.1: The distributions of difference between the reconstructed (L_{xy}(meas)) and true (L_{xy}(true)) transverse decay length as predicted by the Monte Carlo. The three Gaussians and two exponentials used to parameterize the distributions are shown.

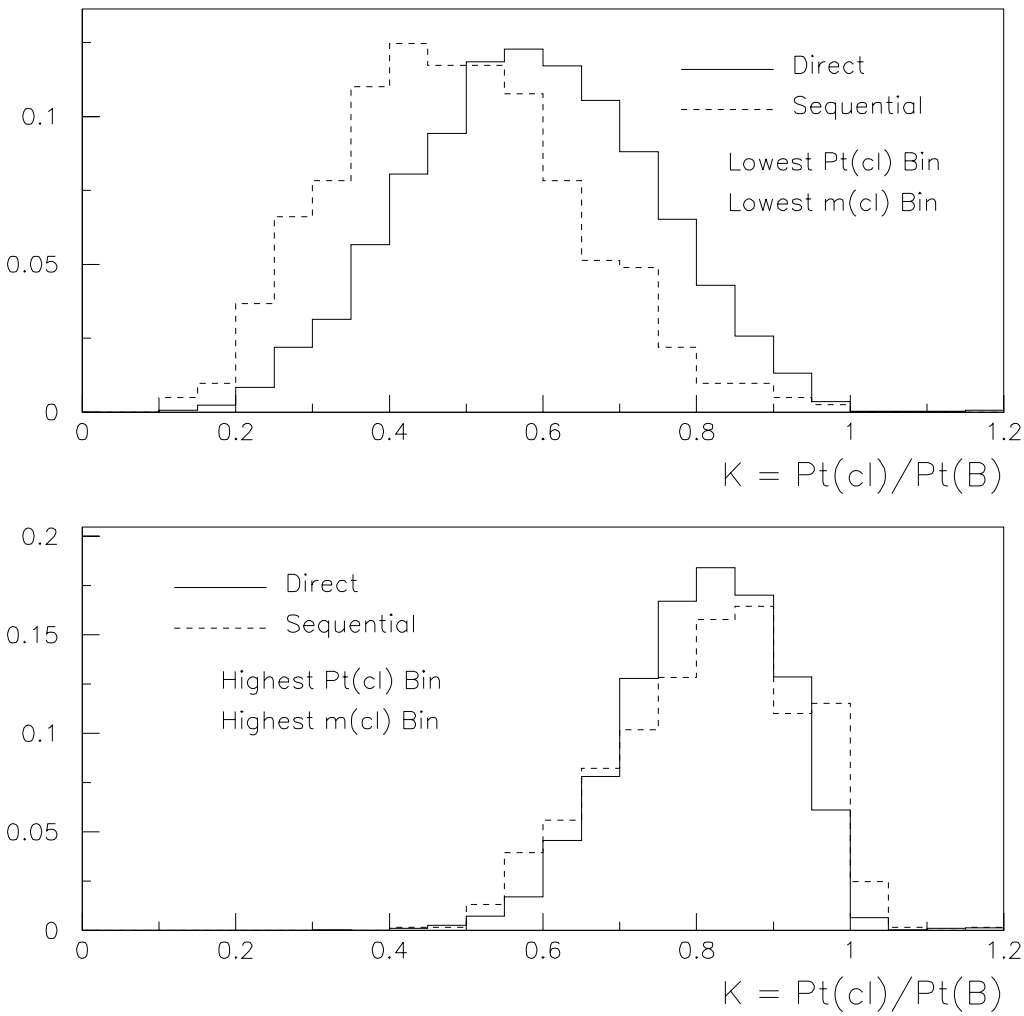

Figure 4.2: Examples of K-factor distributions from the e trigger Monte Carlo. Direct refers to direct semileptonic decay ($b \to l\nu$). Sequential refers to sequential semileptonic decay ($b \to c \to l\nu$).

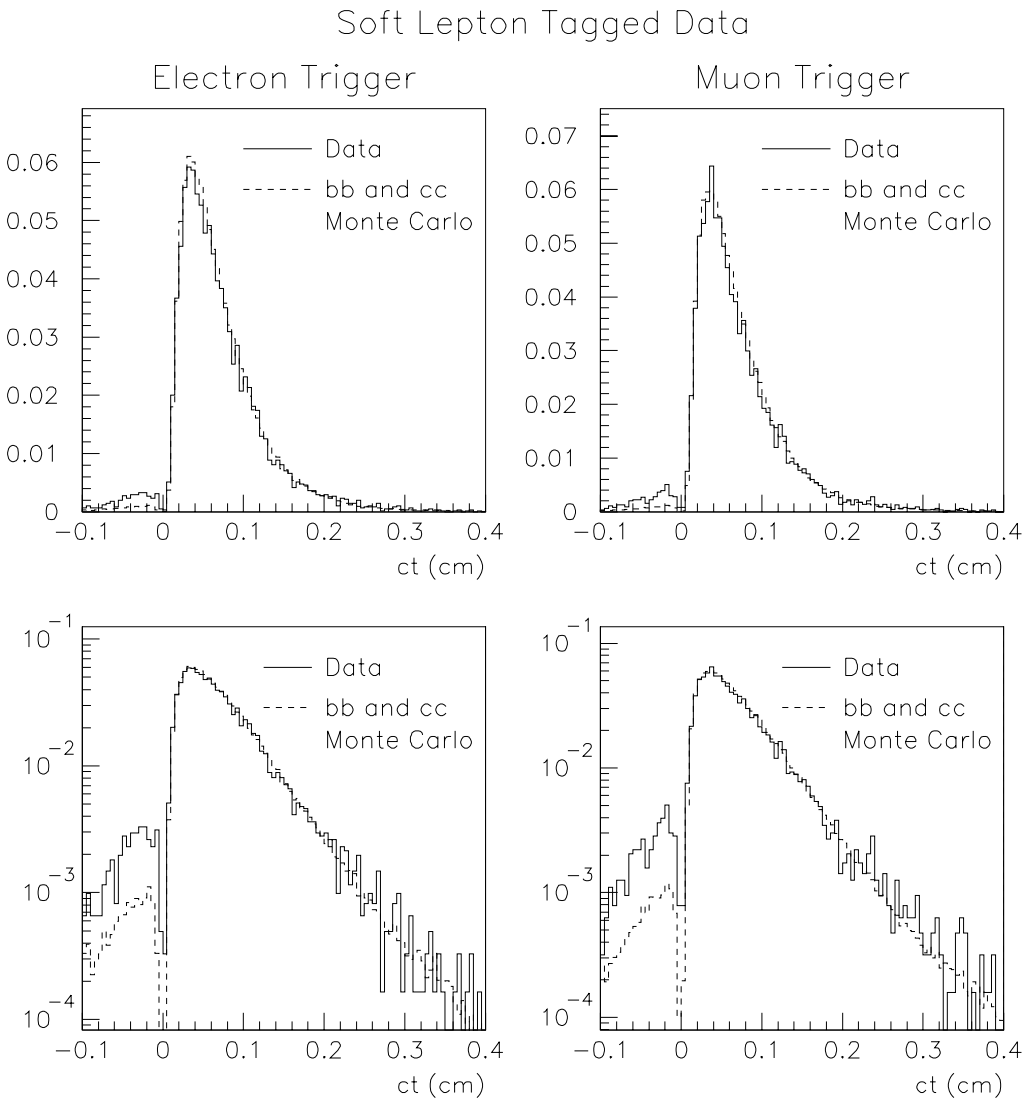

Figure 4.3: Reconstructed ct for the soft lepton tagged data (solid) and a combination of $b\bar{b}$ and $c\bar{c}$ Monte Carlo (dashed). The ratio of $b\bar{b}$ to $c\bar{c}$ Monte Carlo is from Table 3.6. The solid and dashed distributions are both normalized to unit area.

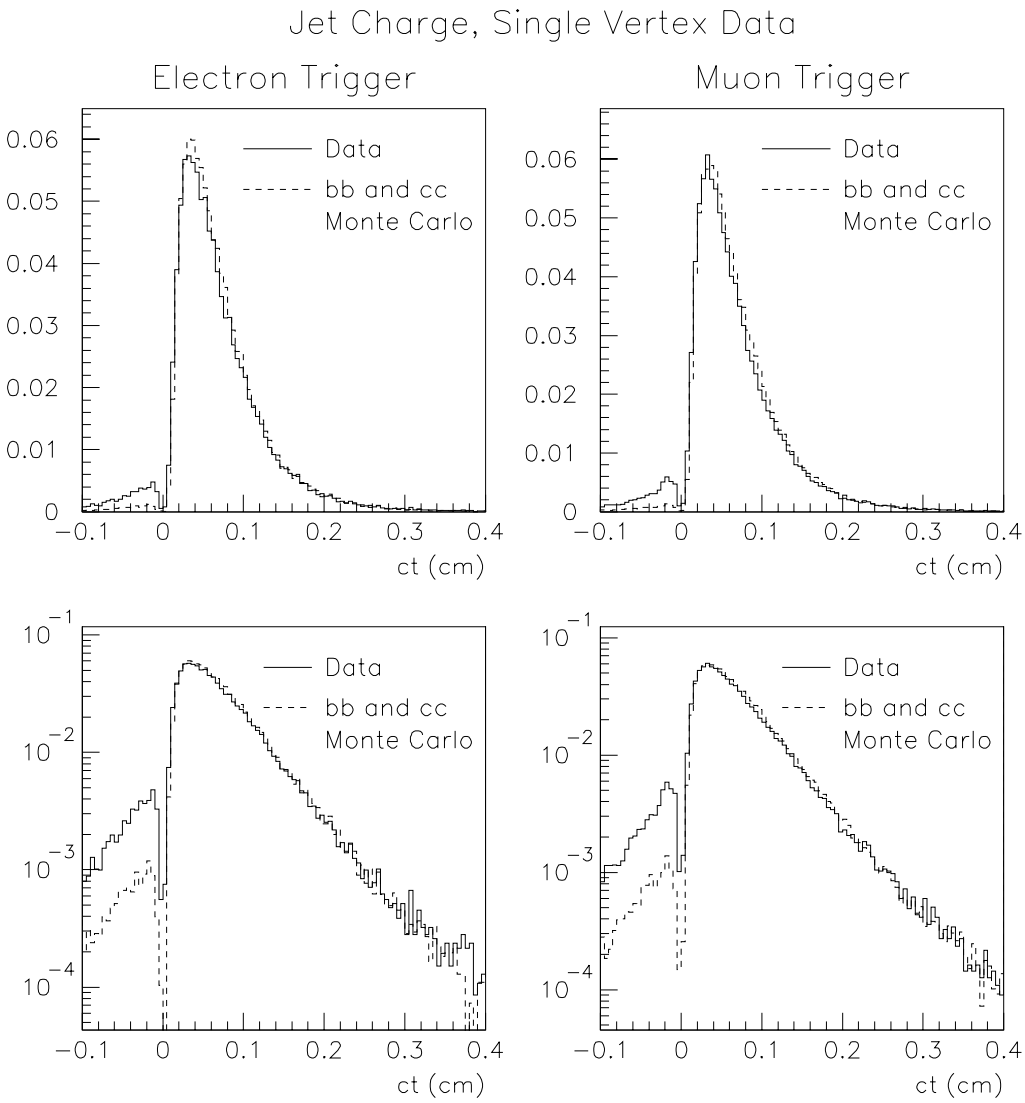

Figure 4.4: Reconstructed ct for the jet charge single vertex data (solid) and a combination of $b\bar{b}$ and $c\bar{c}$ Monte Carlo (dashed). The ratio of $b\bar{b}$ to $c\bar{c}$ Monte Carlo is from Table 3.6. The solid and dashed distributions are both normalized to unit area.

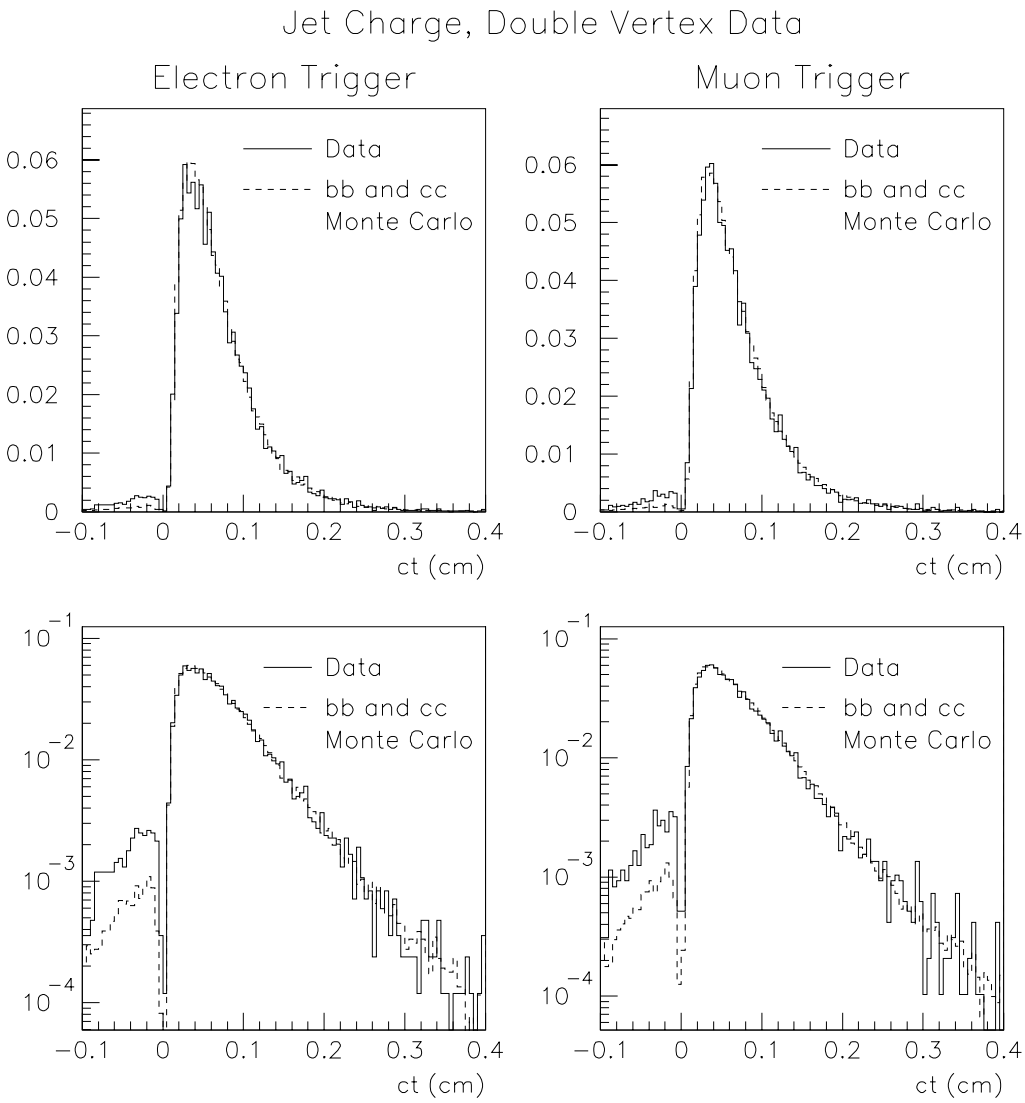

Figure 4.5: Reconstructed ct for the jet charge double vertex data (solid) and a combination of $b\bar{b}$ and $c\bar{c}$ Monte Carlo (dashed). The ratio of $b\bar{b}$ to $c\bar{c}$ Monte Carlo is from Table 3.6. The solid and dashed distributions are both normalized to unit area.

Chapter 5

Flavor Tagging

5.1 Introduction

In order to make a proper time dependent B^0 mixing measurement or a CP asymmetry measurement, one needs to know the flavor of the B at the time of production. Tagging the flavor of the B means determining if it was a B, which contains a $\bar{b}$ quark, or a $\bar{B}$, which contains a b quark. The flavor at production is usually inferred by flavor tagging the "other" B in the event. Since b quarks are always produced in $b\bar{b}$ pairs, the flavor of the B of interest at the time of production can be assumed to be the opposite flavor of the other B. This is not always true, since there is a small but finite probability that the other B was a B^0 and that it decayed in the state opposite of it's original flavor.

Two methods were employed for tagging the flavor at the time of production: soft lepton tagging (SLT) and jet charge tagging. Both rely on the other B in the event to infer the original flavor of the B that produced the trigger lepton. Before describing

these two taggers, we describe how the effectiveness of a flavor tagging method is quantitatively evaluated.

5.1.1 The Flavor Tag Dilution

The quantity that describes how often a flavor tagging method is correct is the dilution (D). The dilution is simply the tag rate minus the mistag rate, as shown below

$$D = \frac{N_{tag} - N_{mistag}}{N_{tag} + N_{mistag}} \tag{5.1}$$

where N_{tag} (N_{mistag}) is the number of events tagged correctly (incorrectly). The term dilution is somewhat of a misnomer since a high dilution is good. A flavor tagger with dilution of 1 is perfect. One with a dilution of 0 gives a random answer (half the time it's right, half the time it's wrong).

The dilution is simply related to the probability that the tag is correct by the formulas below

$$P_{tag} = \frac{1}{2}(1 + D) \tag{5.2}$$

$$P_{mistag} = \frac{1}{2}(1 - D) \tag{5.3}$$

where P_{tag} (P_{mistag}) is the probability that the flavor tag is correct (incorrect). The reason the dilution is used and not P_{tag} becomes clear when one examines the statistical power of the flavor tag.

Consider an asymmetry measurement, which uses a flavor tagger with efficiency ϵ and dilution D, to make a binary assignment: the event is either type a or type b.

The measured asymmetry is defined as

$$A_{meas} = \frac{N_a - N_b}{N_a + N_b} \tag{5.4}$$

where N_a (N_b) is the number of events tagged type a (b). We want to know the true asymmetry in the data, which is given by

$$A = \frac{N_a^0 - N_b^0}{N_a^0 + N_b^0} \tag{5.5}$$

where N_a^0 (N_b^0) is the true number of type a (b) events in the sample. The efficiency of the flavor tag is given by

$$\epsilon = \frac{N_a + N_b}{N_a^0 + N_b^0} \tag{5.6}$$

which is the number of flavor tagged events over the initial number of events before flavor tagging. The true asymmetry from the measured asymmetry is given by

$$A = \frac{1}{D} A_{meas} \tag{5.7}$$

with a statistical uncertainty of

$$\sigma_A = \sqrt{\frac{1 - D^2 A}{\epsilon D^2 N}} \tag{5.8}$$

where N is the number of events in the sample before tagging ($N_a^0 + N_b^0$). The uncertainty scales like $1/\sqrt{\epsilon D^2 N}$, rather than the more familiar $1/\sqrt{N}$. This means the statistical power of the tag is quantified by ϵD^2. If one knows the efficiency and dilution for a flavor tag, one can quantitatively estimate it's usefulness in a measurement. In developing a flavor tag, the quantity ϵD^2 is optimized.

As will be shown, the jet charge tagging method quite efficient, but has a modest dilution. The soft lepton tag is relatively inefficient, but has a very good dilution.

5.1.2 The Raw Dilution

The raw dilution (D_{raw}) is like the true dilution except that it *assumes* opposite sign events are tags and all same sign events are mistags. By opposite (same) sign, we mean that the trigger lepton charge and the flavor tag indicate opposite flavors (the same flavor) for the two Bs in the event.

$$D_{raw} = \frac{N_{OS} - N_{SS}}{N_{SO} + N_{SS}} \tag{5.9}$$

The assumption that opposite sign events are correct tags is not always true because the trigger lepton may be from a B^0 that mixed or a sequential B decay for which opposite sign events are mistags. The trigger lepton may also be fake or the event may be from $c\bar{c}$ production. Taking the above into account, the true and raw dilution are related by

$$D_{raw} = D \cdot \left\{ f_{b\bar{b}} \cdot (1 - 2 \cdot \bar{\chi_B}(\text{eff}))\,(1 - 2 \cdot f_{seq}(ws)) + f_{c\bar{c}} \cdot \frac{D_{c\bar{c}}}{D_{b\bar{b}}} + f_{fake} \cdot \frac{D_{fake}}{D_{b\bar{b}}} \right\} \tag{5.10}$$

or

$$D = N_D \cdot D_{raw} \tag{5.11}$$

where the parameters are

- The sample composition: $f_{b\bar{b}}$, $f_{c\bar{c}}$, f_{fake}.
- The fraction of wrong-sign sequential decays: $f_{seq}(ws)$.
- The effective mixing probability: $\bar{\chi_B}$(eff).
- The $c\bar{c}$ dilution *relative* to the $b\bar{b}$ dilution: $D_{c\bar{c}}/D_{b\bar{b}}$.
- The fake lepton dilution *relative* to the $b\bar{b}$ dilution: $D_{fake}/D_{b\bar{b}}$.

Note that $D_{raw} < D$ and $N_D > 1$. In the determination of Δm_d, the dilution normalization N_D is a free parameter for each flavor tagging method. We choose to fit for N_D, rather than calculating it with Equation 5.10, to avoid biasing Δm_d, since Δm_d and N_D are correlated.

Chapter 6

Jet Charge Flavor Tagging

Jet charge flavor tagging was developed in the e^+–e^- collider environment [18] [19] [20] [21] [22]. The jet charge, defined below in Equation 6.1, is simply a momentum-weighted charge average of tracks in a jet.

$$Q_{jet} = \frac{\sum_i^n q_i \cdot (\vec{\mathbf{p}}_\mathbf{i} \cdot \hat{\mathbf{a}})^\kappa}{\sum_i^n (\vec{\mathbf{p}}_\mathbf{i} \cdot \hat{\mathbf{a}})^\kappa} \tag{6.1}$$

The sum is over all n tracks associated with the jet. The tracks used must satisfy the quality criteria listed in Table 3.1 introduced in Chapter 3. The component of the track momentum $\vec{\mathbf{p}}_\mathbf{i}$ along the jet axis $\hat{\mathbf{a}}$ is the weight for the charge of the track q_i. A weighting factor κ tunes the sensitivity to different parts of the momentum spectrum. A low (high) κ emphasizes the low (high) momentum tracks. A $\kappa = 0$ gives all tracks equal weight. The upper extreme $\kappa = \infty$ gives all of the weight to the highest momentum track. The jet charge is normalized to be bound within the interval $[-1, 1]$. In this analysis, a κ of 1 is used.

The jets are defined using the track clustering algorithm described in subsec-

tion 3.3.2. Tracks are associated to the jet simply by requiring the separation between the track and the jet axis in R to be less than 0.7. That is, the tracks must be in a cone of $\Delta R < 0.7$ about the jet axis.

The jet charge of a heavy flavor quark jet is correlated to the charge of the heavy quark. This is an empirical fact. There are several intuitive explanations for why it works. If the heavy quark decays semileptonically, one could argue that the lepton will contribute strongly to the charge average. Since the lepton charge has the correct sign, the jet charge will have the correct sign. If a B^+ decays via $D^0 \to K^+$ the kaon and the products from the virtual W^+ in the $b \to c$ transition have the right sign. The kaon in the similar decay of a B_d^0 is neutral but the B_d^0 produces a π^+ in fragmentation which has the right sign [1]. The fragmentation pion is illustrated in Figure 6.1.

In the following sections we will describe how we select the other b jet, the jet charge distributions, the jet charge dilution, and the statistical power of jet charge tagging.

6.1 $b\bar{b}$ Production Topologies

In the $e^+e^- \to Z^0$, $Z^0 \to b\bar{b}$ environment, such as LEP or SLC, it's trivial to identify the jet from the other b in the event. The Z^0, produced essentially at rest in the lab frame, decays into two back-to-back jets, each with $|\vec{\mathbf{p}}| = m_{Z^0}/2$. Because of the

[1] Another B^0 mixing analysis at CDF uses the fragmentation $\pi^\pm$ as the production flavor tag [46]. This is referred to as "same side tagging" since the other B is not used for the production flavor tag.

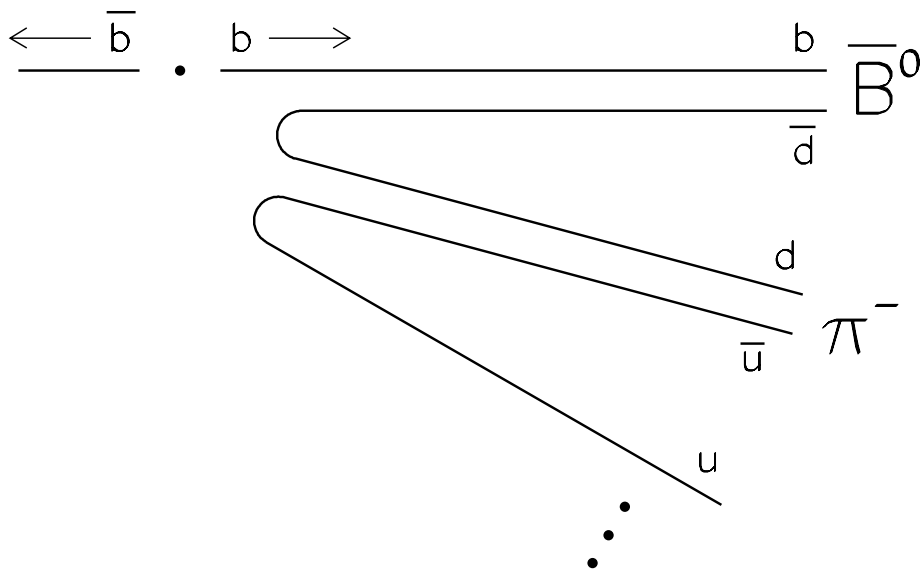

Figure 6.1: The π^- produced in b quark fragmentation, where a $\bar{B}_d^0$ is formed, is correlated in charge with the original b quark flavor.

symmetry of the detectors used, if one b jet is in the detector acceptance, the other will be too.

The p–$\bar{p}$ collider environment is very different. The main $b\bar{b}$ production mechanism at $\sqrt{s} = 1.8$ TeV is **gluon-gluon fusion**, or direct production [2]. Direct $b\bar{b}$ production gives b jets that are back-to-back in ϕ and balanced in P_t. However, the $b\bar{b}$ system may be significantly boosted in the $\pm z$ direction, since the $b\bar{b}$ pair is produced from gluons within the p and $\bar{p}$ which carry a variable fraction of the p or $\bar{p}$ momentum. This means the b and $\bar{b}$ jets are not necessarily back-to-back in η.

[2]Gluon-gluon fusion dominates over quark annihilation, which is the same order in α_s, because the parton density function for the gluon is much higher than that of the quark at low x, where the $b\bar{b}$ cross section is large.

Two other higher order $b\bar{b}$ production mechanisms give event topologies that are much harder to deal with. The so called **flavor excitation** process, for events that pass our triggers, gives one b jet in the central (low η) region. The other b in the event usually has a large longitudinal boost making it out of the tracking chamber acceptance. That is, the tracks from the b jet all have large values $|\eta|$ which means they exit the tracking chamber before traversing all of the sense wires. The second higher order process is **gluon splitting** which gives two b jets that are relatively close to each other in η and ϕ. The b jets are balanced by a gluon jet on the opposite side in ϕ. The contribution to the total $b\bar{b}$ cross section from higher order production mechanisms is comparable to that of direct production. Figure 6.2 shows representative Feynman diagrams for the three mechanisms. Note that not all of the possible diagrams are shown.

In practice, one can't distinguish between the different production mechanisms. This means some of the time, the jet selected as the other b in the event is really from a gluon. There are two ways of dealing with this problem. First, if the event has two jets with secondary vertex tags, where the trigger lepton jet is one of the tagged jets, we use the other tagged jet to calculate the jet charge. If only the trigger lepton jet is secondary vertex tagged, the highest P_t jet opposite the trigger lepton in ϕ is selected as the other B jet. The next subsections give the details of the opposite side jet selection and classification.

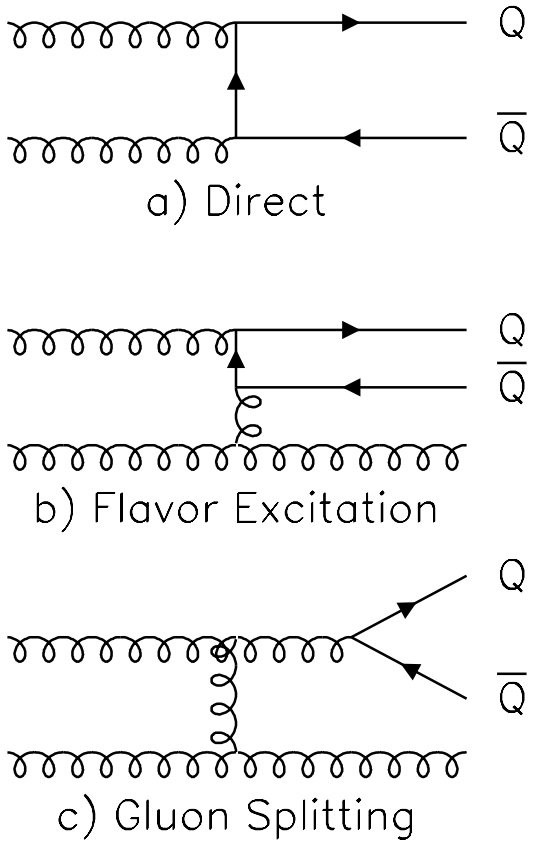

Figure 6.2: Representative Feynman diagrams for the three main $b\bar{b}$ production mechanisms. Note that not all possible diagrams are shown.

6.2 Jet Selection and Classification

6.2.1 Double Secondary Vertex Tagged Events

If an event has a second secondary vertex tagged jet, in addition to the trigger lepton jet, the second vertex tagged jet is used to calculate the jet charge. These events are classified as double vertex events. We require that the second tag have a positive decay length (L_{xy}) and that it be separated in ϕ from the trigger jet by 0.5 radians. If the second vertex tag fails either of these requirements, the event is treated as a single vertex tagged event. About 7% of the events are classified as double vertex events.

6.2.2 Single Secondary Vertex Tagged Events

If only the trigger lepton jet has a good secondary vertex tag, the task of identifying the second b jet is more difficult. The choice is based on the jet topology alone (ϕ and P_t). The only option is to assume the event is from direct $b\bar{b}$ production, giving back-to-back b jets in ϕ. Under this assumption, we require that the other b candidate jet be separated in ϕ by at least $\pi/2$ from the trigger b jet and that the jet have a minimum transverse momentum ($P_t > 5.0$ GeV/c). If there is more than one jet satisfying these criteria, the jet with the highest P_t is chosen.

The efficiency for finding such a jet is about 42%. The $b\bar{b}$ Monte Carlo tells us that the jet selected is indeed from the other b in the event around 75% of the time. The $b\bar{b}$

Monte Carlo also predicts that the other b jet is in the tracking chamber acceptance ($|\eta| < 1$) only about 40% of the time.

6.3 Jet Charge Distributions and Dilutions

The tag dilution D is a function of the jet charge itself. Figures 6.3 and 6.4 show jet charge distributions and the raw dilution derived from them as a function of $|Q_{jet}|$ for the electron and muon trigger data respectively. The raw dilution for each bin is calculated using only events with $|Q_{jet}|$ in that particular bin. The $|Q_{jet}|$ dependence is roughly linear, with the exception of events where $|Q_{jet}| = 1$, so we fit the $D(raw)$ vs $|Q_{jet}|$ distribution to the functional form:

$$D(raw) = |Q_{jet}| \cdot D_{max}(raw) \tag{6.2}$$

excluding events where $|Q_{jet}| = 1$. This parameterization is used to predict the tag dilution on an event-by-event basis based on it's absolute jet charge, and thus the probability that the event is a tag or a mistag. For events with $|Q_{jet}| = 1$ the raw dilution is used, instead of Equation 6.2, for the dilution prediction. The $b\bar{b}$ Monte Carlo predicts this behavior.

Note that the double vertex events have a significantly higher raw dilution than the single vertex events. This is because the secondary vertex in associated with the jet significantly increases the probability that the jet is indeed from the other B in the event. Events where the jet charge is calculated from a gluon jet, instead of the

other B, have zero dilution on average.

The $D(raw)$ vs $|Q_{jet}|$, population of events in $|Q_{jet}|$, and overall tag efficiency can be combined to give $\epsilon D^2(raw)$ vs $|Q_{jet}|$. These distributions are shown in Figures 6.5 and 6.6 for the electron and muon trigger data respectively. It can be shown [47] that if several measurements with different dilutions are made of a particular quantity, the equivalent ϵD^2 for the combination of all measurements is $\sum_i \epsilon_i D_i^2$. In Figures 6.5 and 6.6 the data are binned in $|Q_{jet}|$. The $\epsilon D^2(raw)$ values are summed over the $|Q_{jet}|$ bins to get an effective $\epsilon D^2(raw)$ for the entire sample. The results of this calculation are in Table 6.1. These values for $\epsilon D^2(raw)$ need to be multiplied by N_D^2 from the fit to Δm_d to get the true flavor tag ϵD^2. The true ϵD^2 is quantity that quantifies the statistical power of the flavor tagging method (see Equation 5.8).

	e Trigger		μ Trigger	
Tag Type	Total ϵ	$\sum_i \epsilon_i D_{raw}^2$	Total ϵ	$\sum_i \epsilon_i D_{raw}^2$
Single Vertex	41.55 ± 0.14 %	0.077 ± 0.016 %	43.81 ± 0.14 %	0.048 ± 0.012 %
Double Vertex	7.44 ± 0.08 %	0.159 ± 0.023 %	7.66 ± 0.07 %	0.113 ± 0.018 %
Combined	48.99 ± 0.16 %	0.236 ± 0.028 %	51.47 ± 0.16 %	0.161 ± 0.022 %

Table 6.1: Jet charge flavor tag $\sum \epsilon D(raw)^2$ where the sum is in bins of $|Q_{jet}|$.

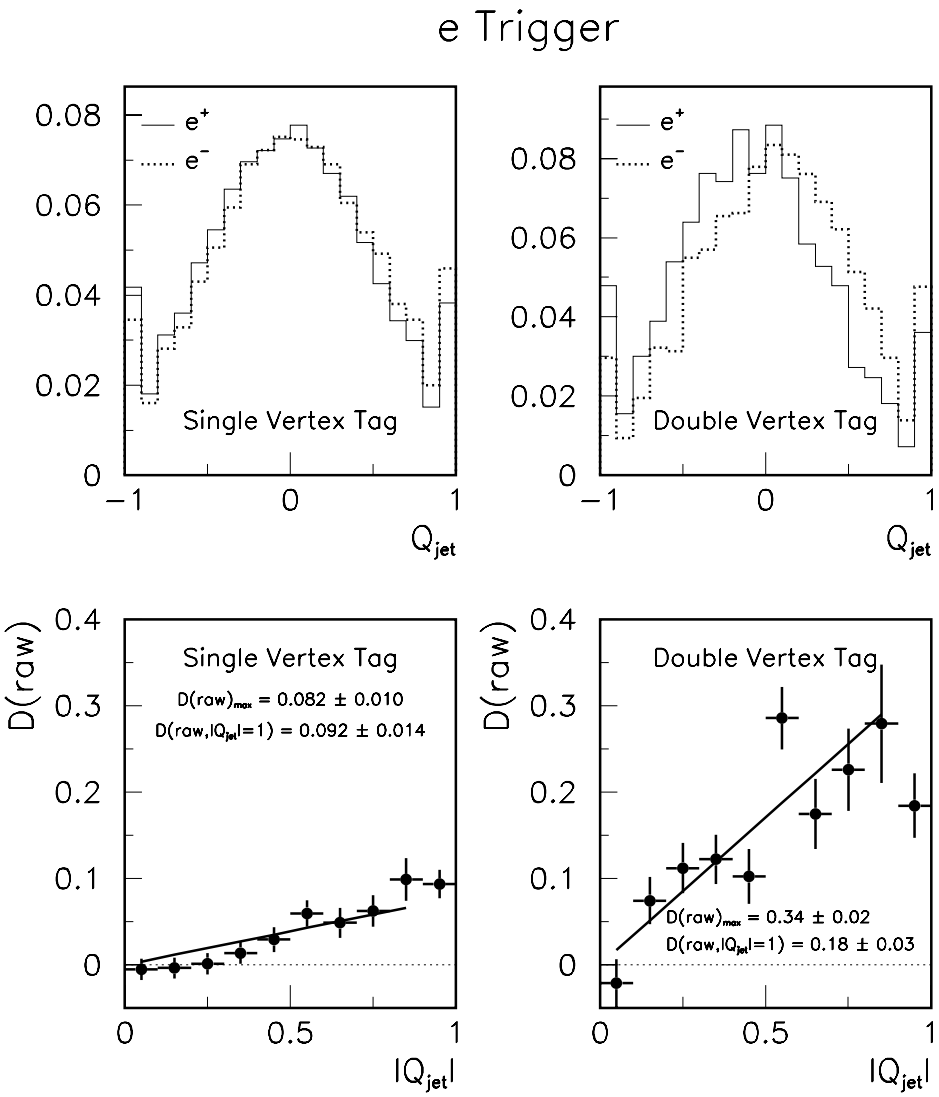

Figure 6.3: Jet charge and $D(raw)$ vs $|Q_{jet}|$ distributions for single and double vertex tagged events in the e trigger data.

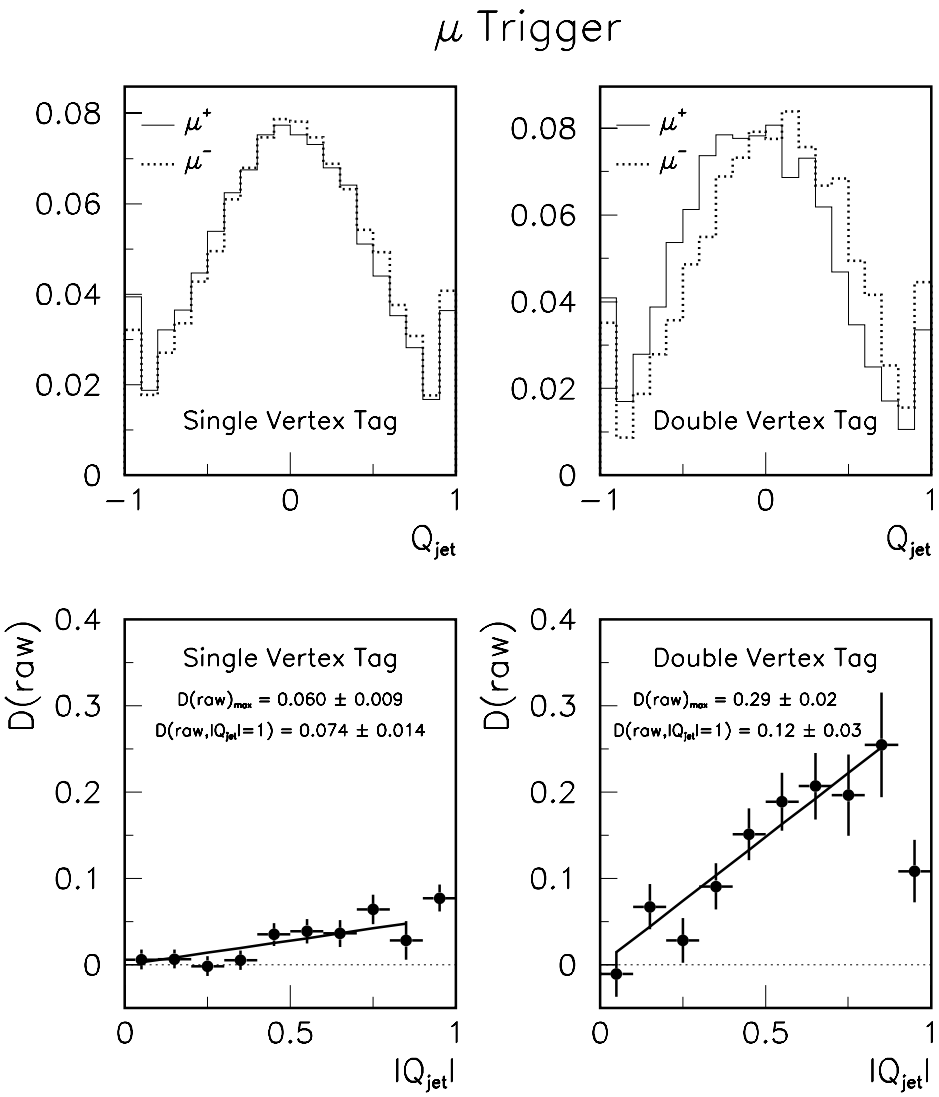

Figure 6.4: Jet charge and $D(raw)$ vs $|Q_{jet}|$ distributions for single and double vertex tagged events in the μ trigger data.

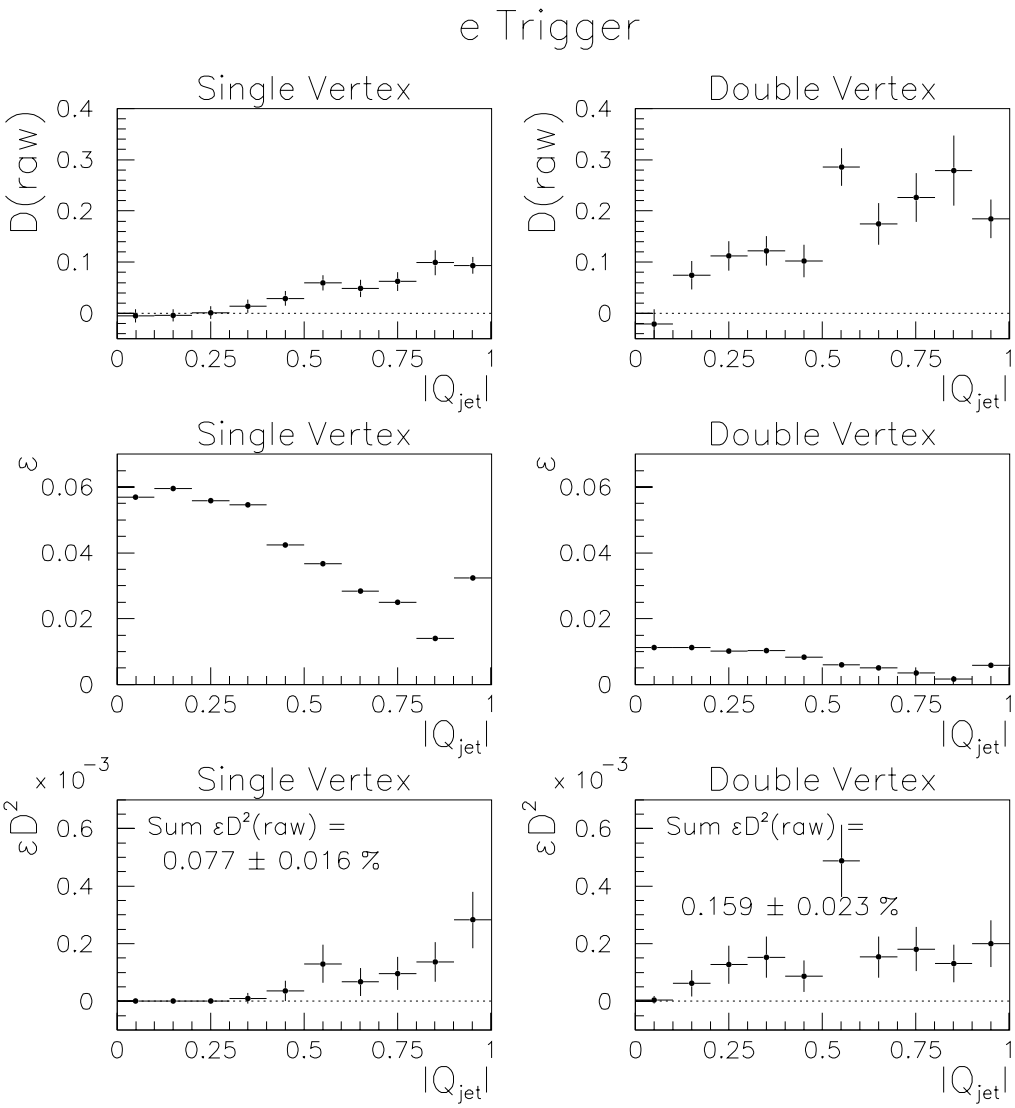

Figure 6.5: The raw dilution $D(raw)$, flavor tag efficiency ϵ, and $\epsilon D(raw)^2$ in bins of $|Q_{jet}|$ for single and double vertex e trigger events.

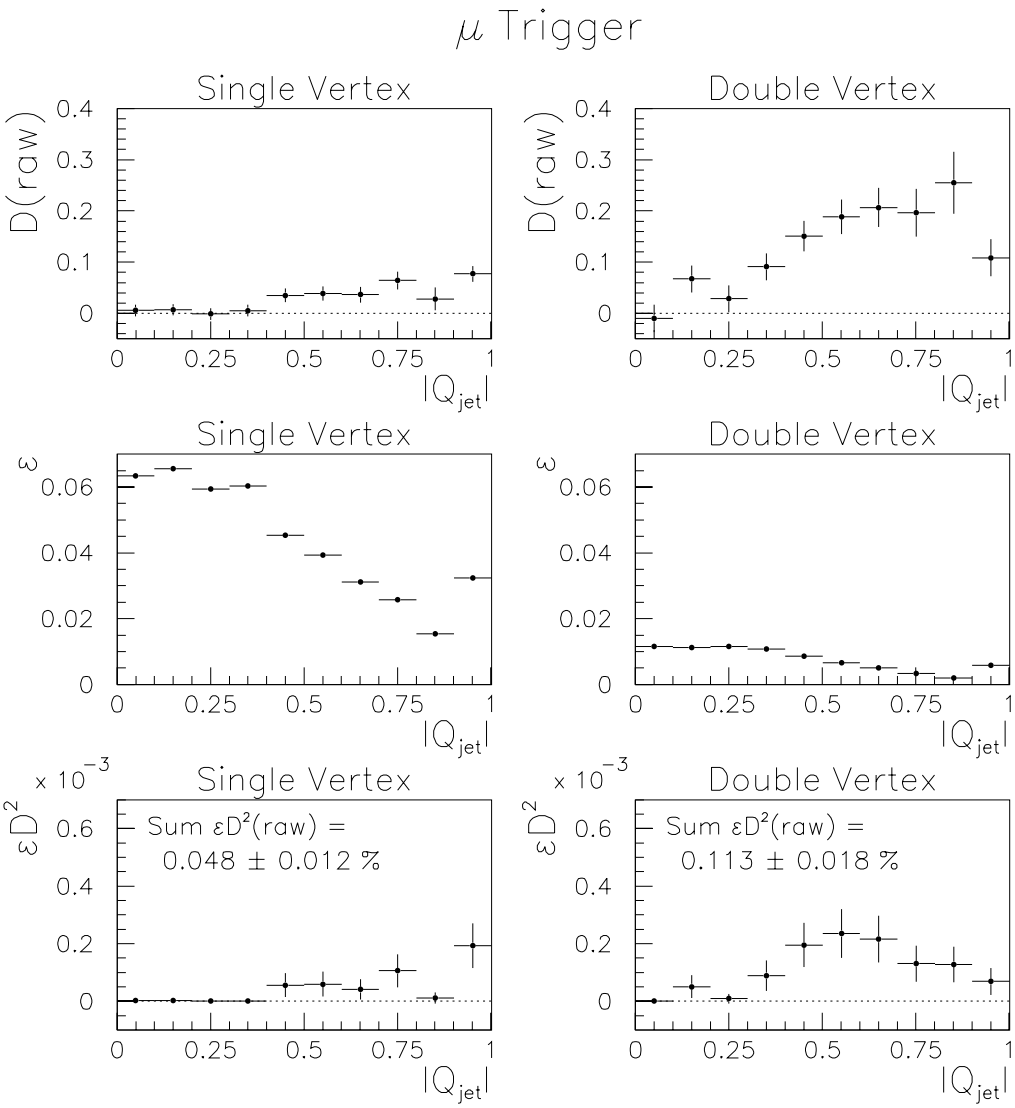

Figure 6.6: The raw dilution $D(raw)$, flavor tag efficiency ϵ, and $\epsilon D(raw)^2$ in bins of $|Q_{jet}|$ for single and double vertex μ trigger events.

Chapter 7

Soft Lepton Flavor Tagging

Semileptonic b decays can be used to tag the flavor of the second b, just as it is used to tag the first. CDF has already developed low-P_t electron and muon b taggers for use in its top discovery [45] [48]. The same algorithms are used here with only minor changes to reflect the different kinematics of our events relative to the much more energetic top events.

The soft lepton and the trigger lepton must form an invariant mass which is greater than 5 GeV/c and must not be in the same jet as the trigger lepton, which is equivalent to requiring a separation $\Delta R > 0.7$. This ensures that the soft leptons are not from double semileptonic decay: $b \to l\nu c$; $c \to l\nu s$. Soft electrons consistent with coming from conversions are removed using the same criteria described in Subsection 3.5.

The quantity that discriminates soft leptons from direct b decay from those from sequential decay and charm and fake backgrounds is P_t(rel), as those background processes have a much smaller mean P_t(rel) than does direct decay. Recall that

P_t(rel) is the component of the lepton momentum transverse to the axis of the jet that it's associated with, where the lepton is not included in the calculation of the jet axis. This means that the raw SLT dilution is a function of P_t(rel) much in the same way that the jet charge raw dilution is a function of $|Q_{jet}|$. The SLT raw dilution is parameterized as a function of P_t(rel) used to predict P^{tag} on an event-by-event basis. Figure 7.1 shows the soft lepton raw dilution as a function of P_t(rel) for the e and μ trigger data. The D_{raw} parameterization has the form

$$D_{raw}(P_t(\text{rel})) = A \cdot \left(1 - e^{-P_t(\text{rel})+B}\right) \tag{7.1}$$

where the parameters A and B are determined for each of the soft lepton types: soft electron and the four soft muon types. If the event does not have a soft lepton P_t(rel) measurement, because the soft lepton is isolated, the average D_{raw} for events with no P_t(rel) is used. These events are shown in Figure 7.1 as the negative P_t(rel) bin. The dashed curves are the variations on $D_{raw}(P_t(\text{rel}))$ used in the evaluation of the systematic errors on Δm_d and N_D. For the events with no soft lepton $P_t(rel)$, the statistical error on the raw dilution of the no $P_t(rel)$ events is used for the variation in the systematic errors.

The statistical power of the soft lepton flavor tag is estimated from $\sum_i \epsilon_i D_{raw}^2$ where the sum is in bins of soft lepton P_t(rel). The values of $\sum_i \epsilon_i D_{raw}^2$ are summarized in Table 7.1.

	e Trigger		μ Trigger	
SLT Type	Total ϵ	$\sum_i \epsilon_i D^2_{raw}$	Total ϵ	$\sum_i \epsilon_i D^2_{raw}$
Soft e	1.59 ± 0.04 %	0.136 ± 0.021 %	1.56 ± 0.03 %	0.074 ± 0.015 %
Soft μ, CMU	1.71 ± 0.04 %	0.069 ± 0.015 %	1.62 ± 0.04 %	0.041 ± 0.011 %
Soft μ, CMP	0.20 ± 0.01 %	0.028 ± 0.009 %	0.22 ± 0.01 %	0.009 ± 0.005 %
Soft μ, CMUP	1.08 ± 0.03 %	0.125 ± 0.020 %	0.86 ± 0.03 %	0.064 ± 0.013 %
Soft μ, CMX	0.86 ± 0.03 %	0.044 ± 0.012 %	0.80 ± 0.02 %	0.045 ± 0.011 %
All Types	5.44 ± 0.07 %	0.402 ± 0.036 %	5.06 ± 0.06 %	0.233 ± 0.026 %

Table 7.1: Soft lepton flavor tag $\sum_i \epsilon_i D^2_{raw}$ where the sum is in bins of soft lepton P_t(rel).

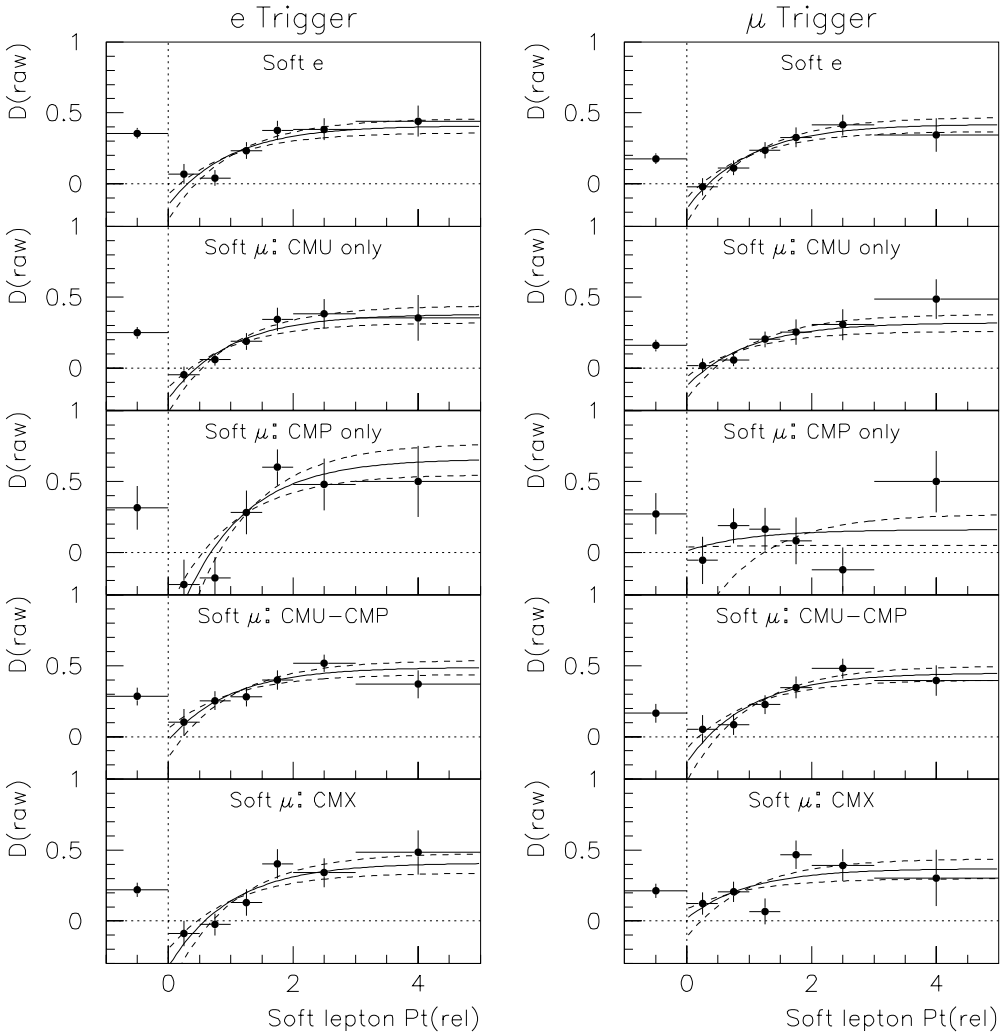

Figure 7.1: The soft lepton raw dilution as a function of the soft lepton P_t(rel). The data are divided into the 5 soft lepton types for the e and μ triggers. The negative P_t(rel) point is for events where the soft lepton is isolated and does not have a P_t(rel) measurement. The solid curve is used in the event-by-event dilution prediction. The dashed curves are used in the evaluation of the systematic error on the dilution parameterization.

Chapter 8

Determination of Δm_d and the Dilution Normalization N_D

The main objectives of this thesis are to measure the difference $\Delta m_d = m_{B_H} - m_{B_L}$, which is the difference in mass between the mass eigenstates of the B_d^0 hadron ($|B_H\rangle$ and $|B_L\rangle$), and to evaluate the performance of the flavor tagging methods used. An unbinned maximum likelihood fit is used to simultaneously determine Δm_d and the dilution normalization factors (N_D) for the different flavor taggers. The B_d^0 mixing frequency Δm_d is determined from the proper time dependence of the mixing probability.

First the probability density used in determining each event's contribution to the overall likelihood is described. Next, the convolution of the probability density with the experimental resolution on the transverse decay length L_{xy} and the estimation of $P_t(B)$ is discussed. Finally, the results of the fit are presented along with a description of the systematic errors on Δm_d and the N_D factors.

8.1 The Probability Density

The proper time dependent probability that a B^0 decayed in a state of opposite (mixed) or the same (mixed) flavor as that at the time of production is

$$P_{B_i}^{mix}(t_0) = \frac{1}{2}(1 - \cos(\Delta m_i \ t_0)) \tag{8.1}$$

$$P_{B_i}^{unmix}(t_0) = \frac{1}{2}(1 + \cos(\Delta m_i \ t_0)) \tag{8.2}$$

where t_0 is the proper time at decay, i is either d or s, and Δm_i is the mixing frequency. The B_s^0 mixing frequency Δm_s is assumed to be very large [49] [50]. The B_d^0 mixing frequency Δm_d is free in the fit.

The jet charge and the soft lepton flavor taggers give a raw tag dilution on an event-by-event basis. This raw dilution needs to be rescaled, for the reasons described in Section 5.1.2, by the factor N_D or

$$D = N_D \cdot D(raw). \tag{8.3}$$

The dilution normalization factor N_D is a free parameter in the fit. The probability of tagging or mistagging the event in terms of the dilution is given by

$$P^{tag}(D) = \frac{1}{2}(1 + D) \tag{8.4}$$

$$P^{mistag}(D) = \frac{1}{2}(1 - D) \tag{8.5}$$

First consider the simple case of a B_d sample that is free of sequential decays. The event is classified as **same sign** or **opposite sign** by comparing the sign of the flavor

tag with the sign of the trigger lepton charge. The probability densities for same sign and opposite sign events are given by

$$P_{SS}(t_0, D : B_d) = \frac{1}{\tau_{B_d}} e^{-\frac{t_0}{\tau_{B_d}}} \left\{ P^{tag}(D) \cdot P^{mix}_{B_d}(t_0) + P^{mistag}(D) \cdot P^{unmix}_{B_d}(t_0) \right\} \quad (8.6)$$

$$P_{OS}(t_0, D : B_d) = \frac{1}{\tau_{B_d}} e^{-\frac{t_0}{\tau_{B_d}}} \left\{ P^{tag}(D) \cdot P^{unmix}_{B_d}(t_0) + P^{mistag}(D) \cdot P^{mix}_{B_d}(t_0) \right\} \quad (8.7)$$

Note that

$$P_{SS}(t_0, D : B_d) + P_{OS}(t_0, D : B_d) = \frac{1}{\tau_{B_d}} e^{-\frac{t_0}{\tau_{B_d}}}$$

and

$$\int_0^\infty \left\{ P_{SS}(t_0, D : B_d) + P_{OS}(t_0, D : B_d) \right\} dt_0 = 1$$

thus, the probability densities are properly normalized.

The term for B_s mesons in the absence of sequentials is of the same form. The terms for B_u and Λ_b are simpler since they cannot mix. They are

$$P_{SS}(t_0, D : B_u) = \frac{1}{\tau_{B_u}} e^{-\frac{t_0}{\tau_{B_u}}} \left\{ P^{mistag}(D) \right\} \quad (8.8)$$

$$P_{OS}(t_0, D : B_u) = \frac{1}{\tau_{B_u}} e^{-\frac{t_0}{\tau_{B_u}}} \left\{ P^{tag}(D) \right\} \quad (8.9)$$

$$P_{SS}(t_0, D : \Lambda_b) = \frac{1}{\tau_{\Lambda_b}} e^{-\frac{t_0}{\tau_{\Lambda_b}}} \left\{ P^{mistag}(D) \right\} \quad (8.10)$$

$$P_{OS}(t_0, D : \Lambda_b) = \frac{1}{\tau_{\Lambda_b}} e^{-\frac{t_0}{\tau_{\Lambda_b}}} \left\{ P^{tag}(D) \right\} \quad (8.11)$$

We now have all of the pieces to put together a $b\bar{b}$ probability density in the absence of sequentials.

$$P^{\star}_{SS}(t_0, D : b\bar{b}) = f'_{B_d} \cdot P_{SS}(t_0, D : B_d) + f'_{B_s} \cdot P_{SS}(t_0, D : B_s)$$

$$+f'_{B_u} \cdot P_{SS}(t_0, D : B_u) + f'_{\Lambda_b} \cdot P_{SS}(t_0, D : \Lambda_b) \qquad (8.12)$$

$$P^{\star}_{OS}(t_0, D : b\bar{b}) = f'_{B_d} \cdot P_{OS}(t_0, D : B_d) + f'_{B_s} \cdot P_{OS}(t_0, D : B_s)$$

$$+f'_{B_u} \cdot P_{OS}(t_0, D : B_u) + f'_{\Lambda_b} \cdot P_{OS}(t_0, D : \Lambda_b) \qquad (8.13)$$

The B hadron fractions are primed because they have been corrected for the semileptonic branching fractions (see Section 8.3).

The charge of a trigger lepton from a sequential decay ($b \to c\ X$; $c \to s\ l\ \nu$) has the wrong sign. That is, it's charge is opposite that of the b quark at decay, not the same. Any lepton in the B decay products that is not from a direct decay is defined as a "sequential" lepton. This includes leptons from J/ψ decay, which will be sign random with respect to the B flavor at decay. Because of this, the probability that the trigger lepton is not from a direct decay **and** that it has the wrong sign is defined as P^{seq}_{ws}. The $b\bar{b}$ probability density is modified using P^{seq}_{ws} in the following way.

$$P_{SS}(t_0, D : b\bar{b}) = \{1 - P^{seq}_{ws}\} \cdot P^{\star}_{SS}(t_0, D : b\bar{b})$$

$$+P^{seq}_{ws} \cdot P^{\star}_{OS}(t_0, D : b\bar{b}) \qquad (8.14)$$

$$P_{OS}(t_0, D : b\bar{b}) = \{1 - P^{seq}_{ws}\} \cdot P^{\star}_{OS}(t_0, D : b\bar{b})$$

$$+P^{seq}_{ws} \cdot P^{\star}_{SS}(t_0, D : b\bar{b}) \qquad (8.15)$$

The $c\bar{c}$ component has the same form as the B_u and Λ_b terms. It is given by

$$P_{SS}(t_0, D, D_{c\bar{c}}/D_{b\bar{b}} : c\bar{c}) = \frac{1}{\tau_{c\bar{c}}} e^{-\frac{t_0}{\tau_{c\bar{c}}}} \left\{ P^{mistag}(D \cdot D_{c\bar{c}}/D_{b\bar{b}}) \right\} \qquad (8.16)$$

$$P_{OS}(t_0, D, D_{c\bar{c}}/D_{b\bar{b}} : c\bar{c}) = \frac{1}{\tau_{c\bar{c}}} e^{-\frac{t_0}{\tau_{c\bar{c}}}} \left\{ P^{tag}(D \cdot D_{c\bar{c}}/D_{b\bar{b}}) \right\}. \qquad (8.17)$$

There are essentially no fake trigger electrons (0.6 ± 0.5 %). However, there are a significant number of fake trigger muons. The uncertainty on the number of fake trigger muons is also rather large (12 ± 6 %). Figure 8.1 shows the reconstructed ct distribution of the single track trigger sample compared with the μ trigger data and $b\bar{b}$ Monte Carlo. The single track trigger sample, which represents the behavior of fake muons, has roughly the same shape as the data and the $b\bar{b}$ Monte Carlo. It is assumed that fake muons are mostly from $b\bar{b}$ events and have zero dilution.

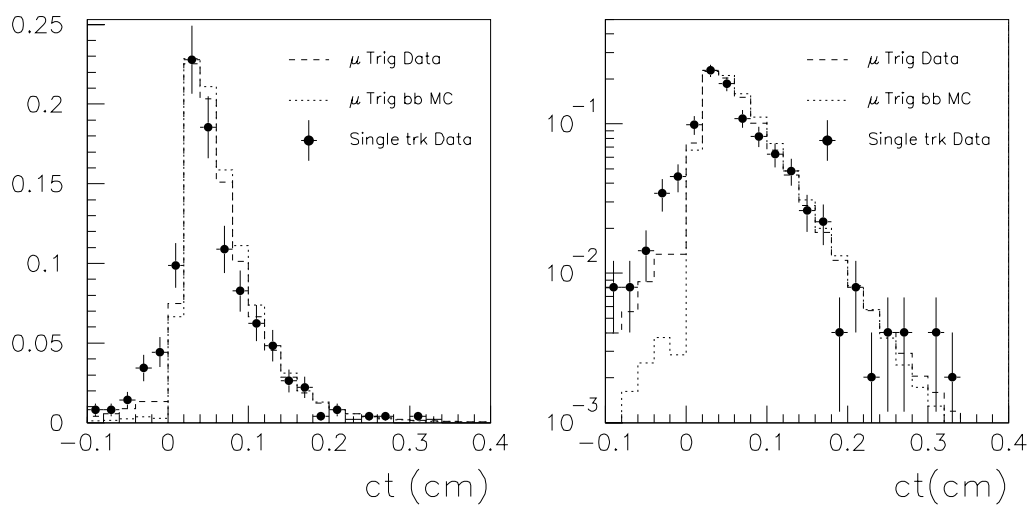

Figure 8.1: The ct distributions for the single track trigger sample, μ trigger data, and μ trigger $b\bar{b}$ Monte Carlo. All distributions are normalized to unit area.

Now we have all of the components. The total same sign and opposite sign probability densities are given by

$$P_{SS}(t_0, D, D_{c\bar{c}}/D_{b\bar{b}}) \quad = \quad f_{b\bar{b}} \cdot P_{SS}(t_0, D : b\bar{b})$$

$$+f_{c\bar{c}} \cdot P_{SS}(t_0, D, D_{c\bar{c}}/D_{b\bar{b}} : c\bar{c})$$

$$+f_{fl} \cdot P_{SS}(t_0, D = 0 : b\bar{b}) \tag{8.18}$$

$$\begin{aligned} P_{OS}(t_0, D, D_{c\bar{c}}/D_{b\bar{b}}) &= f_{b\bar{b}} \cdot P_{OS}(t_0, D : b\bar{b}) \\ &+f_{c\bar{c}} \cdot P_{OS}(t_0, D, D_{c\bar{c}}/D_{b\bar{b}} : c\bar{c}) \\ &+f_{fl} \cdot P_{SS}(t_0, D = 0 : b\bar{b}) \end{aligned} \tag{8.19}$$

where f_{fl} is the fraction of events with a zero dilution fake muon for the muon trigger data and zero for the electron trigger data.

8.2 Convolution of ct Resolution With the Probability Density

The K-factor distributions, described in Section 4.2, are used to convolute the experimental P_t resolution with the probability density. Figure 8.2 shows a generic K-factor distribution that will be used to illustrate the P_t resolution convolution. Given an observed $m(cl)$ and $P_t(cl)$ which fall into $m(cl)$ bin i and $P_t(cl)$ bin j, the ij^{th} K-factor distribution is stepped through calculating the value and relative probability of the true $P_t(B)$ for each bin. Referring to Figure 8.2, the true $P_t(B)$ for the αth bin is given by

$$P_t(B)_\alpha = P_t(cl)/K(ij)_\alpha \tag{8.20}$$

with the probability $w(ij)_\alpha$, thus giving a value for the true ct

$$ct_{0\ \alpha} = \frac{L^0_{xy} \cdot m_B}{P_t(B)_\alpha}. \tag{8.21}$$

Explicitly, the convolution of the K-factor distribution with P_{SS}, and similarly for P_{OS}, is given by

$$\sum_{\alpha} w(ij)_{\alpha} \cdot K(ij)_{\alpha} \; P_{SS}(t_{0\ \alpha}) \tag{8.22}$$

where the factor of $f(ij)_{\alpha}$ is necessary for proper relative normalization of the exponentials in $P_{SS}(t_{0\ \alpha})$ throughout the sum over α.

For the resolution on L^r_{xy}, the convolution of $R_{L_{xy}}$ with P_{SS} and P_{OS} is an integral which can be solved analytically [51]. Adding this to Equation 8.22 gives

$$\mathcal{P}_{\mathcal{SS}} = \sum_{\alpha} w(ij)_{\alpha} \cdot K(ij)_{\alpha} \int_0^{\infty} dL^0_{xy} \; P_{SS}(t_{0\ \alpha}) \cdot R_{L_{xy}} \left(L^0_{xy}, L^r_{xy} \right). \tag{8.23}$$

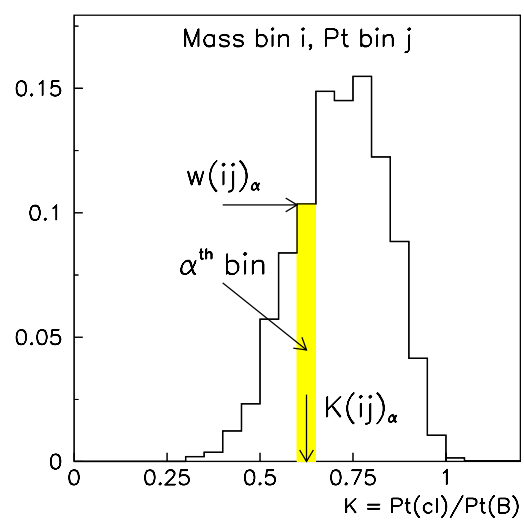

Figure 8.2: A generic K-factor distribution.

Finally, the overall negative log likelihood is given by

$$-ln\,\mathcal{L} = -\sum_{i}^{SS} ln\ (\mathcal{P}_{SS\ i}) - \sum_{j}^{OS} ln\ (\mathcal{P}_{OS\ j}) \tag{8.24}$$

where the sum over i (j) is for all same sign (opposite sign) events. The minimization of $-ln\mathcal{L}$ was performed with the MINUIT [52] software package.

8.3 Fit Parameters

Table 8.1 summarizes the parameters involved in the fit. The B lifetimes and hadron fractions all come from the '96 PDG [5]. The B hadron fractions are adjusted in the fit for their semileptonic branching fractions using the hadron lifetimes. This assumes that the partial width , ($b \to c\ l\nu$) is the same for all B hadrons thus the semileptonic branching fractions follow the lifetimes. Explicitly,

$$\begin{aligned} f'_{B_i} &= f_{B_i} \cdot c\tau_{B_i}/K \\ K &= \sum_i f_{B_i} \cdot c\tau_{B_i} \end{aligned}$$

where B_i is B_u, B_d, B_s, or Λ_b.

An effective $c\bar{c}$ lifetime was determined by fitting the reconstructed ct distribution of the $c\bar{c}$ Monte Carlo, where ct is reconstructed as if it were a B decay. That is, the B mass and the $b\bar{b}$ K-factor correction is used. Figure 8.3 shows the results of the fit for the e and μ trigger. Both give an effective lifetime of 460 μm. A 60 μm uncertainty is assigned to this number.

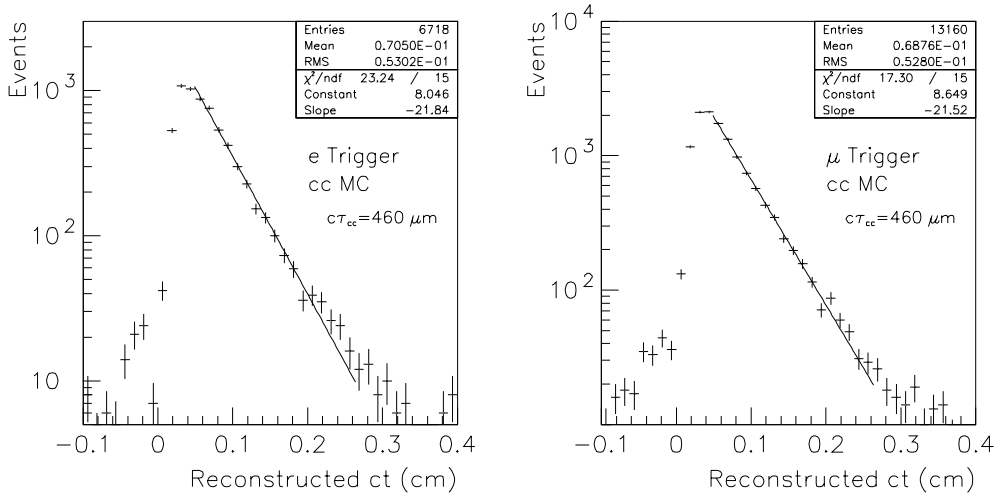

Figure 8.3: Determination of effective $c\bar{c}$ lifetime from the e and μ trigger $c\bar{c}$ Monte Carlo.

Parameter	Value	Source
$c\tau_{Bd}$	468 ± 18 μm	'96 PDG
$c\tau_{Bu}/c\tau_{Bd}$	1.02 ± 0.05	'96 PDG
$c\tau_{Bs}$	483^{+30}_{-27} μm	'96 PDG
$c\tau_{\Lambda_b}$	342 ± 24 μm	'96 PDG
$c\tau_{c\bar{c}}$	460 ± 60 μm	fit to $c\bar{c}$ MC
f_{B_u}	37.8 ± 2.2 %	'96 PDG
f_{B_d}	37.8 ± 2.2 %	'96 PDG
f_{B_s}	$11.1^{+2.5}_{-2.6}$ %	'96 PDG
f_{Λ_b}	13.2 ± 4.1 %	'96 PDG
JC $D_{c\bar{c}}/D_{b\bar{b}}$	0.5	Assumption
SLT $D_{c\bar{c}}$	0.5	Assumption
D_{fv}/D_{bb}	0.5	Assumption
f_{seq}	e: 9.4 %	MC
	μ: 13.6 %	
Δm_s	700 $\hbar$ ps^{-1}	Assumption
N_D	Free in fit	
Δm_d	Free in fit	

Table 8.1: Parameters of the fit and their sources.

8.4 Fit Range in ct

The reader may have noticed that there has been no discussion thus far of the secondary vertexing algorithms efficiency turn-on in ct. Specifically, how it affects the normalization of the probability density. The efficiency is a function of the observed (smeared) ct, not the true ct. This means it is a multiplicative constant in $\mathcal{P}_{SS}$ (or $\mathcal{P}_{OS}$) for each event. Moreover, this constant does not depend on Δm_d or N_D. In equation 8.24, the efficiency constants, one for each event, form an additional sum which shifts the likelihood by a constant. A maximum likelihood fit is not affected by an additional constant as long as the constant does not depend on the parameters being varied in the fit.

We are free to choose a specific range of ct for the fit for the same reason that the efficiency is not an issue. In fact, the ct range is an effective efficiency. The $ct < 0$ region has an excess in the data over expectations from the Monte Carlo, fake leptons, and leptons not from B decay. There is also evidence that backgrounds may exist near $ct = 0$. Any background that is relatively flat in ct will become significant compared to the data for large values of ct. We choose the range 0.02 cm $< ct < 0.3$ cm for the fit for Δm_d and N_D.

8.5 Results of Fit for Δm_d

Figure 8.4 shows the raw same-sign fraction as a function of the reconstructed ct for the jet charge and soft lepton flavor tagged data. These are shown to illustrate the ct dependence of the B_d^0 mixing as seen in the data. Recall that the fit for Δm_d is an unbinned fit and that events with high dilution have a higher weight in the fit. The plots in Figure 8.4 treat every event equally.

Figure 8.5 shows the raw same sign fraction for the combined jet charge and soft lepton tagged e and μ trigger data. A representation of the fit result is superimposed on the data. Like the plots in Figure 8.4, each event has an equal weight. This means a χ^2 fit to the points would *not* give the same result as the unbinned maximum likelihood fit.

Tables 8.2 and 8.3 give the fit results for the e and μ trigger data respectively. Results for the individual flavor taggers are given as well as a combined fit which uses both jet charge and soft lepton flavor tags. Events with a soft lepton must have a positive dilution estimate (from the soft lepton $P_t(rel)$) in order to be used in the fit. If an event has both a soft lepton and a jet charge flavor tag, the soft lepton is used for the flavor tag since it has significantly higher dilution. The jet charge N_D values in the combined fits are somewhat low because the SLT events were removed from the jet charge sample. These events have higher than average dilution for the jet charge tag. Since the raw dilution as a function of $|Q_{jet}|$ was not redone for the

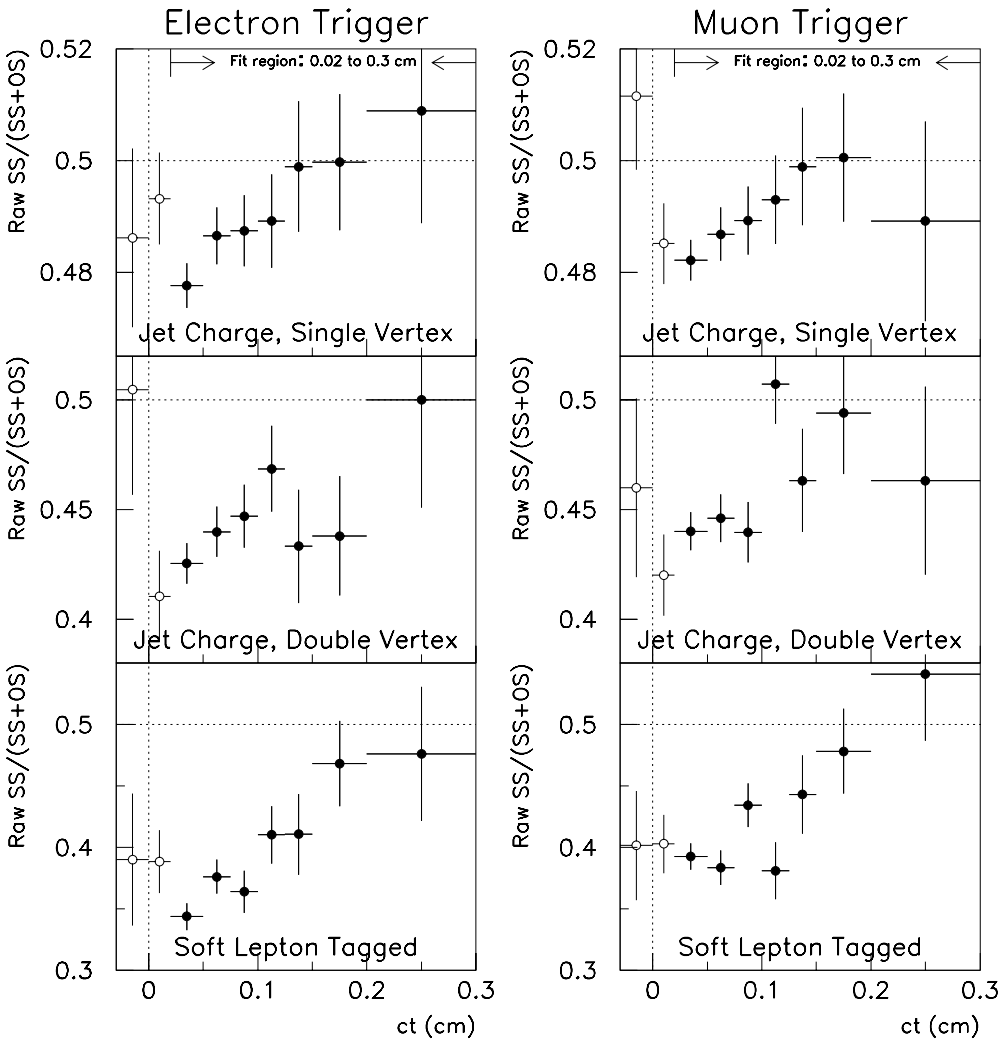

Figure 8.4: The raw same sign fraction as a function of the reconstructed proper time for the jet charge and soft lepton tagged e and μ trigger data.

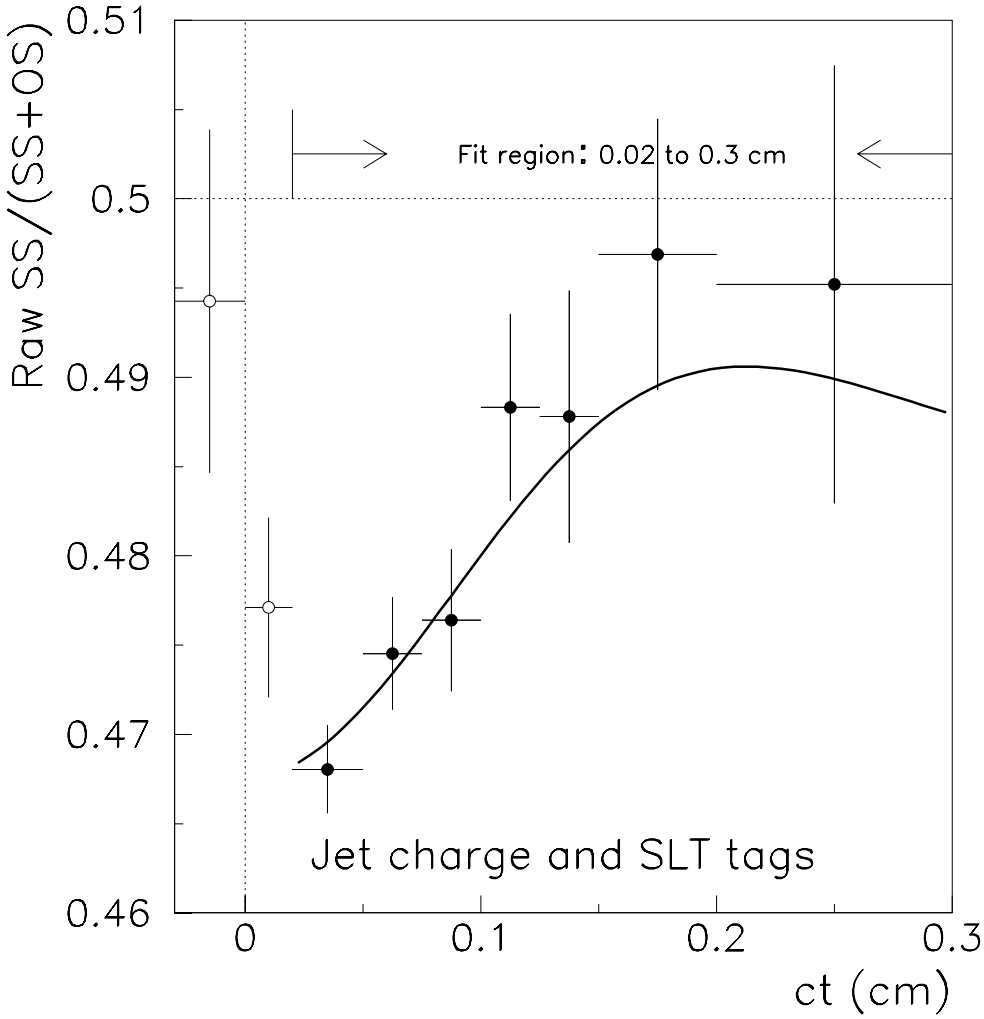

Figure 8.5: The raw same sign fraction as a function of the reconstructed proper time for the combined jet charge and soft lepton tagged e and μ trigger data. The curve is a representation of the fit result.

jet charge events without the SLT tagged events, N_D will be low in the combined fits since the average jet charge dilution has been lowered.

Based on the sample composition ($f_{b\bar{b}}$, $f_{c\bar{c}}$, f_{seq}, etc...) and an estimated time-integrated mixing probability, we expect the N_D values to be around 1.7 and 2.0 for the e and μ trigger respectively using Equation 5.10. Some of the N_D values are significantly above the expected value, but these fits also have unusually high values for Δm_d. Table 8.4 lists the correlation coefficients between Δm_d and N_D for the different flavor taggers and triggers. There is a significant positive correlation between Δm_d and N_D. This means a fit with an upward fluctuation in N_D will also have a high value of Δm_d and vice versa.

8.6 Systematic Errors

The systematic errors on Δm_d and the flavor tag dilution normalization N_D constants were evaluated by varying the fixed input parameters to the fit, one by one, by $\pm 1\ \sigma$ and adding the deviations from the nominal fit result values in quadrature. This does not take into account any correlations between the fixed input parameters so the total systematic error is conservative (slightly overestimated). Tables 8.6, 8.7, 8.8, and 8.9 summarize the results of the fixed parameter variations for the SLT and jet charge fits for the electron and muon trigger data. Below, we give a brief description of each fixed parameter variation.

- $c\tau_{B_d}$, $c\tau_{B_s}$, $c\tau_{\lambda_b}$, and $c\tau_{B_u}/c\tau_{B_d}$: These were varied by their quoted errors from the '96 PDG [5]. The variation of $c\tau_{B_u}/c\tau_{B_d}$ (1.02 ± 0.05) gives one of the largest single systematic error on Δm_d. The value of Δm_d is sensitive to $c\tau_{B_u}/c\tau_{B_d}$ because if the B_u and B_d hadrons have different lifetimes, the shape of the expected same sign fraction as a function of the proper time at decay changes. Recall that the data have roughly equal numbers of B_u and B_d hadrons.

- SLT $D(raw)$ vs soft lepton $P_t(rel)$: The parameters describing the soft lepton dilution as a function of the soft lepton $P_t(rel)$ were varied by their statistical errors. This variation is shown in Figure 7.1. This variation changes the effective weight of the SLT events relative to each other.

- Jet charge $D(raw)$ vs $|Q_{jet}|$: The raw dilution of the $|Q_{jet}| = 1$ events relative to the linear parameterization of $D(raw)$ vs $|Q_{jet}|$ was varied by the statistical error on the raw dilution of the $|Q_{jet}| = 1$ events.

- SLT $D_{c\bar{c}}$ and jet charge $D_{c\bar{c}}/D_{b\bar{b}}$: No reliable estimate for the dilution of $c\bar{c}$ events exists for the flavor taggers used. The SLT $D_{c\bar{c}}$ and jet charge $D_{c\bar{c}}/D_{b\bar{b}}$ values were varied from their minimum to maximum possible values.

- $f_{c\bar{c}}$: The fraction of $c\bar{c}$ events in the individual samples were varied by the uncertainties listed in Table 3.6.

- $c\tau_{c\bar{c}}$: The effective lifetime of $c\bar{c}$ events was varied by 60 μm.

- f_{B_s} and f_{Λ_b}: The B_s and Λ_b hadron fractions were varied by their quoted errors from the '96 PDG [5], absorbing the variation in the other parameters while keeping the ratios between the other parameters constant.

- f_{seq}: The fraction of trigger leptons from sequential decays (non-direct decays) was determined from the Monte Carlo. This fraction was varied by 25% of it's value.

- Δm_s: The default value for Δm_s was assumed to be very large; half of the B_s^0 hadrons decay with opposite their original flavor. Δm_s was lowered to 6.7 ps^{-1}, which is close to the current lower limit [49] [50].

- $D_{fv}/D_{b\bar{b}}$ and R_{fv} Scale factor: Since there is a significant excess of $L_{xy} < 0$ events over what is expected, it was assumed there may be an L_{xy} symmetric background. The excess $L_{xy} < 0$ shape was reflected on to the positive side and was assumed to have a dilution relative to $b\bar{b}$ events given by $D_{fv}/D_{b\bar{b}}$. R_{fv} is amount of this background relative to the rest of the data.

- F_{fl}: The fake μ fraction was estimated to be 12 % with an uncertainty of 6 % (see Appendix B).

Electron Trigger			
Data Set	Events	Δm_d ($\hbar$ ps^{-1})	Dilution Normalization: N_D
SLT	4,872	.45 ± .08 ± .05	$N_D(SLT)$: 1.66 ± 0.12 ± 0.18
JC, SV	39,621	.56 ± .15	$N_D(SV)$: 2.03 ± 0.28
JC, DV	7,366	.33 ± .11	$N_D(DV)$: 1.62 ± 0.17
JC, SV & DV	47,048	.42 ± .09 ± .03	$N_D(SV)$: 1.84 ± 0.23 ± 0.19 $N_D(DV)$: 1.71 ± 0.16 ± 0.11
SLT & JC	48,016	.45 ± .06 ± .04	$N'_D(JC, SV)$: 1.38 ± 0.22 ± 0.19 $N'_D(JC, DV)$: 1.49 ± 0.16 ± 0.11 $N_D(SLT)$: 1.67 ± 0.11 ± 0.18

Table 8.2: Results of the fits for Δm_d and N_D for the electron trigger data. The first errors are statistical and the second systematic. The systematic errors were evaluated for the jet charge and soft lepton flavor tags separately and are summarized in Tables 8.8 and 8.6. The systematic errors for the combined fit were calculated from the tables mentioned above, taking into account the correlated and uncorrelated variations.

Muon Trigger			
Data Set	Events	Δm_d ($\hbar$ ps^{-1})	Dilution Normalization: N_D
SLT	5,075	.50 ± .09 ± .05	$N_D(SLT)$: 2.05 ± 0.19 ± 0.37
JC, SV	45,779	.79 ± .15	$N_D(SV)$: 3.05 ± 0.43
JC, DV	8,316	.58 ± .16	$N_D(DV)$: 2.41 ± 0.33
JC, SV & DV	54,095	.68 ± .11 ± .04	$N_D(SV)$: 2.86 ± 0.40 ± 0.43 $N_D(DV)$: 2.52 ± 0.28 ± 0.25
SLT & JC	54,998	.58 ± .09 ± .05	$N'_D(JC, SV)$: 2.12 ± 0.36 ± 0.43 $N'_D(JC, DV)$: 2.12 ± 0.26 ± 0.25 $N_D(SLT)$: 2.16 ± 0.19 ± 0.37

Table 8.3: Results of the fits for Δm_d and N_D for the muon trigger data. The first errors are statistical and the second systematic. The systematic errors were evaluated for the jet charge and soft lepton flavor tags separately and are summarized in Tables 8.9 and 8.7. The systematic errors for the combined fit were calculated from the tables mentioned above, taking into account the correlated and uncorrelated variations.

Δm_d - N_D Correlation Coefficients		
Flavor Tag	e Trigger	μ Trigger
SLT	+.73	+.68
JC, SV	+.70	+.55
JC, DV	+.71	+.81

Table 8.4: Correlation coefficients for the free parameters Δm_d and N_D in the fit.

e & μ Trig, JC & SLT Combined Fit	
Parameter	Value
Δm_d	$0.50 \pm 0.05 \pm 0.05\ \hbar\ \mathrm{ps}^{-1}$
$N'_D(e : JC, SV)$	$1.43 \pm 0.22 \pm 0.19$
$N'_D(e : JC, DV)$	$1.53 \pm 0.16 \pm 0.11$
$N_D(e : SLT)$	$1.72 \pm 0.10 \pm 0.18$
$N'_D(\mu : JC, SV)$	$1.99 \pm 0.32 \pm 0.43$
$N'_D(\mu : JC, DV)$	$2.00 \pm 0.22 \pm 0.25$
$N_D(\mu : SLT)$	$2.05 \pm 0.16 \pm 0.37$

Table 8.5: Result of the e and μ trigger, jet charge and soft lepton combined fit. The first errors are statistical and the second systematic. The systematic errors were calculated from Tables 8.6, 8.7, 8.8, and 8.9 taking into account the correlated and uncorrelated variations.

SLT Flavor Tag, e Trigger					
Parameter	Variation	$\delta\Delta m_d$ ($\hbar$ ps^{-1})		δN_D	
SLT, e: $D_{c\bar{c}}$	[0, 1]	− 0.039	+ 0.042	+ 0.14	− 0.15
SLT, e: $f_{c\bar{c}}$	(7.1 ± 1.7) %	+ 0.010	− 0.009	− 0.01	+ 0.00
$c\tau_{B_d}$	468 ± 18 μm	− 0.004	+ 0.004	− 0.01	+ 0.01
$c\tau_{B_u}/c\tau_{B_d}$	1.02 ± 0.05	+ 0.020	− 0.022	+ 0.01	− 0.01
$c\tau_{\Lambda_b}$	342 ± 24 μm	+ 0.005	− 0.004	− 0.00	+ 0.00
$c\tau_{B_s}$	483 ± 30 μm	− 0.007	+ 0.007	+ 0.00	− 0.01
$c\tau_{c\bar{c}}$	460 ± 60 μm	+ 0.007	− 0.009	+ 0.01	− 0.01
f_{B_s}	$(11.1^{+2.5}_{-2.6})$ %	− 0.001	+ 0.001	+ 0.05	− 0.05
f_{Λ_b}	(13.2 ± 4.1) %	+ 0.007	− 0.007	− 0.01	+ 0.01
e: f_{seq}	(9.4 ± 2.4) %	− 0.003	+ 0.003	+ 0.06	− 0.06
Δm_s	$\rightarrow$ 6.7 $\hbar$ ps^{-1}	− 0.003		− 0.01	
D_{raw} Param		+ 0.015	− 0.016	+ 0.05	− 0.06
$D_{fv}/D_{b\bar{b}}$	[0, 1]	+ 0.005	− 0.004	+ 0.04	− 0.04
R_{fv} Scale factor	[0, 2]	− 0.008	+ 0.007	− 0.02	+ 0.02
Total Systematics		**+0.053** $\hbar$ ps^{-1} **−0.051** $\hbar$ ps^{-1}		**+0.18** **−0.18**	

Table 8.6: Systematic errors for the fit for Δm_d and the N_D factors for the soft lepton tagged e trigger data.

SLT Flavor Tag, μ Trigger					
Parameter	Variation	$\delta\Delta m_d$ ($\hbar$ ps^{-1})		δN_D	
SLT, μ: $D_{c\bar{c}}$	[0, 1]	− 0.034	+ 0.037	+ 0.25	− 0.26
SLT, μ: $f_{c\bar{c}}$	(7.8 ± 1.6) %	+ 0.007	− 0.007	− 0.02	+ 0.02
$c\tau_{B_d}$	468 ± 18 μm	− 0.006	+ 0.007	− 0.01	+ 0.01
$c\tau_{B_u}/c\tau_{B_d}$	1.02 ± 0.05	+ 0.014	− 0.016	− 0.00	+ 0.00
$c\tau_{\Lambda_b}$	342 ± 24 μm	+ 0.003	− 0.003	− 0.00	+ 0.00
$c\tau_{B_s}$	483 ± 30 μm	− 0.004	+ 0.004	+ 0.01	− 0.01
$c\tau_{c\bar{c}}$	460 ± 60 μm	+ 0.008	− 0.009	+ 0.01	− 0.01
f_{B_s}	$(11.1^{+2.5}_{-2.6})$ %	− 0.001	+ 0.001	+ 0.06	− 0.06
f_{Λ_b}	(13.2 ± 4.1) %	+ 0.006	− 0.005	− 0.01	+ 0.01
μ: f_{seq}	(13.6 ± 3.4) %	− 0.005	+ 0.005	+ 0.13	− 0.12
Δm_s	$\rightarrow$ 6.7 $\hbar$ ps^{-1}	− 0.002		− 0.01	
D_{raw} Param		+ 0.017	− 0.017	+ 0.06	− 0.08
F_{fl}	(12 ± 6) %	+ 0.002	− 0.002	− 0.16	+ 0.14
$D_{fv}/D_{b\bar{b}}$	[0, 1]	− 0.001	+ 0.000	+ 0.06	− 0.06
R_{fv} Scale factor	[0, 2]	− 0.005	+ 0.005	− 0.01	+ 0.01
Total Systematics		**+0.046** $\hbar$ ps^{-1}		**+0.36**	
		−0.044 $\hbar$ ps^{-1}		**−0.38**	

Table 8.7: Systematic errors for the fit for Δm_d and the N_D factors for the soft lepton tagged μ trigger data.

Jet Charge Flavor Tag, e Trigger							
Parameter	Variation	$\delta\Delta m_d$ ($\hbar$ ps^{-1})		$\delta N_D(SV)$		$\delta N_D(DV)$	
JC: $D_{c\bar{c}}/D_{b\bar{b}}$	[0, 1]	− 0.011	+ 0.011	+ 0.13	− 0.11	+ 0.05	− 0.04
JC,SV: $f_{c\bar{c}}$	(9.1 ± 1.3) %	+ 0.000	− 0.000	+ 0.00	− 0.00	+ 0.00	− 0.00
JC,DV: $f_{c\bar{c}}$	(4.4 ± 1.5) %	+ 0.003	− 0.003	+ 0.00	− 0.00	+ 0.01	− 0.01
$c\tau_{B_d}$	468 ± 18 μm	− 0.002	+ 0.002	− 0.01	+ 0.01	− 0.01	+ 0.01
$c\tau_{B_u}/c\tau_{B_d}$	1.02 ± 0.05	+ 0.022	− 0.022	+ 0.01	− 0.01	+ 0.01	− 0.01
$c\tau_{\Lambda_b}$	342 ± 24 μm	+ 0.004	− 0.004	− 0.00	+ 0.00	− 0.00	+ 0.00
$c\tau_{B_s}$	483 ± 30 μm	− 0.006	+ 0.005	+ 0.01	− 0.01	+ 0.01	− 0.01
$c\tau_{c\bar{c}}$	460 ± 60 μm	− 0.000	+ 0.001	− 0.00	+ 0.00	− 0.00	+ 0.00
f_{B_s}	$(11.1^{+2.5}_{-2.6})$ %	− 0.001	+ 0.001	+ 0.05	− 0.05	+ 0.05	− 0.05
f_{Λ_b}	(13.2 ± 4.1) %	+ 0.004	− 0.004	− 0.01	+ 0.01	− 0.01	+ 0.01
e: f_{seq}	(9.4 ± 2.4) %	− 0.004	+ 0.004	+ 0.07	− 0.06	+ 0.06	− 0.06
Δm_s	→ 6.7 $\hbar$ ps^{-1}	− 0.007		− 0.02		− 0.01	
D_{raw} Param		− 0.008	+ 0.009	− 0.10	+ 0.10	− 0.05	+ 0.04
$D_{fv}/D_{b\bar{b}}$	[0, 1]	+ 0.000	− 0.000	+ 0.06	− 0.05	+ 0.03	− 0.03
R_{fv} Scale	[0, 2]	− 0.005	+ 0.005	− 0.02	+ 0.02	− 0.01	+ 0.01
Total Systematics		**+0.028** $\hbar$ ps^{-1}		**+0.20**		**+0.11**	
		−0.028 $\hbar$ ps^{-1}		**−0.18**		**−0.11**	

Table 8.8: Systematic errors for the fit for Δm_d and the N_D factors for the jet charge tagged e trigger data.

Jet Charge Flavor Tag, μ Trigger							
Parameter	Variation	$\delta\Delta m_d$ ($\hbar$ ps^{-1})		$\delta N_D(SV)$		$\delta N_D(DV)$	
JC: $D_{c\bar{c}}/D_{b\bar{b}}$	[0, 1]	− 0.008	+ 0.005	+ 0.29	− 0.26	+ 0.03	− 0.03
JC,SV: $f_{c\bar{c}}$	(10.4 ± 1.3) %	+ 0.000	− 0.000	+ 0.00	− 0.00	+ 0.00	− 0.00
JC,DV: $f_{c\bar{c}}$	(1.8 ± 1.3) %	+ 0.004	− 0.004	+ 0.00	− 0.01	+ 0.01	− 0.00
$c\tau_{B_d}$	468 ± 18 μm	− 0.003	+ 0.003	− 0.00	+ 0.00	− 0.00	+ 0.00
$c\tau_{B_u}/c\tau_{B_d}$	1.02 ± 0.05	+ 0.008	− 0.015	− 0.02	+ 0.01	− 0.02	+ 0.01
$c\tau_{\Lambda_b}$	342 ± 24 μm	+ 0.006	− 0.006	− 0.00	+ 0.00	+ 0.01	− 0.00
$c\tau_{B_s}$	483 ± 30 μm	− 0.004	+ 0.004	+ 0.01	− 0.01	+ 0.01	− 0.01
$c\tau_{c\bar{c}}$	460 ± 60 μm	− 0.001	+ 0.001	− 0.01	+ 0.01	− 0.00	+ 0.00
f_{B_s}	$(11.1^{+2.5}_{-2.6})$ %	− 0.001	+ 0.001	+ 0.07	− 0.08	+ 0.07	− 0.07
f_{Λ_b}	(13.2 ± 4.1) %	+ 0.013	− 0.013	− 0.02	+ 0.02	− 0.02	+ 0.01
μ: f_{seq}	(13.6 ± 3.4) %	− 0.005	+ 0.005	+ 0.16	− 0.14	+ 0.15	− 0.13
Δm_s	$\rightarrow$ 6.7 $\hbar$ ps^{-1}	− 0.004		− 0.02		− 0.01	
D_{raw} Param		+ 0.022	− 0.026	+ 0.16	− 0.18	+ 0.02	− 0.03
F_{fl}	(12 ± 6) %	+ 0.000	− 0.001	+ 0.20	− 0.18	+ 0.18	− 0.15
$D_{fv}/D_{b\bar{b}}$	[0, 1]	+ 0.007	− 0.005	+ 0.13	− 0.12	+ 0.08	− 0.07
R_{fv} Scale	[0, 2]	− 0.001	+ 0.004	+ 0.00	− 0.00	− 0.00	+ 0.01
Total Systematics		**+0.030** $\hbar$ ps^{-1}		**+0.44**		**+0.26**	
		−0.036 $\hbar$ ps^{-1}		**−0.42**		**−0.24**	

Table 8.9: Systematic errors for the fit for Δm_d and the N_D factors for the jet charge tagged μ trigger data.

8.7 Check of the Fit Using a Fast Monte Carlo

A fast Monte Carlo program was used to check for systematic biases and the scale of the errors returned by MINUIT. The program generates events using resolution functions and parameters derived from the data. Many of sets of data with the statistics and dilution of the SLT, single vertex jet charge, and double vertex jet charge tagged data for both the e and μ triggers were generated and fit exactly as if they were real data. The distributions of the fitted values, their errors, and the deviation of the fitted values from the input values over the fitted error were examined.

As an example, Figure 8.6 shows the results of many fast Monte Carlo experiments simulating the soft lepton tagged e trigger data. The top plots show the spectrum of fitted values for Δm_d and the dilution normalization N_D. The mean of each distribution is equal to the input value. The middle plots show the spectrum of fitted errors with arrows indicating the values for the fit to the real data. The bottom plots show the distribution of δ/σ or the pull distribution for Δm_d and N_D. The width of both of these distributions is one verifying that MINUIT is calculating the errors properly. The fast monte carlo experiments for the other flavor tag data sets yielded similar results demonstrating that the error scale on Δm_d and N_D is correct and that the fit is free of any biases on Δm_d and N_D.

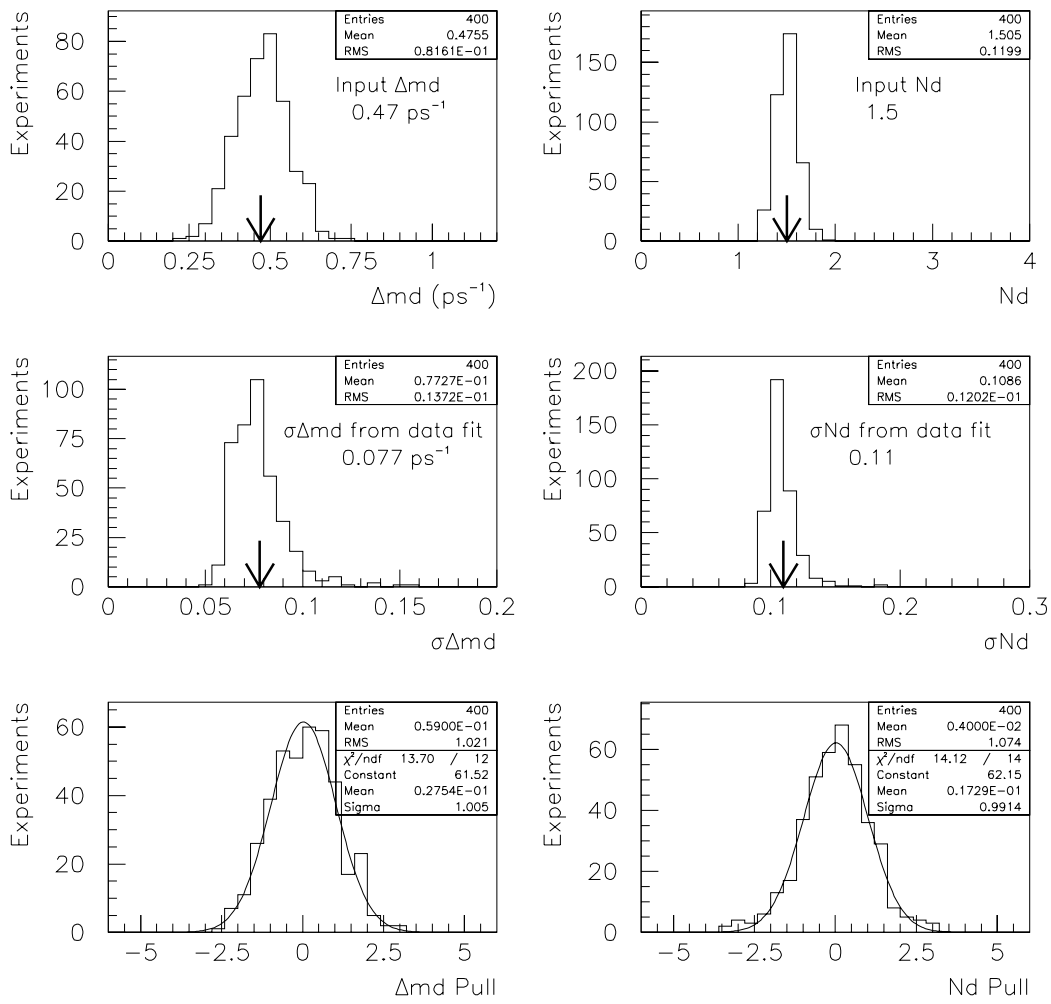

Figure 8.6: Several fast Monte Carlo experiments simulating the soft lepton tagged e trigger data.

8.8 Flavor Tag ϵD^2 Values

As discussed in section 5.1.1, the effectiveness of a flavor tagging method is usually quantified by ϵD^2. Tables 6.1 and 7.1 give the values of $\sum_i \epsilon_i D^2_{raw\ i}$ for the jet charge and SLT tags respectively. These numbers need to be corrected by N_D^2 to get the true ϵD^2. The fit for Δm_d gives the values for the N_D factors. However, the correlation between Δm_d and N_D (shown in Table 8.4) may introduce statistical fluctuations that can be avoided by fixing Δm_d to the world average [5] in the fit. Table 8.10 gives the values for the N_D factors where Δm_d has been fixed to 0.47 ps^{-1}.

Values for N_D, Δm_d fixed to 0.47 $\hbar$ ps^{-1}		
Flavor Tag	e Trigger	μ Trigger
Jet Charge, Single Vertex	1.88 ± 0.20 ± 0.15	2.41 ± 0.29 ± 0.39
Jet Charge, Double Vertex	1.76 ± 0.13 ± 0.09	2.14 ± 0.33 ± 0.25
Soft Lepton Tag	1.72 ± 0.08 ± 0.11	2.01 ± 0.13 ± 0.22

Table 8.10: Values for N_D factors, where Δm_d has been fixed to the world average: 0.47 $\hbar$ ps^{-1}. The first error is statistical, the second systematic.

Table 8.11 gives the ϵD^2 values, corrected with the N_D factors in 8.10, for the different flavor taggers. An average of the e and μ trigger results is included since ϵD^2 should in principle be the same for the two triggers.

Corrected ϵD^2			
Flavor Tag	e Trigger	μ Trigger	e, μ Average
JC, SV	.27 ± .06 ± .04 %	.28 ± .10 ± .09 %	.28 ± .06 ± .05 %
JC, DV	.49 ± .10 ± .05 %	.52 ± .18 ± .12 %	.51 ± .10 ± .07 %
JC, SV & DV	.76 ± .11 ± .07 %	.80 ± .21 ± .15 %	.78 ± .12 ± .09 %
Soft e	.40 ± .07 ± .05 %	.30 ± .05 ± .07 %	.35 ± .04 ± .04 %
Soft μ	.79 ± .11 ± .10 %	.64 ± .12 ± .14 %	.78 ± .12 ± .09 %
Soft e & μ	1.19 ± .15 ± .15 %	.94 ± .16 ± .21 %	1.07 ± .09 ± .10 %

Table 8.11: Vales for ϵD^2, corrected with the N_D factors in Table 8.10. The first error is statistical, the second systematic.

Chapter 9

Conclusion

The B_d^0 mixing frequency Δm_d has been measured to be

$$\Delta m_d = 0.50 \pm 0.05 \text{ (stat)} \pm 0.05 \text{ (sys) } \hbar \text{ ps}^{-1}$$

in $p - \bar{p}$ collisions at $\sqrt{s} = 1.8$ TeV using jet charge and soft lepton flavor tagging in 91 pb^{-1} of the inclusive e and μ trigger data of the CDF detector. This is consistent with the world average for Δm_d which is 0.474 ± 0.031 $\hbar$ ps^{-1} [5] and is competitive with individual measurements from other experiments [23]. This measurement is the first application of jet charge flavor tagging in the difficult environment of hadronic collisions. The statistical power of the flavor taggers used was measured to be

- Jet Charge: $\epsilon D^2 = 0.78 \pm 0.12 \text{ (stat)} \pm 0.09 \text{ (sys) } \%$
- Soft Lepton: $\epsilon D^2 = 1.07 \pm 0.09 \text{ (stat)} \pm 0.10 \text{ (sys) } \%$

The CDFII detector expects to have a sample of 15,000 $B_d^0 \rightarrow J/\psi K_s^0$ events at the end of the next colliding beam run [27]. If the jet charge and soft lepton

flavor tagging methods were applied to this sample, using the measured ϵD^2 numbers above [1], the precision on a measurement of $\sin(2\beta)$ would be about 0.2. Including other flavor tagging methods and taking into account improvements in the detector reduces the expected error on $\sin(2\beta)$ to about 0.076 [27].

The study of CP violation in the B system promises to be an exciting test of the so far rock solid Standard Model. The jet charge and soft lepton flavor tagging methods are powerful tools that will make CDFII competitive with the dedicated B physics experiments being built in the United States [24], Japan [25], and Germany [26].

[1] The average P_t of the "other" B for the J/ψ trigger is lower than that for the inclusive lepton triggers. This may affect the efficiency (ϵ) and dilution (D) of the flavor taggers.

Appendix A

Glossary of Symbols and Acronyms

We provide here a list of symbols and acronyms used in this thesis, each with a brief description and a reference to it's use in the text.

- V: The CKM matrix which describes the coupling of the charge 2/3 quarks to the charge -1/3 quarks. Eqn. 1.3.

- A: A parameter (of order 1) in the Wolfenstein representation of the CKM matrix. Eqn. 1.7.

- λ: A parameter in the Wolfenstein representation of the CKM matrix. λ is the sin of the Cabbibo angle θ_C ($\sin\theta_C \approx 0.22$). Eqn. 1.7.

- ρ and η: Parameters in the Wolfenstein representation of the CKM matrix in the elements V_{ub} and V_{td}, which are expected to have non-zero phase. The top corner of the renormalized unitarity triangle (see Figure 1.1) is at the coordinates (ρ,η) in the complex plane. Eqn. 1.7.

- η: The variable η is also a geometric quantity, which is the "natural" unit orthogonal to ϕ in a $p-\bar{p}$ environment. η is 0 normal to the beam direction and infinite along the beam direction. $\eta = -\tan\left(ln\frac{\theta}{2}\right)$. Introduction of Chapter 2.

- α: An angle in the unitarity triangle (see Figure 1.1). The angle α can be measured from CP asymmetries involving the B_d^0 and a decay mode with a $b \to u$ transition. Table 1.1.

- γ: An angle in the unitarity triangle (see Figure 1.1). The angle γ is the phase of the CKM matrix element V_{ub} and can be measured from CP asymmetries involving the B_s^0 and a decay mode with a $b \to u$ transition. Table 1.1.

- β: An angle in the unitarity triangle (see Figure 1.1). The angle β is the phase of the CKM matrix element V_{td} and can be measured from CP asymmetries involving the B_d^0. The most notable decay mode for measuring β is $B_d^0 \to J/\psi K_s^0$ (the "golden" mode). Table 1.1.

- CP: A combination of the charge conjugation operator C, which switches particle to antiparticle, and the parity operator P, which inverts spatial directions ($\vec{x} \to -\vec{x}$). Section 1.3

- H: The effective mixing Hamiltonian in the $|B^0\rangle$, $|\bar{B}^0\rangle$ basis. Eqn. 1.11.

- M: The Hermitian mass matrix of H. Eqn. 1.11.

- , : The Hermitian width matrix of H. Eqn. 1.11.

- b: The b quark. Charge: -1/3 of the charge of the electron.

- B: A B meson which contains a $\bar{b}$ (an anti-b quark) and a light quark (u, d, s).

- $\bar{B}$: An anti-B meson which contains a b quark and a light anti-quark ($\bar{u}$, $\bar{d}$, $\bar{s}$).

- B^0: A neutral B meson containing a $\bar{b}$ and either a d or a s quark.

- $\bar{B}^0$: A neutral anti-B meson containing a b and either a $\bar{d}$ or a $\bar{s}$ quark.

- Δm_d: The mass difference between the B_{dH} and B_{dL}, which are linear combinations of the weak eigenstates B_d^0 and $\bar{B}_d^0$.

- $\bar{\chi_B}$: The probability that a B hadron decayed in a "mixed" state (the state opposite in flavor of it's production state) , averaged over all B hadron types. $\bar{\chi_B} = f_{B_d}\ \chi_{B_d} + f_{B_s}\ \chi_{B_s} \approx 13\%$. Section 5.1.

- ϵ: The efficiency for applying a flavor tag. Eqn. 5.8.

- D: The dilution of a flavor tag. Eqn. 5.1.

- D_{raw}: The raw dilution of a flavor tag. Eqn. 5.9.

- P_{tag}: The probability that the flavor tag is correct. Eqn. 5.2.

- P_{mistag}: The probability that the flavor tag is incorrect. Eqn. 5.3.

- P_t: The component of momentum transverse to the beam direction ($P_t = \sqrt{P_x^2 + P_y^2}$).
- E_t: The component of energy in the $x - y$ plane ($E_t = \sqrt{E_x^2 + E_y^2}$).
- D_0: The helix parameter which describes the closest distance of approach to the origin (see Figure 2.3).
- CTC: The **C**entral **T**racking **C**hamber. Subsection 2.1.3.
- SVX: The **S**ilicon **V**ertex **D**etector. Subsection 2.1.2.
- CEM: The **C**entral **E**lecro**M**agnetic calorimeter. Section 2.2.
- CFT: The **C**entral **F**ast **T**racker. Section 2.3.
- CMU: The **C**entral **MU**on chambers. Section 2.4.
- CMP: The **C**entral **M**uon **U**pgrade. Section 2.4.
- CDF: The **C**ollider **D**etector at **F**ermilab.

Appendix B

Fake Muon Estimate From Flavor Tag Dilution

The true dilution for the flavor tagging methods should in principle be the same in the muon and electron trigger data. The raw dilution assumes that all opposite (same) sign events are tags (mistags). The sign comparison is between the trigger lepton charge and either the sign of the jet charge or the sign of the soft lepton charge. The raw dilution is lower than the true dilution because of the following

1. The trigger jet B decays in a mixed state some of the time.

2. The trigger lepton is from a sequential decay.

3. The data are not pure $b\bar{b}$ events.

4. Some of the trigger leptons are fake.

Number 1 is the same for the electron and muon trigger data. Numbers 2 and 3 are not the same for the electron and muon trigger data, but the raw dilution can be corrected for these effects. The electron trigger data have essentially no fake electrons (0.6 $\pm$

0.5 %) and a small amount of residual conversion electrons (about 1.4 %), which have zero dilution. Comparing the raw dilution, corrected for 2 and 3, for the electron and muon tags gives an estimate of the excess of zero dilution events in the muon trigger data, which are presumed to be fake muons. Note that not all fake muons have zero dilution. For example, a B^+ that decays via ($\bar{b} \to \bar{c} \to \bar{s}$, u spectator) to a K^+ that punches through the calorimeter gives the same charge for the trigger "lepton" as a B^+ that decays semileptonically to a real muon. This estimate only measures the zero dilution excess in the muon trigger data.

Table B.1 gives the raw dilution in the electron and muon trigger data for the flavor taggers used in this analysis. The raw dilution numbers in Table B.1 need to

Flavor Tag	N_{SS}	N_{OS}	$\langle D_{raw} \rangle$	$\langle D_{raw}(e) \rangle / \langle D_{raw}(\mu) \rangle$
JC, SV (e)	23,506	24,803	2.7 ± 0.5 %	1.17 ± 0.30
JC, SV (μ)	27,447	28,726	2.3 ± 0.4 %	
JC, DV (e)	3,809	4,856	12.1 ± 1.1 %	1.25 ± 0.17
JC, DV (μ)	4,434	5,382	9.7 ± 1.0 %	
SLT (e)	2,211	3,468	22.1 ± 1.3 %	1.21 ± 0.11
SLT (μ)	2,285	3,303	18.2 ± 1.3 %	

Table B.1: Uncorrected average raw dilution for three flavor taggers in the electron and muon data.

Flavor Tag	$\langle D_{raw} \rangle$	Correction	$\langle D'_{raw} \rangle$	$\langle D'_{raw}(e) \rangle / \langle D'_{raw}(\mu) \rangle$
JC, SV (e)	2.7 ± 0.5 %	1.16	3.1 ± 0.6 %	1.07 ± 0.28
JC, SV (μ)	2.3 ± 0.4 %	1.26	2.9 ± 0.5 %	
JC, DV (e)	12.1 ± 1.1 %	1.15	14.2 ± 1.3 %	1.18 ± 0.16
JC, DV (μ)	9.7 ± 1.0 %	1.24	12.0 ± 1.2 %	
SLT (e)	22.1 ± 1.3 %	1.15	25.5 ± 1.5 %	1.13 ± 0.10
SLT (μ)	18.2 ± 1.3 %	1.24	22.5 ± 1.6 %	

Table B.2: Average raw dilution for three flavor taggers in the electron and muon data corrected for wrong sign sequential decay trigger leptons and the $b\bar{b}$ to $c\bar{c}$ ratio.

be corrected for the fraction of wrong sign sequentials and the $b\bar{b}$ to $c\bar{c}$ ratio in the data. This correction has the form

$$\langle D'_{raw} \rangle = \frac{\langle D_{raw} \rangle}{f_{b\bar{b}} \cdot (1 - 2f_{seq}(ws)) + f_{c\bar{c}} \cdot D_{c\bar{c}}/D_{b\bar{b}}} \tag{B.1}$$

The wrong sign sequential fractions are 6.4 % and 9.0 % for the electron and muon triggers respectively. We use the $f_{b\bar{b}}$ and $f_{c\bar{c}}$ values from Table 3.6. We assume $D_{c\bar{c}}/D_{b\bar{b}} = 0.5$. The corrected average raw dilution values are shown in Table B.2. The weighted average of $\langle D'_{raw}(e) \rangle / \langle D'_{raw}(\mu) \rangle$ gives 1.14 ± 0.08. Finally, the fraction of additional zero dilution events in the muon trigger data is approximately given by

$$f_{D=0}(\mu) = 1 - \frac{1}{\langle D'_{raw}(e) \rangle / \langle D'_{raw}(\mu) \rangle}. \tag{B.2}$$

The equation above gives $f_{D=0}(\mu) = 12 \pm 6$ %.

Bibliography

[1] S. Weinberg, Phys Rev. Lett. **19**, 1264 (1967);

A. Salam, Proc. 8th Nobel Symp. (Aspenäsgärden, 1968)

(Almqvist and Wiksell, Stockholm, 1968) p. 367.

[2] N. Cabibbo, Phys. Rev. Lett., **10**, 531 (1963).

[3] M. Kobayashi and K. Maskawa, Prog Theor. Phys **49**, 652 (1973).

[4] C. Quigg, *Gauge Theories of the Strong, Weak, and Electromagnetic Interactions.* Addison-Wesley, (1983).

[5] R. M. Barnett *et al.* (The Particle Data Group), Physical Review D**54**, 1 (1996).

[6] C. Athanassopoulos *et al.* Phys. Rev. Lett. **77**, 3082 (1996).

[7] E. W. Beier *et al.* Nucl. Phys. A **527**, 653c (1991).

[8] The CLEO Collaboration. Phys. Rev. Lett. **58**, 183 (1987).

[9] C. Albajar *et al.* Phys. Lett B **186**, 247 (1987).

[10] H. Albrecht *et al.* Phys. Lett. B **192**, 245 (1987).

[11] B. Adeva *et al.* Phys. Lett. B **252**, 703 (1990).

[12] D. Decamp *et al.* Phys. Lett. B **258**, 236 (1991).

[13] P. D. Acton *et al.* Phys. Lett. B **276**, 379 (1992).

[14] P. Abreu *et al.* Phys Lett. B **301**, 145 (1993).

[15] S. Stone. *Prospects for B-Physics in the Next Decade.* Presented at NATO ASI summer school, Virgin Islands, July 1996, HEPSY 96-01. The original measurement is from D. Besson *et al.* Phys. Rev. Lett **54**, 381 (1985).

[16] This is the inclusive b quark cross-section determined in S. Riemersma and R. Meng, *B-Quark Production at Hadron Accelerators*, Snowmass, June 21 - July 2, 1993, ed. P. McBride and C. S. Mishra. The number is based on the calculations presented in P. Nason, S. Dawson, and R. K. Ellis, Nucl. Phys. B **303**, 607 (1988) and P. Nason, S. Dawson, and R. K. Ellis, Nucl. Phys. B **327**, 19 (1989).

[17] F. Abe *et al.* Phys. Rev. D **50**, 5550 (1994);
N. M. Amos *et al.* Phys. Rev. Lett. **68**, 2433 (1992).

[18] D. Buskulic *et al.* Zeit. Phys. C **75**, 397 (1997).

[19] D. Buskulic *et al.* Phys. Lett. B **356**, 409 (1995).

[20] P. Abreu *et al.* Zeit. Phys. C **72**, 17 (1996).

[21] R. Akers *et al.* Phys. Lett. B **327**, 411 (1994).

[22] K. Abe *et al.* Phys. Rev. Lett. **74**, 2890 (1995).

[23] The LEP B Oscillations Working Group (V. Andreev *et al.*) have summarized the current status of Δm_d and Δm_s as of August 18, 1997. They arrive at the following values: $\Delta m_d = 0.472 \pm 0.018\ \hbar\mathrm{ps}^{-1}$ and $\Delta m_s > 10.2\ \hbar\mathrm{ps}^{-1}$ at 95 % CL. See `http://www.cern.ch/LEPBOSC/` or CDF internal note 4297.

[24] BaBar Technical Design Report. SLAC-R-457, March 1995.

[25] Belle Technical Design Report. KEK-Report-95-1, April 1995.

[26] Hera-B Technical Design Report. DESY-PRC 95/01, January 1995.

[27] F. Abe *et al.* The CDFII Detector Technial Design Report. Fermilab-Pub-96/390-E, November 1996.

[28] F. Abe *et al.*, Nucl. Instrum. Methods Phys. Res. A **271**, 387 (1998).

[29] P. Renton, *Electroweak Interactions*, Cambridge University, New York (1990).

[30] J. D. Richman and P. R. Burchat, Rev. Mod. Phys. , Vol 67, No 4, Oct 1995.

[31] M. Neubert. Submitted to Journal of Mod. Phys. A, April 1996, `hep-ph/9604412`.

[32] L. Wolfenstein, Phys. Rev. Lett., **51**, 1945 (1983).

[33] M. Gronau, Phys. Rev. Lett., **63**, 1451 (1989).

[34] A. J. Buras *et al.*, Nucl. Phys. B**245**, 369 (1984).

[35] A. Buras. and R. Fleischer. hep-ph/9704376. April (1997). To appear in *Heavy Flavours II*, World Scientific (1997), Eds. A. J. Buras and M. Lindner.

[36] J. P. Alexander *et al.* Phys. Rev. Lett. **77**, 5000 (1996).

[37] T. Inami and C. S. Lim, Prog. Theor. Phys. **65**, 297 (1981).

[38] A. J. Buras, Proceedings of 'Beauty 95', Oxford, England, July 1995, Nucl. Instrum. Meth. A **368**, 1 (1995).

[39] A. J. Buras, Nucl. Phys. B **347**, 491 (1990).

[40] J. M. Flynn, Plenary talk at ICHEP96, July 1996, `hep-lat/9611016`.

[41] A. J. Buras, Plenary talk at ICHEP96, July 1996, `hep-ph/9610461`.

[42] F. Abe. *et al.* Phys. Rev. Lett. **75**, 11 (1995).

[43] H. U. Bengtsson and T. Sjöstrand, Computer Physics Commun. **43**, 43 (1987); T. Sjöstrand, Computer Physics Commun. **82**, 74 (1994).

[44] P. Avery, K. Read, and G. Trahern, Cornell Internal Note CSN-22, 1985 (unpublished).

[45] F. Abe *et al.* Phys. Rev. D, Vol. 50, No 5, Sept. 1994.

[46] F. Abe *et al. Observation of* $\pi - B$ *meson Charge-flavor Correlations and Measurement of Time Dependent* $B^0\bar{B}^0$ *Mixing in* $p\bar{p}$ *Collisions.* Submitted to Phys. Rev. D.

[47] P. Sphicas. *Combining Flavor-Taggers.* CDF Internal note 3425.

[48] D. Kestenbaum, Thesis, Harvard University (1996).

[49] D. Buskulic *et al.* Phys. Let. B **377**, 205 (1996).

[50] W. Adam *et al.* CERN-PPE/97-114, Aug. 1997, to be submitted to Phys. Lett. B.

[51] F. Bedeschi *et al. Formulas to Describe Resolution Effects in Mixing Analysis.* CDF Internal Note 2859.

[52] F. James, CERN Program library long writeup D506.